Development of high-power 3 µm fiber laser sources and components

Thèse

Yiğit Ozan Aydın

Doctorat en physique
Philosophiæ doctor (Ph. D.)

Québec, Canada

Development of high-power 3 µm fiber laser sources and components

Thèse

Yiğit Ozan Aydın

Sous la direction de:

Martin Bernier, directeur de recherche
Réal Vallée, codirecteur de recherche

Résumé

Les systèmes laser en fibre optique de verre fluoré se sont placés en tête de file pour la génération de lumière cohérente dans l'infrarouge moyen, de 2 à 5 μm. En particulier, les lasers à fibre opérant à 3 μm ont attiré une attention considérable puisqu'ils permettent le développement d'applications en spectroscopie, en contre-mesure militaire et en médecine. De ce fait, ces lasers ont connu des progrès considérables en termes de puissance, de qualité de faisceau, de fiabilité et de compacité dans la dernière décennie.

Cette thèse s'inscrit dans cette démarche d'accroissement des performances des lasers à fibre infrarouges opérant à 3 μm. Ainsi, elle présente différents systèmes laser en fibre de verre fluoré et détaille les composants tout-fibre qui ont permis d'atteindre des records d'efficacité énergétique, de puissance et d'énergie par impulsion.

Trois types de sources laser, chacune ayant établi un record de performance, ont été investiguées. Tout d'abord, une efficacité laser record de 50% a été obtenue à partir d'un laser à fibre opérant à 2.8 μm en utilisant le principe de cascade laser à 2.8 et 1.6 μm. Ensuite, un amplificateur à fibre, basé sur des fibres dopées à l'ion erbium et aux ions holmium et praséodyme, a permis d'amplifier des impulsions picosecondes à 3 μm d'une source laser à l'état solide pour obtenir une énergie par impulsion (122 μJ) et une puissance moyenne (2.45 W) records. Finalement, une cavité laser tout-fibre dopée à l'ion erbium opérant autour de 3 μm, dépourvue d'épissures fusionnées, a mené à la démonstration d'une puissance laser record de 41.6 W. D'autre part, cette thèse a ciblé différents obstacles limitant l'accroissement de la puissance des lasers à fibre opérant à 3 μm, et a permis d'identifier des pistes de solutions pour pallier ces limitations. En l'occurrence, la photodégradation de l'extrémité de sortie des lasers à fibre à 3 μm, causée par la diffusion de la vapeur d'eau ambiante, limite la durée de vie et la puissance maximale de ce type de laser. Ainsi, le dernier volet de cette thèse a été consacré à l'étude expérimentale de la photodégradation d'embouts de protection à base de verre fluoré ou d'oxyde. Cette étude a mené au développement d'une nouvelle méthode permettant d'inhiber la diffusion de la vapeur d'eau dans les embouts de protection. Cette thèse représente une avancée majeure dans le contexte de l'accroissement de la puissance des sources laser en fibre optique opérant à 3 μm et démontre leur potentiel indéniable pour remplacer d'autres types de lasers dans une multitude d'applications.

Abstract

Fluoride fiber laser technology is one of the noteworthy tools for generating coherent mid-infrared signal between 2 to 5 μm that has made outstanding progress over the last decade in terms of compactness, reliability, high beam quality, and output power. In the mid-infrared spectral region, laser emission near 3 μm is crucial for many applications such as spectroscopy, countermeasures and medicine. In addition, there has always been an increasing demand for higher laser output parameters to open new doors for potential applications.

This dissertation presents a series of experimental studies of fluoride fiber laser systems, either in continuous wave or pulsed regime, and of their critical in-fiber components to achieve a laser emission with high slope efficiency, output power, and pulse energy near 3 μm.

During this PhD project, three main 3 μm-class fluoride fiber laser sources, each representing at least one record output parameter in their own category, have been investigated. First, the highest optical-to-optical efficiency (50%) at 2.8 μm was achieved from a diode-pumped fiber laser cavity by cascaded transitions of 2.8 μm and 1.6 μm in a low-doped erbium fluoride fiber. Then, active media based on erbium and holmium/praseodymium zirconium fluoride fibers seeded by a sub-ns solid-state laser enabled to achieve highest pulse energy (122 μJ) and average power (2.45 W) from a picosecond fiber laser amplifier operating near 3 μm. Lastly, the highest average power 3 μm-class laser (41.6 W) has been demonstrated by using a splice-less heavily erbium-doped fluoride fiber medium. The major problems during the high-power laser operation have been investigated and potential solutions were proposed. The most common problem of all the high-power 3 μm fiber laser demonstrations is the degradation of the fiber tips due to OH migration, which limits the output power and can lead to catastrophic failures. Therefore, in the last part of the PhD project, the performance of fluoride- and oxide-based endcap components under high-power 3 μm laser emission has been experimentally investigated and a novel endcapping method was proposed for suppressing the OH migration. Experimental studies in this PhD project represents a significant advance for further power scaling of 3 μm fluoride fiber laser sources and shows their potential to replace other laser technologies.

Contents

List of Tables

List of Figures

List of Abbreviations

CPS cladding pump stripper

CR cross relaxation

CW continuous wave

DFBL distributed feedback lasers

DFG difference-frequency generation systems

DM dichroic mirror

ESA excited state absorption

ET energy transfer

ETU energy transfer upconversion

FBG fiber Bragg gratings

GSA ground state absorption

HR-DM highly reflective dichroic mirror

HR-FBG high reflective fiber Bragg grating

ICLs inter-band cascade diode lasers

InGaAs indium gallium arsenide

IR infrared

LID laser induced damage

LR-FBG low reflective fiber Bragg grating

mid-IR mid-infrared

MOPA master oscillator power amplifier

MPC multi pump combiner

MPR multiphonon relaxation

NA numerical aperture

OPG optical parametric generation

OPO optical parametric oscillators

PbP point-by-point

PM polarization maintaining

QCL quantum cascade lasers

RMS root-mean square

SC supercontinuum

UV ultraviolet

VBG volume Bragg grating

YAG yttrium aluminum garnet

anneme, babama ve kardeşime...

Acknowledgements

This dissertation would not have been possible without many people who contributed to it in their own particular way and for that I want to thank them. First and foremost, I would like to thank my supervisor Martin Bernier for believing in me, for giving me a wonderful opportunity to be his PhD student and for being an excellent advisor. His magical word "*easy!*" has always been a moral support and has made every part of this journey easier. His outstanding guidance, advice, and support during this work encouraged me and allowed me to achieve significant scientific results. I am eternally indebted in my co-supervisor Réal Vallée who enlightened and motivated me with his immense knowledge, enthusiasm, and wise advice. He provided a dynamic and excellent research environment with the most modern equipment and generous research support. Finally, I would like to thank my both supervisors for the financial support I received through their projects and for allowing me to participate in international conferences, trainings, and high-level meetings.

Vincent Fortin deserves a very special word of gratitude. I always feel lucky to have had a chance to work with him and learn from him. He has always taken the time to discuss and enrich my work, helped me with all my experimental work, and I would not be where I am today without him.

I would like to thank Frédéric Maes, a great friend and office mate, who generously gave his time to offer me valuable comments toward improving my dissertation and made excellent scientific contributions to my research work.

Many members of Bernier and Vallée research groups contributed to my research project and helped me along the way. I would like to thank especially Pascal Paradis and Frédéric Jobin for insightful discussions and their help concerning the numerical simulations and my common computer related problems. Thanks to Simon Duval, Jean-Christophe Gauthier, Louis-Rafaël Robichaud, Souleymane T. Bah and Louis-Philippe Pleau for their friendship and support in the laboratory. I feel always lucky to have them as friends.

I would like to thank Stuart D. Jackson and Darren Kreamer for their excellent scientific contributions to my research work.

I would also like to acknowledge the contributions of the technicians to the success of this

project, especially Marc d'Auteuil and Stéphan Gagnon who were always available and answered with a great patience to all my technical needs.

I am grateful to all of the Centre d'optique photonique et laser (COPL) members I had the pleasure to work with during my PhD project, especially, Diane Déziel who has always supported and helped me for completing my out-of-lab tasks with her invaluable service.

I am deeply grateful to Michel Piché for agreeing to read my thesis before the initial deposit. I thank my committee members Younes Messaddeq, F.Ömer İlday and Michel Piché for their guidance and for accepting to serve on my committee.

The list of people who contributed to my happiness outside the professional context is quite exhaustive, but I would like to thank especially Tolga Tezcan, Andréanne Béland, Sasan Zhalehpour, Alexandre Arsenault-Bourdeauand, Çağatay Göde, Koray Eken, Emre Yağcı and Caner Boyraz for their love, care and moral support. I feel so lucky and am so thankful to have such wonderful people in my life.

A very special thanks to my family for their endless love and support. The words cannot express how grateful I am to my mother, father and brother who encouraged me all the time and this work would not have been possible without them. In addition, thanks to my aunt and uncle who have always supported me with their love.

Prof. Vallée asked me if I was sure I wanted to live at -40 ℃ as a first question of my PhD interview before I moved to Canada. At that time it was impossible to imagine the benefits of winter but it now deserves an appreciation. A final thank to Québec's winter for motivating me to complete my PhD as soon as possible.

Foreword

This thesis deals with the development of high-power 3 μm fluoride-based fiber laser sources and of their in-fiber components. High power fiber laser development near 3 μm is a considerably challenging process due to the weak mechanical and thermal properties of fluoride fibers and the limitations related to the development of laser components based on fluoride glass. In this thesis, three fluoride fiber laser systems based on different active media have been designed and experimentally demonstrated. The limiting factors for achieving high-power laser operation in fluoride fibers have been studied which resulted in a record laser slope efficiency, a record laser output power, and a record laser pulse energy near 3 μm from each system, respectively. Moreover, the degradation of fiber tip due to OH migration that is the major limiting factor for 3 μm laser power scaling was experimentally studied by investigating the performance of different endcap components under high-power laser emission. A novel method has been proposed to overcome this problem which consists of sputtering a barrier film on the endcap face. This work has been carried out under the supervision of Martin Bernier (director) and Réal Vallée (co-director) in the Centre for Optics, Photonics and Lasers at Laval University.

Organization of Thesis

This thesis is organized with an introduction, 4 chapters and a conclusion. The introduction part consists of the idea behind the thesis and an overview of the applications that can benefit from 3 μm laser emission. Then, the importance of main fluoride fiber laser components followed with points to take into consideration during their fabrication is given. It also presents a theoretical overview of 3 μm transition from rare-earth doped fluoride fibers with a literature review and a content outlining the current status of these lasers. The major challenges while developing high-power fluoride fiber lasers are highlighted along with their proposed solutions in the last part of the introduction. The concepts exposed in this part are essential for a good understanding of the following chapters. Each of the chapters from 1 to 4 corresponds to an article which was published as part of the PhD project and one supplementary material belongs to the article presented in chapter 1. In the last part, the conclusion of the thesis and discussion of possible short- and long-term research projects are given.

Personal contribution to the presented articles

The layout of the figures was modified to adapt articles to the single column template of the thesis and the contents of the articles were divided into sections. All references in the articles are incorporated into the bibliography at the end of the thesis. The citation numbers in square brackets corresponding to each of the references may therefore differ from the original article. Apart from these modifications, no changes have been made to the published articles.

Chapter 1 presents an article "Diode-pumped mid-infrared fiber laser with 50% slope efficiency," published in **Optica**, Vol. 4, pp 235-238 (Y.O. Aydin, V.Fortin, F. Maes, F. Jobin, S.D. Jackson, R. Vallée, and M. Bernier). The laser demonstrated in this work has an output power of 12.95 W at 2.8 μm with a slope efficiency of 49.5%. This slope efficiency is the highest optical-to-optical conversion efficiency achieved from a diode-pumped mid-infrared fluoride fiber laser thanks to a new excited state absorption discovered in erbium-doped zirconium fluoride fiber. My contribution to this work can be divided into four points: Assembling the laser cavity, conducting all the experimental measurements, writing the manuscript and supplementary material as a first author, compiling all the figures presented in the article and supplementary material. Fiber Bragg gratings (FBG) in this work were fabricated by Martin Bernier. I also presented the result of this study at CLEO Europe (The European Conference on Lasers and Electro-Optics) in Munich, Germany in 2017.

The article in Chapter 2, "High-energy picosecond pulses from a 2850 nm fiber amplifier" is a demonstration of a three-stage fluoride fiber amplifier seeded by an optical parametric oscillator and it was published in **Optics Letters**, Vol. 43, pp. 2748-2741 (Y.O. Aydin, V. Fortin, D. Kraemer, A. Fraser, R. Vallée, and M. Bernier). In this work, the obtained pulse energy (122 μJ) was the highest ever produced from a fluoride fiber amplifier and the average power (2.45 W) is a record for a sub-ns 3 μm class fiber laser source. My contribution to this work is similar to the article presented in Chapter 1. Another version of the amplifier delivering 100 μJ pulses by using different seed source and one amplification medium was demonstrated and presented at the 8th EPS-QEOD Europhoton Conference in Barcelona, Spain in 2018.

"Towards power scaling of 2.8 μm fiber lasers" is a high-power continuous-wave demonstration of a 3 μm-class fiber laser presented in Chapter 3. It was published in **Optics Letters**, Vol. 43, pp. 4542–4545 (Y.O. Aydin, V. Fortin, R. Vallée, and M. Bernier). In this work, a record output power (41.6 W) from a fiber laser operating near 3 μm was reported and the long-term performance of two commonly used endcap components was investigated. The laser cavity in this work is the first splice-less demonstration of high-power 3 μm-class fluoride fiber laser and represents a significant advance for further power scaling of such lasers. My contribution to this work is similar to the article presented in Chapter 1. FBGs in this work were fabricated by Martin Bernier. I presented the preliminary results of this work at 20th Photonics North Conference in Montreal, Canada in 2018. Then, I presented the results at

CLEO US (Conference on Lasers and Electro-Optics) in San Jose, the United States in 2018.

In Chapter 4, another article entitled "Endcapping of high-power 3 μm fiber lasers" is presented. This article was published in **Optics Express**, Vol. 27, pp. 20659–20669 (Y.O. Aydin, F. Maes, V. Fortin, S.T. Bah, R. Vallée and M. Bernier). The article given in Chapter 3 highlights the photo-degradation of fiber tips as the main limitation of power scaling and long-term performance of high-power 3 μm-class fiber lasers. Therefore, to investigate solutions for this problem, the research work presented in Chapter 4 focuses on OH-diffusion related degradation of various endcaps by comparing their performances under high-power laser radiation at 3 μm. In this study, sputtering a nanoscopic diffusion barrier film on the output face of the endcap component was proposed as a new method to completely suppress OH diffusion from output fiber face. It is believed that thanks to this novel method, the long-term operation of 100-W-level 3 μm fiber lasers will be feasible. My contribution to this work can be divided into five points : Assembling a stable 25 W laser cavity used in the long-term tests, conducting all the experimental measurements of laser cavity, fabricating all the fluoride- and fluorogermanate-based endcaps, conducting long-term endcap performance experiments except one with nanoscopic thin-film of silicon nitride and writing the manuscript as a shared first authorship together with Frédéric Maes.

Introduction

This part consists of 7 sections. The first section (I.1) is providing the context and relevance of the work by briefly introducing the main idea behind this thesis and the importance of the research work. Section I.2 gives an overview of the applications that can benefit from 3 μm laser sources. In section I.3, the importance of the main components of the fluoride fiber laser is discussed and points to take into consideration during their fabrication are described. The theoretical overview of 3 μm transitions from rare-earth doped fluoride fibers is given in section I.4. A literature review with the current state of high-power 3 μm fiber lasers and current challenges are described in sections I.5 and I.6, respectively. In the last section (I.7), presentation of the articles published in the context of the PhD project is given.

I.1 Context and relevance

It has been more than century since Albert Einstein proposed the stimulated emission theory which is the fundamental idea behind laser science. After the invention of the first laser [1], which was based on laser emission from a ruby crystal, laser technology has made tremendous progress and nowadays lasers are found almost everywhere in daily life. As lasers evolve and become an integral part of modern society, so do the many other applications in the area of manufacturing, construction, telecommunication, automotive, medicine, security, etc. There are various types of lasers which are divided into different types according to their active media. Fiber lasers, in which the laser beam propagates through the glass-based core of an optical fiber, have become one of the most popular laser technologies thanks to their potential for power and brightness scalability, excellent beam quality, high efficiency, and reliability. After the first experimental demonstration of laser operation in a fiber [2], it has taken more than 20 years to develop a technique for fabricating low-loss rare earth doped single and multimode optical fibers [3] which is one of the most important milestones in fiber laser technology. In the first place, fiber lasers started to be used in telecommunication area, then the invention of double clad silica fibers enabled the achievement of high output powers, and their eventual use in other areas. As laser technology revolutionized many sectors, research has continuously grown to improve laser components as well as output beam parameters such as average power, peak power, pulse energy, and beam profile. There is always an increasing demand for achieving

higher output parameters, therefore it is the main concern of laser science and technology considering that enhanced output parameters always have the potential to open new doors for potential applications. Today, such need brought the output power level of silicate-based fiber laser systems up to 100 kW [4] and pulse energies up to 100 mJ [5], while maximum output power obtained from a fiber laser was only 100 W in 1999 [6].

The spectral properties of the laser beam is another crucial parameter, since the emission wavelength generally determines the application. Simultaneously, as fiber technology evolved and output power levels increased, the need for different wavelengths has grown as well. The active ion determines the emission wavelength of the laser, as well as the type of host material which determines the spectral range of the laser. The mid-IR region of the electromagnetic spectrum (2-20 μm) has great importance for many applications in medicine, defense, industry, environment and research. In fiber laser technology, the well known silicate-based fibers are transparent up to 2.3 μm (1 dB/m) and can therefore not provide mid-IR wavelength coverage so different fiber hosts must be employed to achieve longer optical transparency. While researchers focus on silicate glasses for laser development, in 1975, heavy metal fluoride glass was accidentally discovered, which provides a broader spectral transmission window with much lower minimum transmission losses. This discovery has made the efficient generation of mid-IR laser emission through fibers possible with the fabrication of high-quality fluoride-based fibers. More than 10 years after the discovery of the fluoride glass, the first laser emission at 1.05 μm from a multimode fluorozirconate fiber was demonstrated [7]. Subsequently, the first mid-IR laser emission at 2.702 μm was reported from an Er^{3+}-doped fluoride fiber [8]. Hereafter, extraordinary progress in fluoride fiber laser development, especially in the last two decades, has proven their potential to replace existing mid-IR sources such as YAG-based lasers, quantum cascade lasers (QCLs) and optical parametric oscillators (OPOs).

In the mid-IR region, laser emission near 3 μm is crucial for many applications such as spectroscopy, countermeasures, and medicine. Especially medicine is the main target area of such lasers since soft and hard biological tissues contain a high amount of water and such a wavelength coincides with the water absorption peak. Thus, there is a rapidly increasing demand for compact, highly efficient and bright, high-power 3 μm laser sources and fluoride fiber lasers are ideal candidates to meet those needs thanks to their favourable properties. There is not a standard definition of "high-power" term in laser science and as a rule, the era and the type of technology used determine the proper use of such term. While, half a W of laser emission near 3 μm from a fiber laser could be accepted as "high-power" 20 years ago [52], today such power levels are defined as low power. On the other hand, for different spectral range, i.e. 1 μm silicate-based lasers, the "high-power" term is considered for kW power levels, whereas this is tens of watts for 3 μm fiber laser sources today. In short, it is possible to define high-power fluoride fiber lasers as the laser sources in pulsed or continuous wave (CW) operation modes generating considerably higher output power than other fluoride fiber lasers at the same wave-

length. During the last 20 years, 3 μm fluoride fiber lasers and their components have made significant progress and still maintain a high potential for further improvement. While the CW and pulsed output powers of the first version of such lasers were μW-level and their peak power was watt-level, respectively [9; 53], today more than 40 W of CW power and 100 kW of peak power is possible thanks to advances in this research field. The evolution of the reported CW output power of 3 μm fluoride-based fiber lasers as a function of time is shown in Fig. I.1, where the output power shows an exponential increase as a results of the growing interest in aiming to achieve higher output levels.

In this PhD project, fluoride fiber laser systems operating near 3 μm based on different active media and approaches and their critical in-fiber components to achieve high output power, efficiency and peak power were investigated. Although Fig. I.1 presents an exponential increase in output power, demonstration of higher output power at 3 μm becomes more challenging due to limits related to the development of the components as well as the physical and chemical properties of fluoride glasses. One of the major challenges is the fluoride fiber tip degradation due to OH diffusion, a phenomenon limiting the maximum output power, was also studied by the fabrication of the novel endcapping components within the scope of this study.

The introduction part of this thesis briefly describes the main components of fluoride fiber

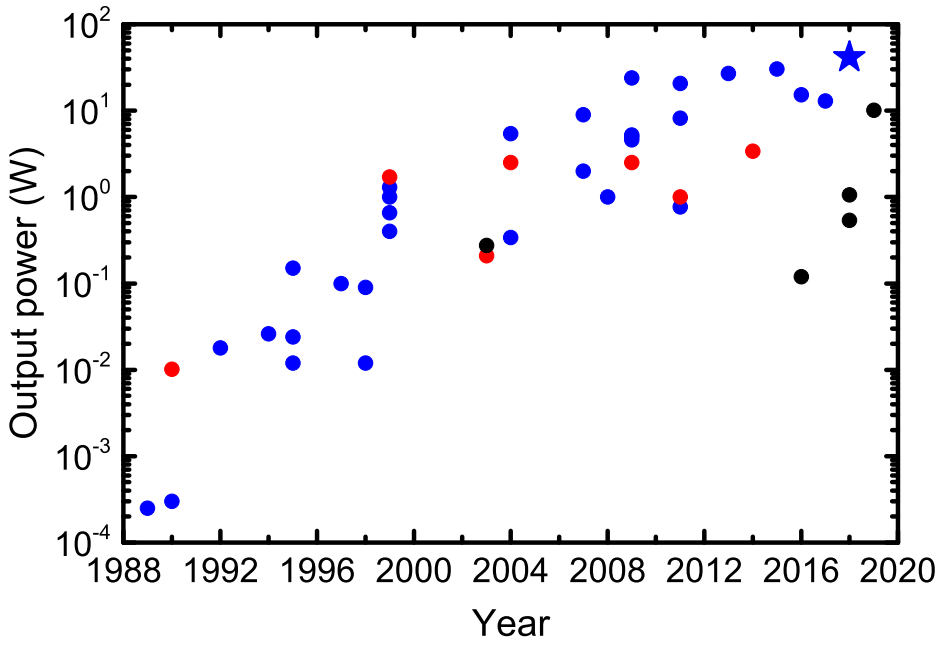

Figure I.1: Output power from fluoride fiber lasers based on Er^{3+} (blue), Ho^{3+} (red) and Dy^{3+} (black) gain media operating near 3 μm in CW mode as a function of time. Star, published through this thesis. Data points were taken from [9; 10; 11; 12; 13; 14; 15; 16; 17; 18; 19; 20; 21; 22; 23; 24; 25; 26; 27; 28; 29; 30; 31; 32; 33; 34; 35; 36; 37; 38; 39; 40; 41; 42; 43; 44; 45; 46; 47; 48; 49; 50; 51].

.

lasers, the schemes for generating 3 μm emission from rare-earth doped fluoride-based fibers, the major high-power based problems and promising methods to solve such problems. The work presented in the first chapter resulted in the demonstration of the highest efficiency diode pumped single-mode fluoride fiber laser operating near 3 μm. The second chapter presents a pulsed 3 μm laser amplifier which achieved the highest pulse energy and average power obtained from a sub-ns fluoride fiber amplifier. In Chapter 3, another simple diode pumped single-mode laser cavity is demonstrated which emits the highest CW output power around 3 μm ever achieved from a fiber laser. In Chapter 4, performances of the different endcapping components are discussed and a novel method to suppress OH diffusion in fiber tip is proposed.

I.2 Applications of 3 μm laser sources

The spectral region around 3 μm offers many advantages for different applications types in many areas. This section summarizes the most promising applications for 3 μm laser sources and, more specifically, for 3 μm fiber based sources.

Medicine

Laser sources based on different technologies and spectral ranges are already widely used in various medical applications as a replacement of traditional surgical tools. Moreover, laser radiation around 3 μm has great potential for such applications. Water is the dominant constituent in the human body and the fundamental stretching vibration of OH bond is located near 2.94 μm. Therefore, radiation is effectively absorbed by bio-materials and enables small penetration depths and precise bio-processing with minimal thermal damage and coagulation zones. The absorption spectrum of water is shown in Fig. I.2, in which at 2.94 μm peak, the absorption coefficient is 13300 cm^{-1}.

CO_2 lasers still popular for medical applications especially in cosmetic tissue surgery due to high water absorption around their operating wavelength of 10.6 μm. Then, bulk Er:YAG systems operating at 2.94 μm have started to replace CO_2 lasers given water absorbs ten times more at 2.94 μm than at 10 μm. Additionally, their shorter pulse duration leads to less thermocoagulative damage. Today, Er:YAG lasers at 2.94 μm are used in different medical applications such as lithotripsy [54], dentistry [55], ophthalmology [56], biopsy [57], osteotomy [58], otolaryngology [59], dermatology [60], angioplasty [61]. In general, high-power CW and pulsed 3 μm lasers are used for hard tissue applications such as bone or dental processing; low power ones are prefered for soft tissue applications such as skin processing. Despite the fact that there are several parameters which affect the laser-tissue interaction, the types of mechanisms are classified as photochemical, thermal, photoablation, plasma-induced ablation or photodisruption [62]. Depending on the laser power, energy density and interaction time, the effect on the tissue varies. For instance, tissue heating occurs at low power densities (100 W/cm^2), tissue evaporation (100-10^8 W/cm^2), plasma and rear shock waves (10^9-10^{15}

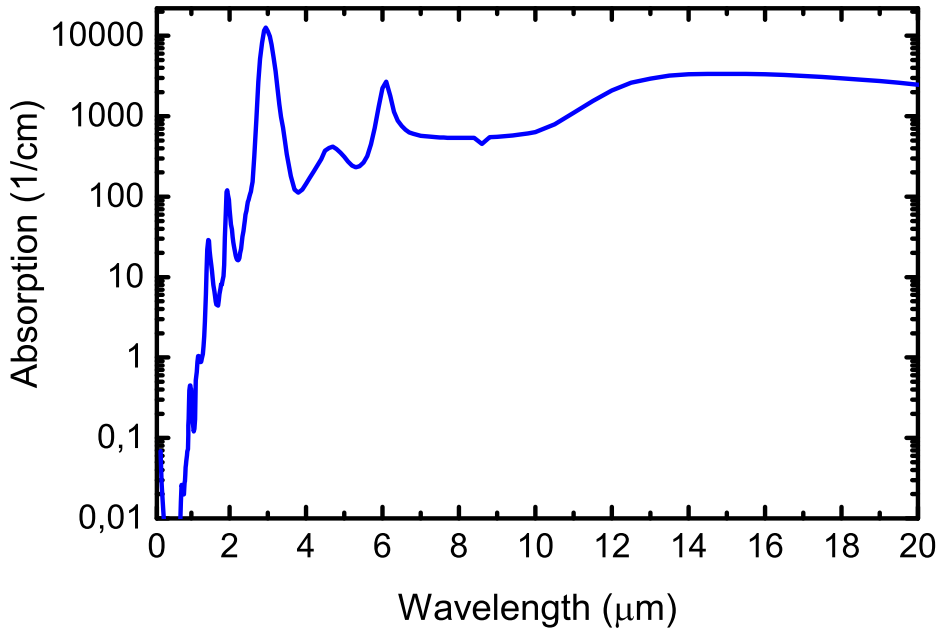

Figure I.2: Absorption spectrum of liquid water. Figure extracted from [67].

W/cm^2) appear at higher power densities [63]. On the other hand, laser exposure time is crucial to control all the applications by affecting the process quality. While plasma-induced ablation, photo-disruption and ablation occur for pulses shorter than 1 ns, photo-chemical and thermal interactions take place in CW or microsecond regimes [62]. Hence, the pulse duration has an effect on the resulting process. Er:YAG systems enable pulse durations lasting dozens of nanoseconds which is longer than the thermal relaxation time of water in biological materials. There are many medical applications requiring shorter pulses around 3 μm such as optical or corneal transplant surgery and stapes surgery. Such applications were realized by using optical parametric generation (OPG) based on solid-state laser architectures [64; 65]. Recently, cold vaporization of tissues by using picosecond pulses at 2.94 μm was also demonstrated and it shows that 3 μm ultrafast lasers have a great potential for damage-free medical applications [66].

The requirements of different laser parameters for medical applications shows that fiber lasers operating at 3 μm also have a great potential as clinical tools thanks to their advantages such as high beam quality, high efficiency, small foot-print and rugged design. The interaction of the laser output from a fiber laser with biomedical materials has been already studied and the clinical use of such systems has been tested by different research groups. A CW Er^{3+},Pr^{3+} fiber laser operating at 2.71 μm was used to ablate chicken and liver tissues. It was shown that laser processing is possible without carbonisation or charring [68]. Cutting capability of 3 and 2 μm cascade fiber lasers was demonstrated on soft rabbit tissues and enabled a precise cutting [23; 69]. On the other hand, rare-earth doped fluoride fiber lasers could be used with proper mirrors to achieve laser emission at a specific wavelength around 3 μm, which provides

precise control of the penetration depth of processing. For example, in Er^{3+}-based media with proper mirrors the laser wavelength could be selected from 2.7 μm to 3 μm and this range could even be extended up to 3.3 μm by using Dy^{3+} dopants. On the other hand, especially for high-power short pulse 3 μm medical lasers, fiber technology plays an important role by serving as an amplifier to improve power levels. In Chapter 2, a high-energy picosecond fiber laser amplifier operating at 2.85 μm which has the potential to be used in medical applications, thanks to its sub-ns pulse duration and high pulse energy, is demonstrated.

Spectroscopy

Most of the atmospheric gases showcasing high absorption caused by fundamental vibration bands are located in the mid-IR spectral region, especially from 3 to 5 μm. Hence, laser sources operating in the mid-infrared range are required for spectroscopy, trace gas detection and monitoring applications with high temporal and spectral resolutions. Fig. I.3 shows the absorption lines of important gases located between 2.5 and 5 μm. In this region, the absorption line strength of many gases is much stronger than their short-wave counterparts. The detection of the molecular species is realized by using tunable lasers such as difference-frequency generation systems (DFG), optical parametric oscillators (OPOs), quantum cascade lasers (QCLs), inter-band cascade diode lasers (ICLs) or distributed feedback lasers (DFB).

The detection of species around 3 μm can also be realized by using tunable ZrF_4 fiber-based systems. A tunable dysprosium-doped ZBLAN fiber laser from 2.95 to 3.35 μm was demonstrated by Majewski et al. and the tuning range covers the molecular absorption of OH, NH and CH-based molecules located around 3 μm [70]. In this system, another 3 μm-class Er^{3+}:ZrF_4 fiber laser was used as a pump source. In addition to this, an electronically controlled swept-wavelength laser using a dysprosium ZBLAN fiber and an accousto optic filter was used for real-time remote sensing of ammonia gas by Woodward et al. [71]. In this work, an Er^{3+}:ZrF_4 fiber laser at 2.83 μm was used as a pump source and a sweep range of 360 nm (2.89 to 3.25 μm) was achieved.

Supercontinuum fluoride fiber laser sources are ideal candidates for broadband spectroscopy applications due to their longer wavelength extent range against silicate-based versions that have limited transparency. Generally, in order to broaden the spectrum, ZrF_4 fibers are pumped by 2 μm or 1.55 μm pulsed sources [72; 73]. Then, advances in pulsed 3 μm OPG systems enabled the generation of supercontinuums with larger conversion efficiencies given their larger quantum efficiency. A supercontinuum extending up to 4.1 μm with 82% of its energy above 3 μm was demonstrated by seeding an Er^{3+}:ZrF_4 fiber with ps-level pulses at 3 μm from an OPG [74]. It was also shown that the spectral coverage could be extended up to 5.2 μm by using indium fluoride (InF_3) fibers [75]. Today, 3 μm fluoride fiber lasers provide high peak powers with short pulse duration and have the potential to replace OPG sources as a seed sources and have an indirect advantage by enabling efficient and small footprint systems. Recently,

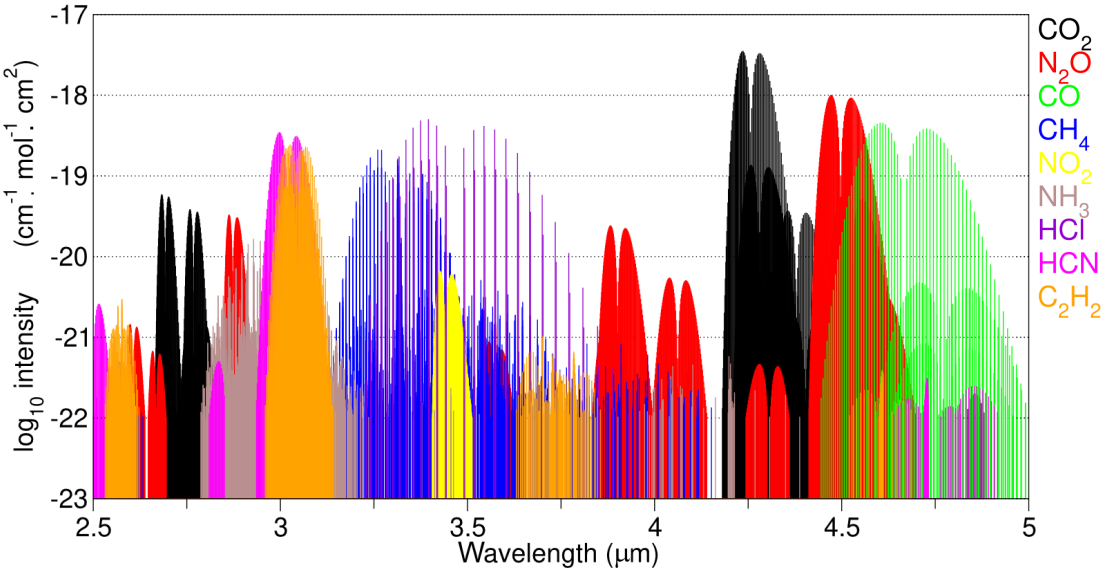

Figure I.3: Absorption spectra of important trace gases in the spectral region between 2.5 and 5 μm. The molecular line data is compiled by spectralcal.com online modeling using HITRAN database [67].

it was shown that, 3 μm ZrF_4-based fiber laser systems have the ability to be mode-locked at fs or ps pulse duration with tens of kW peak powers [76; 77]. Moreover, seed signal at 2 or 3 μm provided by solid-state based or mode-locked lasers are coupled into the fiber by free-space coupling which causes losses and parasitic processes. Hence, the advance of 3 μm ultrafast fiber laser systems will have the potential to provide reliable monolithic fiber-based supercontinuum sources in the near future.

Defence & security

The spectral region between 3 and 5 μm has great importance for the monitoring and tracking of aerospace vehicles since the atmospheric transmission is maximum and detectors used in such vehicles are sensitive in this region. On the other hand, in the operation, hot parts of the aerospace vehicles such as the rotor, fuselage and nozzle reach temperature between 600-700 °C, which is the thermal signature of black body emission located between 3 and 5 μm [78]. Thus, efficient laser sources operating between 3 and 5 μm are necessary to achieve countermeasure systems against heat-seeking missiles. The laser could have a broad spectral width which covers the atmospheric transmission window or short width which tunes rapidly across the wavebands and should have a beam close to the diffraction-limit [79]. The effective modulation rate of the laser source is also important, especially for jamming new generation missiles [80]. For 3-5 μm countermeasure systems, ZrF_4-based fiber lasers are potential candidates given their high efficiency, beam quality, brightness, and small foot-print.

I.3 Fluoride fiber laser components

The evolution of the fluoride fiber laser technology considerably depends on the advances of optical components working in the mid-IR spectral region. The components used in mid-IR fiber lasers have progressed in the last 10 years leading to stable, long-term operation of high-power fiber laser systems operating around 3 μm. Despite this, fluoride fiber-based laser technology still lacks stable, high-power components compared to silica-based technology and has been advancing rather slowly due to the poor thermo-mechanical properties of fluoride glasses.

The main components for a 3 μm fiber laser system can be listed as, the fluoride-based fiber, the fiber Bragg gratings (FBGs), the pump sources, the splices and the endcaps. Fluoride fibers have been used for more than 20 years in laser systems and their manufacturing has been progressing. Using appropriate fluoride fibers for laser systems is critical to obtain the required laser emission parameters. Therefore, geometrical and chemical properties of the fiber are determined prior to the manufacturing process by numerical simulations. FBGs simplify laser cavities by serving as a wavelength selective mirror in the fiber core and their fabrication in fluoride-based fibers is now possible [81]. Pump sources are the essential components for exciting the laser medium and choosing a proper pumping wavelength depending on the lasing mechanism is vital. The fused glass components, namely splices and end-caps also play an important role for laser cavities to ensure their reliability and efficiency by providing a higher damage threshold and increased resistance to OH degradation. State of-the-art heat sources are necessary for achieving a junction between two fibers and the development of endcapping components. The procedure with non-oxide-based fiber glasses is more difficult than with oxide-glasses because of low glass transition temperature and mechanical properties of non-oxide fiber materials. Hence, different novel approaches and state-of-the-art fiber splicing technologies are necessary to achieve low-loss fiber junctions and components between fluoride-based fibers, as well as fluoride to oxide-based fibers.

In this section, the role of the main fluoride fiber laser components and the development of in-fiber components used in 3 μm-class fiber lasers are explained.

I.3.1 Fluoride-based fibers

Fluoride-glass fibers are the core components of 3 μm fiber lasers and amplifiers, thanks to their excellent mid-IR transparency compared to silica fibers. They are the member of fluorozirconate glass family, which were reported for the first time by M. Poulain et al. in 1975 by observing ZrF_4-BaF_2-NaF ternary systems [82]. Then, ZBLAN, the most popular and stable member of this family composed of ZrF_4, BaF_2, LaF_3, AlF_3 and NaF was reported [83]. Given such glasses are mainly composed of ZrF_4, they are often called ZrF_4-glass fibers or ZrF_4-fibers.

The low phonon energy of such glasses (580 cm^{-1} for ZBLAN [84]) leads to metastable states when they are doped with rare earth ions. They are highly soluble which enables highly concentrated doping of rare-earth ions up to 10 mol.% [84]. Therefore, it is possible to obtain laser output by using short-length of highly-doped ZrF_4-based fibers. Moreover, as a result of their low phonon energy, the theoretical attenuation of such fibers around 3 μm is less than 1 dB/km. Currently, it is possible to find commercially available ZrF_4-based fibers with background propagation losses less than 60 dB/km at 2.9 μm [44], which is far from the theoretically predicted minimum loss of fluoride fibers ($<$ 0.01 dB/km) [85]. The attenuation behaviour of a single-mode ZrF_4 (*Le Verre Fluoré*) and a low-OH SiO_2 fibers (*Centre d'Optique, Photonique et Laser*) up to 4.5 μm is shown in Fig. I.4.

Although their excellent properties for mid-IR transmission and their low phonon energy, ZrF_4 fibers present several disadvantages compared to SiO_2 fibers. Before the fiber manufacturing process, choosing the right fiber according to required laser specifications is necessary. Determining geometrical and optical properties, such as core-clad ratio, clad shape, NA, chemical properties, rare-earth dopant and its concentration, is achieved by numerical simulations. During the manufacturing process, point defects due to impurities and imperfections such as bubbles, micro-crystals, core-clad boundary fluctuations could be formed due to the high level of transition metals and OH impurities. These defects cause scattering spots or absorptive losses and may restrict the output power, therefore resulting in catastrophic failures along the fiber. Thus, prior to the experimental work, it is required to screen fluoride fibers in or-

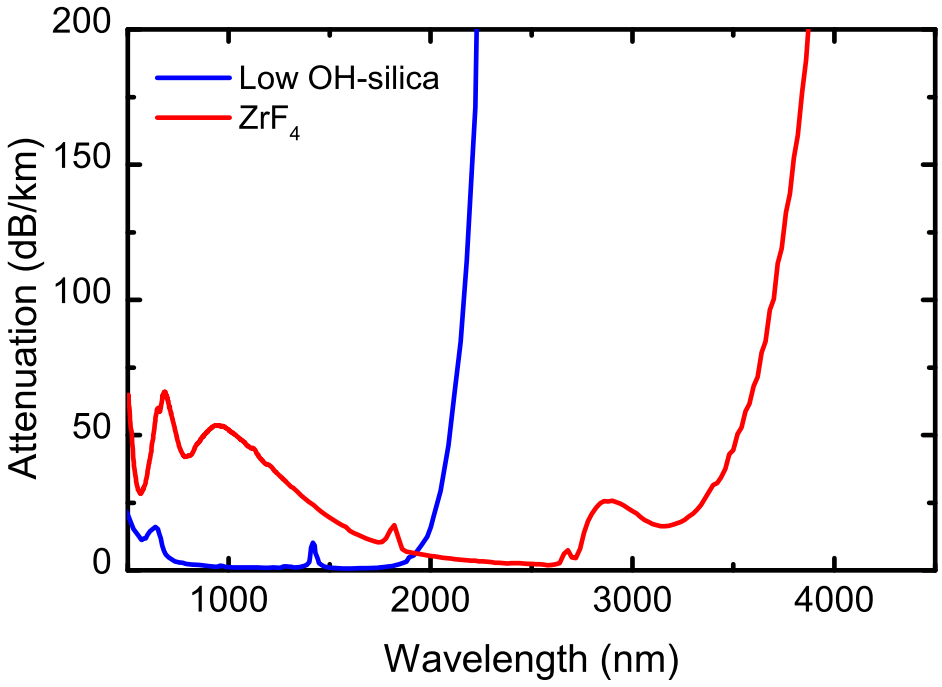

Figure I.4: Attenuation of ZrF_4 and low-OH silica fiber.

der to locate possible point defects on the fiber segment and reduce the occurrence of fiber failure during laser experiments. In order to verify geometrical properties, manufactured fiber segment from both end faces should be inspected by microscope. The smaller binding energy of ZrF_4-glass causes mechanical fragility (e.g. the strength of ZrF_4 fibers is less than 1 GPa [86], while it is 12 GPa for the silica fibers [87] and the theoretical mechanical strength of fluoride fibers is 40-50 % of silica fibers [88]) and poor resistance to environmental attacks. This is because of the nature of the fluoride-based glass in which Zr-F bonds are much weaker than Si-O bonds. For this reason, handling of such fibers is extremely challenging and requires special care during the splicing, FBG writing and laser assembling procedures. The low transition temperature (265 ℃ [89]) and low melting temperature (340 ℃ [90]) of such fibers is another potential problem for stable laser operation. Therefore, monitoring the fiber temperature during high-power laser operation is crucial to prevent against possible thermal catastrophic damages. The small difference between melting and transition temperature also requires precise heating during the splicing procedure of ZrF_4 fibers to avoid crystallization.

Fluoride glass optical fibers have been studied extensively after their discovery and their mechanical properties and repeatability of manufacturing have made tremendous progress especially in the last 10 years. It is possible to fabricate them in different geometries with a well-controlled core/clad eccentricity. Today, it is possible to find fluoride fibers with different geometries on the market. Their core diameter ranges from few-μm diameter to 900 μm. The NA ranges from 0.05 to 0.40 and the clad type can be designed single or double clad with hexagonal, square, cylindrical or double-D shape geometry. Their thermal expansion coefficient varies from 140 to $220\times10^{-7}K^{-1}$ [91] and refractive index can be modified from 1.43 to 1.60, which provides relatively low Fresnel losses compensates other mid-infrared glasses. Nowadays, polarization maintaining (PM) versions with ellipsoidal core and active versions with different dopant ions, such as Er^{3+}, Pr^{3+}, Ho^{3+}, Dy^{3+}, Ce^{3+}, Tm^{3+}, Nd^{3+}, etc. can also be manufactured [92; 93].

In addition to ZrF_4-based fluoride fibers, AlF_3- and InF_3-based fluoride fibers are commercially available and widely used in different areas. AlF_3 fibers contain higher molar concentrations of AlF_3 than ZrF_4 fibers and their transmission range is not as wide as ZrF_4. Despite this, they have enhanced chemical durability and strength than ZrF_4 fibers [94] and the glass transition and melting temperature of AlF_3-based bulk glasses are 392 ℃ and 650 ℃, respectively [95], which are higher than for ZrF_4. Thanks to their higher durability against moisture, better mechanical properties and higher damage threshold, they are mostly used as delivery cables for Er:YAG and Er:YSGG lasers used in medical applications, and for capping component for fiber faces in high-power fluoride fiber lasers.

InF_3-based fibers are another type of fluoride-based fibers, providing more than 1 μm wider spectral transmission (up to 5.5 μm [88]) than ZrF_4. They also have slightly higher glass transition temperature (300 ℃) and lower phonon energy than ZrF_4. They are mainly used

in supercontinuum sources. The first InF_3-based supercontinuum source with a spectrum extending beyond 5 μm has already been demonstrated [75]. On the other hand, by using an InF_3-fiber as a host and doped with Dy^{3+} ion, fluorescence emission beyond 4 μm was also shown for the first time [96].

Lastly, since all types of fluoride-based glasses are highly reactive with liquid water, their uncoated parts should be isolated from the atmosphere in a protected moisture-free ambient enclosure purged by a noble gas such as nitrogen. Under other conditions, two of the glass components, ZrF_4 and BaF_2 start to dissolve by the atmospheric water; then the properties of glass matrix change by penetration of the water into the glass; lastly ZrF_4 crystals growth on the glass surface is observed after a certain time [97; 98].

I.3.2 Fiber Bragg gratings

FBGs are fabricated through periodic perturbation of the refractive index of the fiber core. Instead of using bulk mirrors, FBGs enable to achieve a simple, rugged and monolithic laser architecture. The grating period and the change in refractive index are the main parameters which determine the Bragg wavelength based on the following formula:

$$\lambda = 2n_{\text{eff}}\Lambda, \tag{1}$$

where λ is the vacuum wavelength, n_{eff} is the effective refractive index of the fiber mode and Λ is the period of Bragg grating. In principle, the manufacturing method is based on exposing the fiber core by using an intense light source such as a laser. Depending on the fiber and the exposure pattern, the refractive index increases or decreases with a fixed index modulation. The refractive index profile of the FBGs can be tailored in order to achieve different designs which can be either uniform, chirped, tilted, discrete phase shift or Gaussian apodized, and superstructure based on targeted laser architecture and output laser parameters. FBGs are used in communication and sensing systems such as wavelength filters, optical add-drop multiplexers, dispersion compensators, temperature and strain sensors. In fiber laser applications, they are used as wavelength selective mirrors for laser cavity by restricting the emission wavelength to a specific range. The techniques for manufacturing FBGs vary but the most common are holography, phase-mask, and point by point writing techniques.

FBGs in mid-IR fiber lasers enabled to achieve monolithic laser architectures and led to enhanced efficiency and output power. They are key components for a stable high-power laser emission from a rugged laser cavity and their optimization is crucial for limiting photo-induced losses at laser and pump wavelengths. Prior to FBG technology the output power level of fluoride fiber lasers at 3 μm were limited to 5 W-level [29]. Such systems were not robust and compact, and efficiencies were lower and output spectra were not stable. The use of FBGs in ZBLAN fiber core provided precise spectral control of the gain which led to the achievement

of record output power levels. Fiber laser cavities, in general, are bounded by a high reflective FBG (HR-FBG) and a low reflective FBG (LR-FBG). The reflection bandwidth of HR-FBG is generally chosen to be broader than LR-FBG; however it might change depending on laser configuration and fiber type.

For inscription of FBGs into the core of the fluoride-based fibers, different methods have been used until now. First, the photo-sensitivity of fluoride-based fibers has been investigated on Ce^{3+}-doped ZBLAN fibers by writing 1560 nm FBGs in fiber core through UV illumination at 246 nm [99; 100]. The demonstration of refractive index change in various bulk glasses by using femtosecond pulses at 800 nm has benefited the FBG writing process [101]. Firstly, optical waveguides were written in ZrF_4-based glasses by using 800 nm fs pulses [102]. Then the phase-mask-based FBG writing procedure in single and multimode fluoride fibers by using 800 nm fs pulses was demonstrated for the first time [103; 81]. In this technique, the laser beam is focused on the fiber core through a phase-mask and the distance between the phase-mask and fiber is chosen carefully to ensure propagation of zero-order pulses through the fiber core precedes other orders. Moreover, this technique allows mass production and the grating period is not dependent on the wavelength of the writing source and is less depended on the incident beam angle. The coherence of the laser source is also less critical and the period of the grating is determined only by the period of the mask. After that, a watt-level ZBLAN fiber laser operating at 1480 nm including FBGs based on the phase mask method written by 800 nm femtosecond pulses was reported for the first time [104]. Another FBG writing technique named as point-by-point (PbP) was used in fluoride fibers for the first time and a single-mode fiber laser operating at 2914 nm including such FBGs was demonstrated [105]. In all demonstrations above, it was necessary to strip the fiber polymer before and recoat by using appropriate polymer and UV source after the writing process. This approach is time-consuming and limits the FBG yield because it reduces the mechanical strength of the fiber. By an appropriate focusing configuration, writing FBGs through the silica fiber's coating was demonstrated for acrylate and polyimide coatings [106]. This technique was applied on fluoride and silica fibers to demonstrate high-power laser outputs [107; 108; 109]. The same approach without using a phase mask was also used into a single-mode fluoride fiber core and a wavelength tunable from 2850 nm to 2887 nm FBG-based fluoride fiber laser was demonstrated [110]. Goya et al. also demonstrated a plane-by-plane femtosecond FBG inscription process by using 517 nm pulses, without removing the fiber coating and they studied spectral and output power behaviour of the laser system at 2.8 μm [111]. Another method, named tilted fiber Bragg grating technology, was used by Bharathan et al. to write 45°-tilted FBGs into passive and active fluoride fibers and the polarization properties of such FBGs were evaluated [112].

In this project, all the FBGs used in the laser cavities were fabricated by using 800 nm fs pulses with the phase mask technique described in [81] and in [106]. The pulse energy of the

laser source was around 1 mJ at 1 kHz of repetition rate. Especially for high-power lasers, a characterization procedure of the FBGs is required. ZrF_4-based fibers show poor thermal stability after FBG writing process due to their low glass transition temperature. Depending on the maximum core temperature in laser operation, thermal annealing is necessary to stabilize FBGs' spectral response under the high-power pumping and lasing operation, and to lower losses coming from the inscribed part of the fiber. For example, as shown in the article presented in Chapter 3, a heavily-doped fiber laser cavity was used to achieve 41.6 W output power at 2.8 μm. In this work maximum temperature of fiber core under the maximum pump power was calculated to be 150 ℃ and FBGs were annealed according to this calculation for ensuring their long-term stability. FBGs were annealed at 150 ℃ for 10 min for improving their spectral response at high temperature. On the other hand, due to the annealing process, a decrease in refractive index modulation of FBGs is expected, therefore keeping the index modulation large enough for the HR-FBG is crucial before the annealing process. The reflectivity of the FBGs is chosen depending on the gain medium. For example, if the lasing wavelength is far from the peak gain of the dopant material, a higher reflectivity output FBG is required to reduce the lasing threshold. On the other hand, in high-power 3 μm laser cavities, spectral overlap between HR- and LR-FBGs is necessary to ensure stable laser operation.

I.3.3 Pump sources

The pump laser sources exciting the gain medium are fundamental components of fiber laser sources. To generate 3 μm laser emission by using different rare earth ions, choosing the optimal pump source parameters depending on absorption and energy transfer characteristics of the gain medium is required. The operating mechanism of laser diodes is based on pumping of p-n or p-i-n junctions electrically. Fiber coupled GaAs-based semiconductor laser diodes with single or multiple emitters are widely used as pump sources in fluoride fiber laser architectures thanks to their high efficiency and output power, as well as their low numerical aperture (NA), low threshold current, long lifetime, compactness and robustness. Such features of semiconductor laser diodes have made great contributions to the advancement of fiber laser technology. Especially for high-power laser applications, the efficiency of the laser diode is a crucial parameter for the non-stop industrial applications.

There are essential parameters in order to ensure an efficient laser pumping. First of all, for fiber-coupled fiber laser diodes, if a splice between the pump and laser cavity is required, the NA of the pump source should be matched with that of the cavity fiber for efficient pump light coupling. The pump wavelength should cover the absorption band of the active ion sufficiently with suitable pump energy for inducing the laser transition. In addition, its bandwidth should be chosen depending on the medium. The pump energy and spectral noise is another factor which affects the laser output power stability. The brightness of the pump source has an effect on the efficiency and compactness of the optical design so it is critical to use high-brightness

pumps to have a stable and short gain media.

Most of the multi-mode semiconductor pump laser diodes have the tendency to shift their central wavelength to longer wavelengths, as their temperature and charge density increase [113]. Increasing the electrical current of such diodes, to obtain higher pump power levels, increases the junction temperature, which causes a shift in wavelength. The wavelength shift parameter of laser diodes is provided by the manufacturer and is around 1 nm/A in general i.e. proper cooling conditions are respected. The change in wavelength during the laser operation affects the photon transfer mechanism in the active medium, especially if the medium is heavily doped, and might create slope efficiency problems. For instance, in Er^{3+}:ZrF_4 fibers, the pump source operating around 975 nm is absorbed by ground state absorption (GSA) ($^4I_{15/2} \rightarrow {}^4I_{11/2}$), which is the higher energy level of the 3 μm laser transition. Absorption via excited state absorption (ESA) on the $^4I_{11/2} \rightarrow {}^4F_{7/2}$ transition (e.g. Fig. I.7) is also observed. GSA and ESA have similar cross-sections around such pump wavelength and ESA might limit the output power because it lowers the number of ions in the higher laser transition level ($^4I_{11/2}$). In addition, after the absorption of ions to the $^4F_{7/2}$ level by ESA, they are recycled to $^4I_{11/2}$ level by subsequent multiphonon relaxation, which increases the core temperature. Hence, choosing a proper pump source wavelength or optimizing the wavelength by changing the diode temperature, where ESA is the lowest and GSA is the optimum, to keep the fiber temperature minimum and slope efficiency maximum, is important. Numerical simulations show the optimum wavelength for pumping this system is located around 983 nm [114]. Today, precisely controlled wavelength stabilized diodes based on volume Bragg gratings (VBGs) are commercially available at high output power levels and could be used instead of diodes with an unstable broad spectrum.

On the other hand, the central wavelength of some pump sources to use in 3 μm laser cavities might not be commercially available or be power limited. For instance, in singly doped $Ho^{3+}ZrF_4$- or co-doped Ho^{3+}, Pr^{3+}-based systems, 3 μm is generated from the $^5I_6 \rightarrow {}^5I_7$ transition. The direct excitation of the $^5I_6$ level is possible by GSA around 1150 nm. However, diodes operating at such wavelengths are power limited although Yb-silica or Raman fiber lasers operating around 1100 nm can be used as a pump source [115; 43]. Similarly, in-band pumping of Dy^{3+}-doped fluoride fiber laser emission around 3 μm through pumping with another fiber laser source operating around 2.8 μm, which is not commercially available, was reported [51].

To sum up, pump sources have a critical importance for the lasers and amplifiers and their optical parameters should be considered during the laser design.

I.3.4 Fluoride fiber splices

Fiber splicing of two fibers is one of the most important fabrication steps of the development of fiber lasers. The aim of the splicing process is to achieve a compact laser architecture with higher transmission efficiency with reduced parasitic lasing. Two methods, mechanical and fusion splicing, are generally used. In the mechanical splice method, fibers are not permanently joined together, instead they are just held together in a precisely aligned position. For this reason, insertion loss is higher than the fusion splicing method along with the significant reduction of the mechanical robustness. In the fusion splicing method, the glass faces are fused together by using a filament, laser or electric arc discharge; hence the connection between the fibers enables low insertion losses and ensure high mechanical robustness.

Splicing of silica fibers is easy and well-known because of their high mechanical strength and large difference between the melting temperature and crystallization temperature of silicate glass. On the other hand, fluoride to silica splices are difficult because of their significant chemical composition difference and softening temperature contrast (265 ℃ for fluoride, 1175 ℃ for silicate [89]). In addition, the temperature range for changing from solid to liquid phase has an effect on achieving a good quality splice. However, this range for ZBLAN fibers is around 90 ℃, while it is more than 300 ℃ for silica fibers [116] so precise control of the splice temperature is essential for a good quality splice involving between fluoride fibers. Moreover, especially in high-power laser operation around 3 μm, splice losses should be kept quite low because fiber protecting coating based on low index fluoro-acrylate polymers has high absorption around 3 μm. The heat control precision of the fusion area varies according to the heat source technology. In 1976, splicing by electric arc was shown for the first time and then arc splicers have made great progress [117]. The arc splicers are based on creating a heat zone by a current flow generated between two electrodes. The generated temperature by such technology is generally high (>1000 ℃) and turn-on and -off characteristics of arc discharges lack of precise control. Nowadays, arc splicers with three electrodes technology provide a wide plasma area with more controlled temperature and zone area, allowing to splice ZrF_4 fibers to each other. Fusion splicing of fluoride fibers was also achieved by using CO_2 lasers in laboratory environment [118]. Then splicers with absorptive CO_2 laser-based process was developed recently, and have been used for splicing of fluoride-based fibers, as well as for silica fibers [119]. With commercially available laser glass processing stations, the temperature can be precisely adjusted and distributed uniformly. Besides such technologies, another common splicing method consist of using a filament-based splicer because it can achieve well-controlled heat region and over time duration ability of tungsten filament. In a very short heating time, the temperature of the fusion zone can be changed during the splicing process, which enables repeatable splicing recipes. In all technologies, ambient conditions such as atmospheric OH, temperature, dust, may affect the heat source and fusion splice by causing crystallization of the ZrF_4 fiber. Thus, for the protection of the heat source and the fiber, a low vacuum or high

purity noble gas ambient environment is required during the splicing process.

During the splicing procedure, the preparation of the tip of the fluoride fiber must be realized correctly to minimize the transmission losses without degrading the quality of the beam. There are several steps to achieve a dust-free, low-loss fluoride to fluoride fiber splices. The first step involves removing the acrylate coating from the fiber glass by using chemicals such as dichloromethane. After applying the chemical materials, the coating of the fiber could be removed by using lint-free wipes with isopropyl alcohol or acetone. Remaining particles from the polymer and dust should be completely eliminated from the stripped glass surface. Then the fiber is cleaved by creating a crack propagating through the fiber until it breaks by using a blade with applying a controlled tension along the length of the fiber, which depends on the fiber diameter and material [120]. The accuracy of the applied tension on the fiber has an effect on the quality of the fiber end face and it is important to maintain a low tension variation during the cleave process. There are industrial cleavers in the fiber optics market such as the Fujikura CT-104, Vytran LDC 401, Nyfors LDF-M providing adjustable tension with small variations. The angle of the cleave should be close to zero degree, while the shape of the fiber end should be crack-free for increasing the chance of achieving low-loss fusion splices. Then, parameters of the splicer such as splice power, hot push distance of the fibers, offset values of heat source, the gap between the fibers and splice time are optimized. The splice results of fluoride-based fibers can be considerably affected by small changes of such parameters, especially the amount of heating and temporal behaviour of the heat source, due to their small phase change temperature difference from solid to liquid. Especially in single-mode to single-mode fluoride fiber splices, it is crucial to choose these parameters precisely to preserve the alignment of the fiber cores during the heating process.

After determining the parameters, two fibers are aligned together either core to core or clad to clad depending on the type of splice. Then, a heat zone generated by an electric arc, laser absorption or a filament, is applied to the gap between two fibers or at a different position depending on the fiber types. The last step of splicing is to test the mechanical strength of the splice point by measuring the tension up to a safe value and measure the transmission losses at the operating wavelength.

One of the most critical splice types is fluoride to silica fibers because it allows achieving monolithic 3 μm fiber laser systems [44; 50] by eliminating free space pump coupling, namely allowing to create a junction between fiber output of the pump source and fluoride fiber of the laser cavity. However, the large melting temperature mismatch between fluoride and silicate glasses makes it difficult to achieve. In recent years, many different works have been realized to develop methods for splicing a fluoride to a silica fibers but there is still room for improvement.

After achieving a low-loss splice between two different fibers based on different materials by NP Photonics, Inc. [121], many attempts were demonstrated to achieve ZBLAN to silica fiber

splices. Li et al. showed a joint between ZBLAN and silica fibers at a minimum loss of 0.14 dB [122]. In this demonstration, by using a low stable arc splicer, a 7.8/125 μm fluoride fiber is spliced to a 4.3/125 μm silica fiber, then fixed by gluing with an optical adhesive. A novel method was reported by Okamato et al. by splicing a Pr^{3+}-doped ZBLAN fiber to a silica fiber coated with a dielectric thin film [123]. In this demonstration, an ion assisted deposition process is used to coat a 3.5/125 μm silica fiber to increase the adhesion with a 3.6/125 μm ZBLAN. Then, a mechanical splice of single-mode ZBLAN fiber was demonstrated with a transmission loss of 0.5 dB between a 3.1 μm silica and 2.4 μm ZBLAN fiber [116]. Another thermal splicing method was also shown by Zhi-Jian et al. with a splicing loss of 0.58 dB [124]. In this demonstration, a ZBLAN fiber (9/125μm) is spliced to an SMF-28 silica fiber by using a filament-based splicer. Huang et al. also demonstrated a thermal splicing of ZBLAN (2.7/123 μm) to silica fiber (3.4/125 μm) and achieved 0.3 dB repeatable loss by using a filament splicer [125]. In this research, the position of the filament is set closer to the silica fiber, which has an end face temperature greater than the ZBLAN melting point. Hence, by softening the ZBLAN fiber and contacting it to the silica fiber end, the ZBLAN fiber melts and bonds with the silica fiber end. Lastly, Carbonnier et al. demonstrated a splice between a ZBLAN (8.6/125 μm) and different 80 μm cladding silica fibers by a CO_2 laser glass processing station [119]. In this research, the silica fiber is encapsulated by the ZBLAN fiber by using the ZBLAN's high thermal expansion coefficient and an average transmission loss of 0.225 dB was achieved.

Different parameters and different techniques were used to achieve repeatable low loss splices

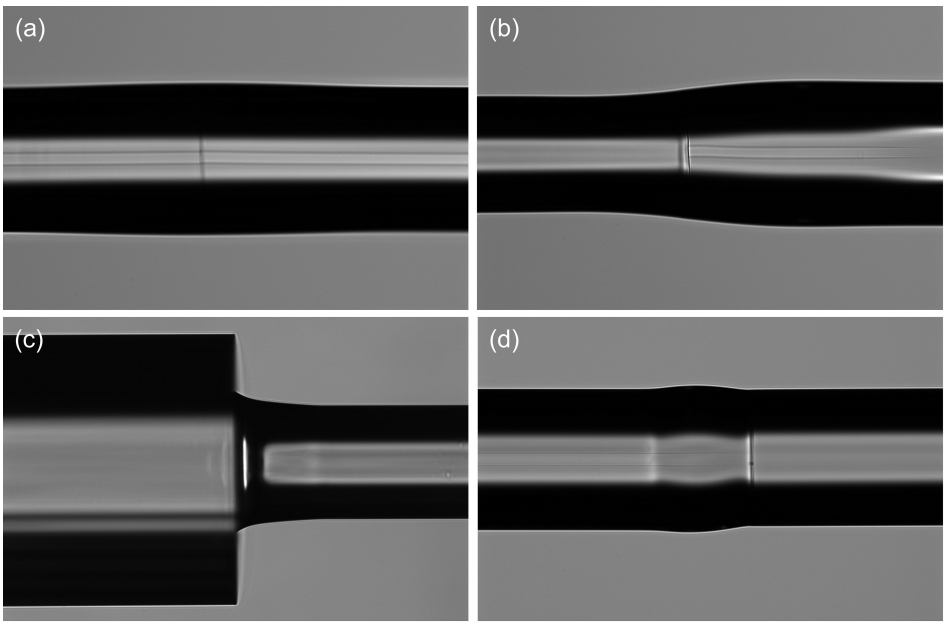

Figure I.5: Example of splices between (a) single-mode ZrF_4 fibers with same clad sizes, (b,c) ZrF_4 fibers with different core and clad sizes, and (d) splices between SiO_2 and ZrF_4 fibers by dielectric coating.

in all studies reviewed above. In this research, splicing of different fiber types was also achieved by using the techniques described above as well as by new methods with the Vytran GPX-3400 splicer containing an omega-shaped iridium filament. In Chapter 1, instead of using a silica to fluoride splice, the fluoride fiber was butt-coupled with the silica fiber. In Chapter 2, the single-mode fluoride fibers of the laser amplifier with different clad sizes were spliced and less than 0.2 dB of losses were achieved. In Chapter 3, silica to fluoride fiber splice was achieved by improving the adhesion through deposition of a dielectric coating on the cleaved silica fiber face by magnetron cathodic sputtering prior to the fusion splicing process as described in [123]. A new fluoride-based fiber to oxide-based fiber splice method is demonstrated in Chapter 4 by offsetting the longitudinal position of the filament in the direction of the oxide fiber and pushing it into the fluoride fiber in a controlled manner, then creating a joint wrapped by fluoride glass [126]. Some of the examples of different types of splices such as single-mode fluoride fibers with same and different clad sizes, fluoride to silica fiber, taken during the PhD project, are shown in the Fig. I.5.

I.3.5 Endcapping components

Endcaps are another important fused component used in fiber laser systems to reduce the power density at the output fiber face and the Fresnel reflection feedback in the laser cavity. A short segment of coreless or larger core size fiber is spliced to the output fiber of the laser cavity in high-power or high energy fiber laser systems to protect the fiber end facet from potential damages. While the output power and pulse energy of fiber laser systems increase, the need for such kind of endcaps also increases. The optical damage threshold and thermal failure are the main reasons to use such endcaps in infrared fiber laser systems. Such failures are caused by laser absorption by microscopic irregularities in the interface between air and fiber in CW fiber laser systems. In pulsed systems, dielectric breakdown at the atomic level and thermal effects can be the reason for fiber facet failure. However, in fluoride glass-based high-power laser systems, beside such failure types, OH-diffusion related degradation is the main reason for the fiber facet damage. OH diffusion in the fiber facet is due to the high reactivity of fluoride-based glasses with atmospheric water, especially under 3 μm laser operation. Hence, besides the increasing of optical damage threshold and reducing Fresnel reflection, reducing the thermal runaway of the fluoride fiber facet due to OH degradation by endcaps is necessary for unpurged and unsealed fiber laser systems. Consequently, endcap fabrication without degrading the beam quality is a key process in high-power 3 μm fiber laser development.

The fabrication process of fluoride fiber lasers consists in low loss splicing, cutting, tapering or polishing the spliced part with proper equipment in order to modify its length or thickness. Precisely adjusting the heating zone is a crucial step in the splicing procedures since the endcap fiber is more stable and its core size is bigger than the output fiber of the laser. Hence the

position of the heating element might need to be shifted toward the endcap fiber. In fluoride fiber end capping, after achieving a splice between the output fiber of the laser and the endcap fiber, as discussed in fluoride fiber splices section (I.3.4), a cleaving procedure is necessary to avoid beam clipping and to sufficiently reduce the laser intensity at the end facet of the fiber. The length of the endcap is determined based on the need for the intended beam clipping and beam quality parameters. If it is necessary to further reduce the effect of the Fresnel reflection on laser feedback, the fiber should be cleaved with a proper angle. After the cleaving process, the end facet of the endcap is controlled by a high-resolution CCD imaging camera or a microscope and cleaned by ultrasonic cleaner or chemicals with lint-free wipes. In high-energy and high-output power fluoride systems operating around 3 μm, different materials are used as an endcap depending on the output power and the operation type of the laser system. Coreless and undoped versions of ZrF_4 based fibers might be one of the options as an endcap due to the matched refractive index and easy splicing. However, the performance of such endcaps was studied and it was shown that they are not sufficient for laser systems operating at an output power higher than a few watts due to their low thermal degradation threshold [127; 50]. Instead, they could be used in low-power pulsed systems since they have a lower splice interface reflections due to the matched refractive index.

AlF_3-based fluoride glass fibers are another option due to their higher chemical durability and mechanical strength compared to ZrF_4-based fibers [128]. Even though they might be a suitable solution for 3 μm fiber laser systems as an endcap, their long-term performance for the power levels higher than about 5 W without OH degradation is limited [50].

Germanate-based fibers (GeO_2) are another option as an endcap because of their higher damage threshold and higher transition temperature than fluoride-based fibers, making them mechanically robust and thermally stable. They are already used as delivery fibers in solid-state Er:YAG lasers operating at 2.94 μm [129]. They could be classified as a potential endcap for the high-power 3 μm fiber lasers, however, their high refractive index ($\sim$ 1.83) causes large splice interface reflection which could affect the stability and output power of the laser system.

Al_2O_3 fibers are also used in biomedical applications as a transfer fiber from 2.94 μm Er:YAG laser to the patient [54; 56], thanks to their bio-inert properties, low transmission losses feature and very high melting temperature properties.

Other types of oxide and crystalline fibers such as silica, single Al_2O_3-crystal and single YAG-crystal fibers have the potential to be an endcap component of high-power 3 μm fiber laser systems. Their performances are studied along with non-oxide endcap components and discussed in Chapter 4.

I.3.6 Other components

There is still room for the development of new components with fluoride-based fibers despite their fragility and low glass transition temperature. Today, many of the bulk optical elements for free-space alignment such as mirrors, lenses, beam splitters, wave plates, filters, diffraction gratings are commercially available. The laser isolators working around 3 μm to protect the active lasing region from parasitic effects have started to be commercially available but they are power-limited and not fiber-coupled which requiring free space alignment [130]. Pump combiners are one of the most important components for fiber laser technology to achieve high-power output levels, and first studies of high-power fluoride-fiber-based combiners based on side coupling of the pump source have been demonstrated recently [131]. Using ZBLAN fibers, development of single-mode couplers with high insertion losses was also demonstrated [132]. Although the experimental progress of couplers and combiners, they are still laboratory prototypes and need time to become stable and robust commercialized components. Germanium-based acousto-optic modulators are also commercially available and used in actively Q-switched mid-IR laser systems operating around 3 μm [133].

The fluoroacrylic polymers are used as a recoating material to cover the stripped region of spliced parts or as cladding pump stripper to eliminate the residual pump from the laser cavity. However, most of the fluoroacrylic polymers have strong absorption around 3 μm ($\approx$ 20-200 dB/mm) which might cause local hot spots on the coated part due to scattered laser signal; hence it is crucial to develop 3 μm versions of such polymers with low absorption.

The fused version of wavelength division multiplexers, circulators, isolators, band-pass filters and single-mode couplers still do not exist and their availability on the market will highly depends on advances in the manufacturing of ZrF_4 fibers.

I.4 Laser transitions of rare-earth ion dopants

The spectral range of laser emission from a fiber host is determined by the rare-earth dopant of the active gain medium. The most suitable rare-earth ions for 3 μm emission are Er^{3+}, Ho^{3+} and Dy^{3+} and their emission cross-sections are presented in Fig. I.6. The Er^{3+} ion has an emission range from 2.7 to 3 μm and is the most used rare-earth ion for mid-IR laser generation in fluoride glasses. The advantage of the Er^{3+} ion is that it allows direct pumping of the upper laser transition level $^4I_{11/2}$ via high-power common diodes operating around 975 nm. The Ho^{3+} ion has a narrower emission range and higher gain around the water absorption peak than Er^{3+}; its upper laser level absorption is around 1150 nm, which leads to a higher Stokes efficiency than 980 nm for Er^{3+}. The Dy^{3+} ion, on the other hand, allows a laser emission range from 2.6 to 3.4 μm and the upper laser level's absorption band is also around 3 μm which enables in-band pumping to achieve high Stokes efficiencies. In this section, the spectroscopy and lasing characteristics of these three rare-earth ions will be detailed.

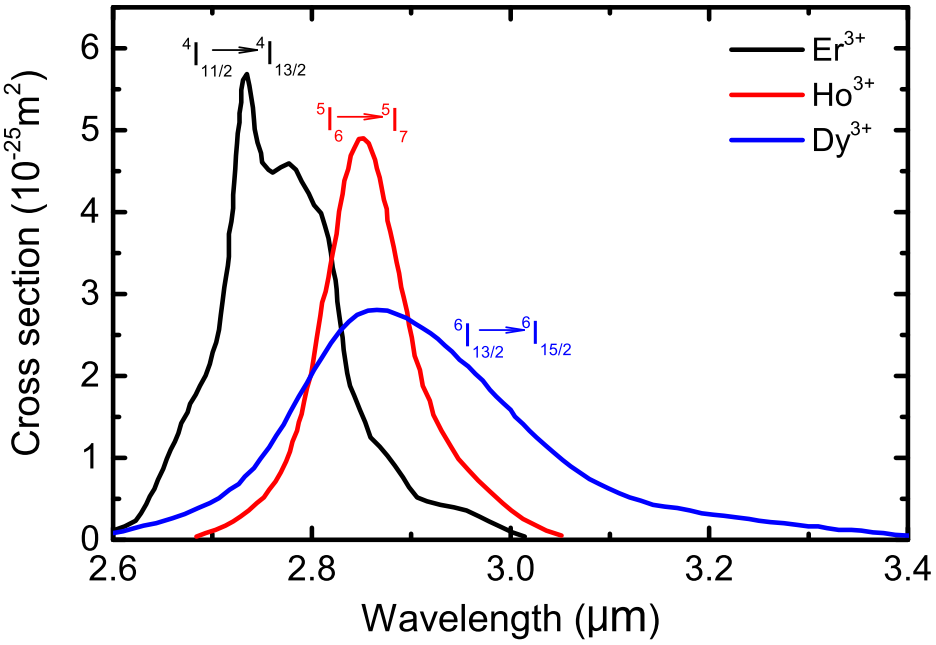

Figure I.6: Emission cross-sections of rare earth ions for 3 μm laser emission in Er^{3+}:ZrF_4 fibers.

I.4.1 Erbium as a gain medium

In Er^{3+}-based fluoride fiber laser systems, 3 μm emission is generated by the $^4I_{11/2} \rightarrow {}^4I_{13/2}$ transition. For this transition, it is required to use a pump wavelength with higher energy than laser wavelength since the transition is located above the ground state. The most efficient excitation of ions from the ground state is direct pumping of the $^4I_{11/2}$ level. In addition to this, the 3 μm transition is self-terminating since the lower energy state ($^4I_{13/2}$, 9 ms) has a longer lifetime than to the upper energy state ($^4I_{11/2}$, 6.9 ms). Therefore, different methods with different approaches are required to overcome bottleneck problem of the 3 μm laser transition in Er^{3+}:ZrF_4-glasses. Three main methods exist : (1) enhancing population inversion in the $^4I_{11/2}$ level by energy recycling based on energy transfer upconversion (ETU) [114], (2) depopulation of $^4I_{13/2}$ level by cascade operation of both 1.6 μm and 2.8 μm [134], (3) desensitization of the $^4I_{13/2}$ level by introduction of Pr^{3+} co-dopant used to achieve an efficient 3 μm emission from Er^{3+}:ZrF_4 medium [135]. In this section, the theoretical basis of such approaches for generating of 3 μm in Er^{3+}:ZrF_4 will be discussed.

Energy transfer by upconversion

Energy recycling by ETU ($^4I_{13/2}$, $^4I_{13/2} \rightarrow {}^4I_{15/2}$, $^4I_{9/2}$) in Er^{3+}:ZrF_4 media provides an efficient way to overcome the bottleneck problem (see Fig. I.7 for the energy level diagram of Er^{3+} ion). By this process, half of the ions are transferred to the $^4I_{9/2}$ level and the other half are to the $^4I_{15/2}$ level, therefore enabling population inversion in $^4I_{11/2}$ level. ETU is based

on multipole-multipole interaction, in which closely spaced ions interact with each other to exchange energy. Therefore, it is necessary to have high ion concentrations to achieve efficient energy migration between ions. First, after the excitation of the ions to the upper states by GSA, the ion-ion interaction based on ETU occurs at $^4I_{13/2}$ level. Then, the conversion of ions from $^4I_{13/2}$ to $^4I_{9/2}$ level by ETU provides a fast depletion of the lower laser level. Lastly, up-converted ions in $^4I_{9/2}$ level are recycled to the $^4I_{11/2}$ level by multiphonon relaxation processes and contributes to population inversion for 3 μm laser transition.

Energy recycling by ETU approach was used to demonstrate effective 3 μm laser transition in heavily doped Er^{3+}:ZrF_4 fibers. The first 3 μm fiber laser based on this approach was demonstrated by Poppe et al. in a single-mode 1 mol.% Er:ZBLAN fiber pumped at 980 nm and 12 mW output power at 2.7 μm was achieved [18]. Then, the same research group has increased the doping concentration of the fiber up to 2 mol.% and achieved 400 mW of output power at 2.7 μm with a slope efficiency of 16% with respect to the absorbed pump power at 791 nm [20]. The first watt-level (1.04 W) fluoride fiber laser at 2.8 μm was demonstrated by using a 5 mol.% Er^{3+}:ZrF_4 fiber which enabled a slope efficiency of 25% with respect to the launched pump power at 970 nm [21]. Later, a free-running 6 mol.% Er^{3+}:ZrF_4 fiber laser achieving a 10-W-level output power with a 21.3% slope efficiency was demonstrated, where the configuration showed fluctuations and shifts from CW to pulsed operation [31]. Subsequently, a 120 nm tunable version of the same configuration at 2 W was developed [30]. By the advance of FBG and fluoride fiber fabrication, 5 W-level 3 μm-class highly-stable lasers based on the energy recycling approach with slope efficiencies higher than 30% with respect to absorbed pump power at 976 nm was developed by using a heavily doped (7 mol.%) single-mode Er^{3+}:ZrF_4 fiber [35; 36]. Tokita et al. demonstrated 24 W of output power at 2.8 μm from a multi-mode 6 mol.% Er^{3+}:ZrF_4-based cavity [37]. It is possible to exceed the Stokes limit by recycling the ions to upper laser transition level through ETU process in $^4I_{13/2}$ level. The first single-mode 20-W-level 3 μm-class laser was demonstrated by Faucher et al. by using a 7 mol.% Er^{3+}:ZrF_4, in which energy recycling by ETU process was confirmed for the first time by exceeding the Stokes limit. The output power in this study was 20.6 W at 2.825 μm and the slope efficiency with respect to absorbed pump power at 976 nm is 35.4%, where the theoretical Stokes efficiency is 34.3% [38]. Later, through optimized FBGs, 27 W of output power at 2825 nm was achieved from a monolithic laser cavity [42]. Then, a 30.5 W single-mode all-fiber fluoride fiber laser at 2.94 μm was demonstrated by Fortin et al., in which the slope efficiency with respect to launched pump power was lower than in previous similar laser cavities due to the low gain of Er^{3+} around 2.94 μm. A splice-less version of the 2.82 μm cavity delivering about 20 W of output power was achieved by using a piece of heavily-doped Er^{3+} fiber bounded by FBGs written inside of active fiber [108]. Using the same approach, 41.6 W output power at 2.824 nm from a 7 mol.Er^{3+}:ZrF_4 fiber was recently achieved via optimization of the FBGs, the central wavelength of the pump diodes and by using bi-directional pumping [50]. This study is detailed in Chapter 3.

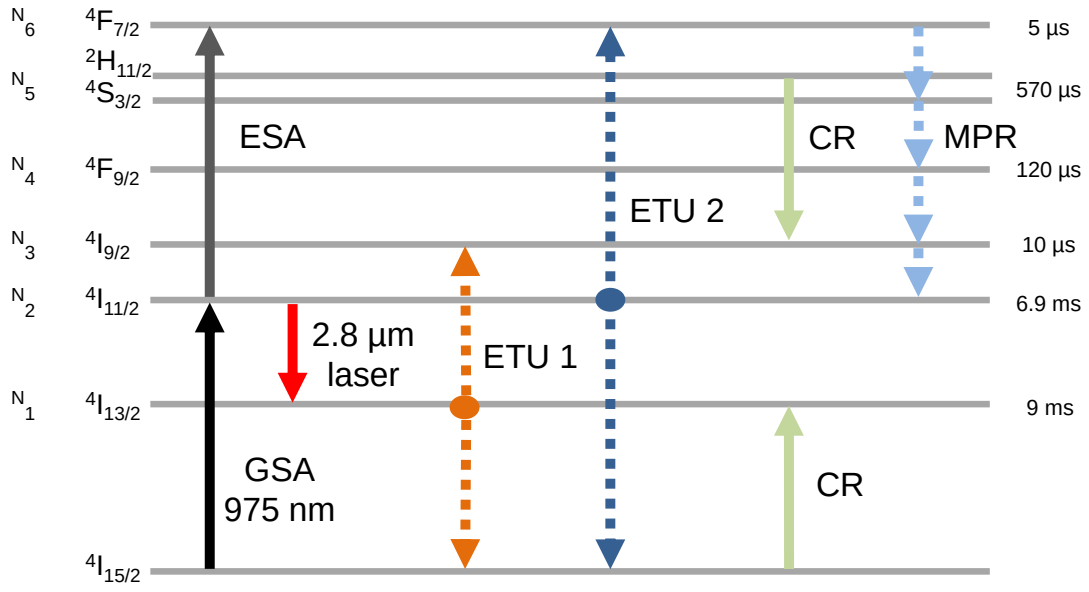

Figure I.7: Simplified energy level diagram of heavily-doped Er^{3+}:ZrF_4 fiber: CR, cross-relaxation; MPR, multiphonon relaxations.

Watt-level pulsed demonstrations in heavily doped Er^{3+}:ZrF_4 fibers benefiting from ETU were also demonstrated by Q-switched and gain-switched cavities. A 2 W average power gain-switched laser producing 300 ns pulses with 20 μJ pulse energy was demonstrated by using a heavily doped (6 mol.%) Er^{3+}:ZBLAN fiber [136]. By using a similar fiber in a Q-switch configuration, Tokita et al. demonstrated a 12 W laser producing 100 ns pulses with a pulse energy of 100 μJ [137]. Then, the advances in FBG technology have enabled to build 5- and 10-W-level monolithic gain-switched Er^{3+}:ZrF_4 fiber laser cavities producing ns pulses [109; 138]. Besides, the amplification of the pulses in heavily-doped Er^{3+}:ZrF_4 fiber seeded by an external pulsed source was demonstrated. An OPA seeded amplifier based on a 6 mol.% Er^{3+}:ZrF_4 fiber medium has produced 840 mW of output power and 24 ps pulses with 84 μJ pulse energy, which corresponds to 350 kW of peak power [139]. After, by using a Q-switched Er^{3+}:ZrF_4 fiber laser as a seed, 4.2 W of output power with 2.3 μs pulses at an energy of 59 μJ was achieved from a MOPA (master oscillator power amplifier) system based on 7 mol.% Er^{3+}:ZrF_4 fiber [140].

The simplified energy level diagram of the heavily-doped Er^{3+}:ZrF_4 system is shown in Fig. I.7. Theoretically, it is possible to achieve 50% of optical to optical conversion efficiency by the recycling process of $^4I_{13/2} \rightarrow {}^4I_{9/2} \rightarrow {}^4I_{11/2}$ with high Er^{3+} concentrations [141]. This is because of the increase in the quantum efficiency of pump photon conversion into laser photon in the recycling process. However, the maximum efficiency achieved from a heavily-doped Er^{3+}:ZrF_4 fiber laser is 35.4% [38]. As shown in Fig. I.7, besides ETU originating from

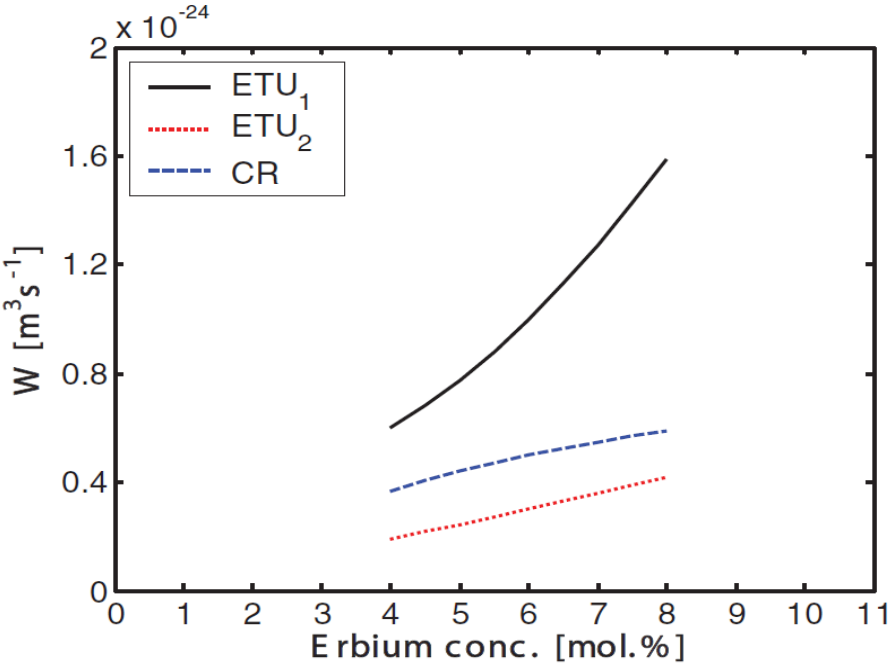

Figure I.8: Estimated rate parameters for ETU_1, ETU_2 and cross relaxations as a function of Er^{3+} concentration in Er^{3+}:ZrF_4 fibers. Figure taken from [114].

$^4I_{13/2}$ level, there are other ETU processes as well as excited state absorption (ESA), cross-relaxations (CR) and multiphonon relaxations (MPR). The ETU_2 process ($^4I_{11/2}$, $^4I_{11/2} \rightarrow$ $^4I_{15/2}$, $^4F_{7/2}$) reduces the population density in the $^4I_{11/2}$ level hence resulting in a decrease in the slope efficiency and increase in the threshold pump power. Besides, excitation of the $^4F_{7/2}$ level by ETU_2 leads to non-radiative decays through MPR originating from this level which increase the fiber core temperature. Nevertheless, the transition rate of ETU_2 is much lower than ETU_1, and the ETU_1/ETU_2 ratio is stable when increasing the absorbed pump power [114]. The rates of ETU_1 and ETU_2 can be defined as [114]

$$R_{ETU_1}(z,t) = W_{11}N_1^2(z,t) \tag{2}$$

$$R_{ETU_2}(z,t) = W_{22}N_2^2(z,t) \tag{3}$$

where W_{11} and W_{22} are the parameters for ETUs and have a unit of [m^3s^{-1}] which increase by increasing doping concentration. N_i is the population density of corresponding energy levels. The estimated ETU parameters as a function of Er^{3+} concentration in Er^{3+}:ZrF_4 fiber is given in Fig. I.8 and energy transfer parameters for weakly and strongly interaction conditions are given in Table I.1.

Through GSA at 975 nm, ions are excited to the $^4I_{11/2}$ level, where the ESA cross-section overlaps the GSA at 975 nm and excites the ion to the $^4F_{7/2}$ level. ESA in Er^{3+}:ZrF_4 fibers

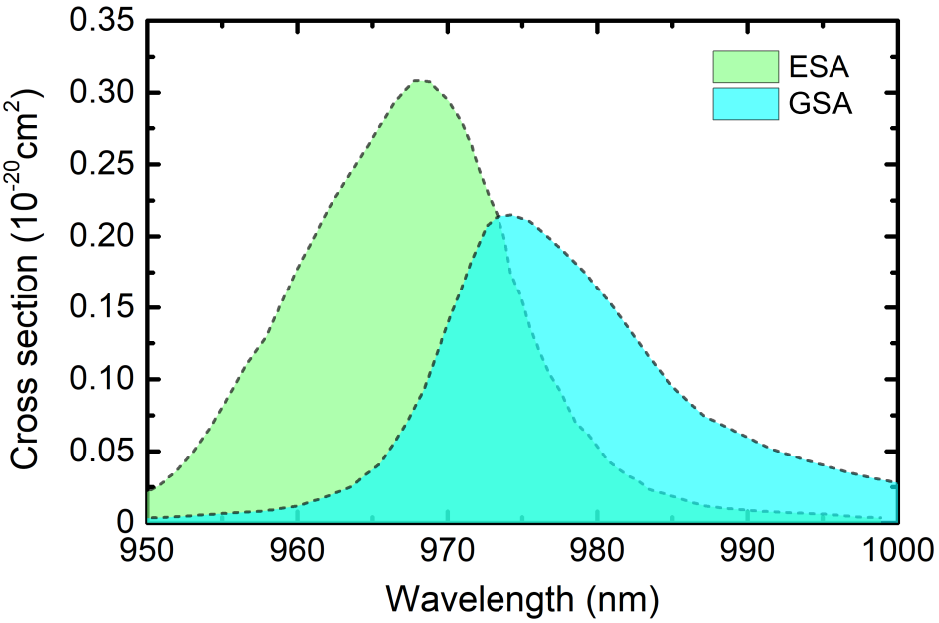

Figure I.9: Cross-section spectra of GSA and ESA in Er^{3+} fluoride glass. Figure retrieved from [142].

has an effect on the output power and fiber core temperature. As shown in the cross-section spectra of GSA and ESA in Fig. I.9, ESA is more dominant than GSA at a wavelength shorter than 975 nm. This situation has an effect on the slope efficiency of highly-doped media because it is observed that the variation of ETU_1 is similar to the variation of GSA [114]. It is also shown that the slope efficiency of the heavily-doped Er^{3+}:ZrF_4 fiber lasers depends on central wavelength of the pump diode and reaches its maximum value around 983 nm then decreases at longer pump wavelengths [114]. This phenomenon is due to the fact that the ETU_1 variation is similar to the GSA's cross-section variation, thus the longer the wavelength the higher the GSA and ETU_1. On the other hand, increasing the ESA also increases multiphonon relaxation from $^4F_{7/2}$. Hence, the temperature of the active medium is lower at longer pump wavelengths. The temperature behaviour of a heavily-doped fiber core with respect to the pump wavelength is investigated in Chapter 3. Besides of the cross-sections, the pump wavelength and power, ESA and GSA rates depend on fiber geometry and active pumping area. The ESA and GSA rates can be defined as

$$R_{ESA}(z,t) = \frac{\lambda_p \Gamma_p \sigma_{ESA}}{hcA_{core}} N_2(z,t) \times \left[P_p^+(z,t) + P_p^-(z,t)\right] \tag{4}$$

$$R_{GSA}(z,t) = \frac{\lambda_p \Gamma_p \sigma_{GSA}}{hcA_{core}} N_0(z,t) \times \left[P_p^+(z,t) + P_p^-(z,t)\right] \tag{5}$$

where, λ_p is the pump wavelength, σ is cross-section of ESA or GSA, Γ_p is the A_{core}/A_{clad} (pump filling factor), h is the Planck's constant, c is the speed of light, A_{core} is the fiber core

area, P_p^+ is the forward pump power, P_p^- is the backward propagating pump power.

Another process in Er^{3+}:ZrF_4 medium is cross-relaxation (CR) ($^2H_{11/2}$, $^4I_{15/2}$) $\rightarrow$ ($^4I_{9/2}$, $^4I_{13/2}$) from $^2H_{11/2}$ and $^4S_{3/2}$ thermally coupled levels. As in ETU_1 and ETU_2 rates, the rate of cross-relaxation increases with increasing Er^{3+} concentration. The CR rate is given by [135]

$$R_{CR}(z,t) = W_{CR} N_5(z,t) N_0(z,t) \tag{6}$$

where W_{CR} is CR parameter which increases with increasing Er^{3+} concentration (Fig. I.8), N_i is the population density of i^{th} energy level. CR parameters for weakly and strongly interaction conditions are given in Table I.1. Lastly, the stimulated emission of laser transition ($^4I_{11/2} \rightarrow$ ($^4I_{13/2}$) could be defined as

$$R_{SE}(z,t) = \frac{\lambda_s \Gamma_s}{hcA_{core}} \left[N_2(z,t)\sigma_{ems} - N_1(z,t)\sigma_{abs}\right] \times \left[P_s^+(z) + P_s^-(z,t)\right] \tag{7}$$

where λ_s is the laser wavelength, Γ_s is the power filling factor, σ_{ems} and σ_{abs} are the emission and absorption cross-sections at laser wavelength, respectively, P_p^+ is the forward signal power, P_p^- is the backward signal power.

Based on all processes mentioned above, the temporal dependency of the energy populations for a heavily-doped Er^{3+}:ZrF_4 fiber laser can be written as below. In the rate level equations, ground state ($^4I_{15/2}$) indicated as zero level and $^4F_{7/2}$ defined as the sixth level since $^2H_{11/2}$ and $^4S_{3/2}$ are thermally coupled so as they represent together the 5th level.

$$\frac{dN_6(z,t)}{dt} = R_{ESA}(z,t) - \tau_6^{-1} N_6(z,t) + R_{ETU_2}(z,t) \tag{8}$$

$$\frac{dN_5(z,t)}{dt} = \beta_{65}\tau_6^{-1} N_6(z,t) - R_{CR}(z,t) - \tau_5^{-1} N_5(z,t) \tag{9}$$

$$\frac{dN_4(z,t)}{dt} = \sum_{i=5,6} \left[\beta_{i4}\tau_i^{-1} N_i(z,t)\right] - \tau_4^{-1} N_4(z,t) \tag{10}$$

$$\frac{dN_3(z,t)}{dt} = \sum_{i=4,5,6} \left[\beta_{i3}\tau_i^{-1} N_i(z,t)\right] + R_{ETU_1}(z,t) + R_{CR}(z,t) - \tau_3^{-1} N_3(z,t) \tag{11}$$

$$\begin{aligned}\frac{dN_2(z,t)}{dt} = &\sum_{i=3\ldots6} \left[\beta_{i2}\tau_i^{-1} N_i(z,t)\right] - R_{ESA2}(z,t) - R_{SE}(z,t) - 2R_{ETU_2}(z,t) \\ &+ R_{GSA}(z,t) - \tau_2^{-1} N_2(z,t)\end{aligned} \tag{12}$$

$$\frac{dN_1(z,t)}{dt} = \sum_{i=2...6} \left[\beta_{i1}\tau_i^{-1}N_i(z,t)\right] + R_{SE}(z,t) + R_{CR}(z,t) - 2R_{ETU_1}(z,t) - \tau_1^{-1}N_1(z,t) \tag{13}$$

$$N_{core} = \sum_{i=0,...6} N_i \tag{14}$$

where, τ_i is the intrinsic lifetimes of the energy level, β_{ij} are the branching ratios from i-level to j-level. The values of the all parameters can be found in [114] and [141]. Branching ratios for Er^{3+} system are given in Table I.1.

Cascade operation

The cascade operation of a laser, also known as cooperative lasing, aims to increase the population inversion by depopulating the lower laser level via another laser transition in order to overcome population bottleneck. Depending on the lasing configuration, it could also be the contribution of the population inversion of a laser transition located at the lower level by depopulation of the higher level with another laser transition. In Er^{3+}:ZrF_4-based fiber lasers, cascaded lasing of 1.6 μm is used for depopulating the $^4I_{13/2}$ level to achieve population inversion on the $^4I_{11/2} \rightarrow {}^4I_{13/2}$ transition at 2.8 μm as seen in Fig. I.10. Unlike energy recycling by ETU approach, cascaded operation provides the advantage of not requiring high-concentration Er^{3+}-doped fibers to enable high laser efficiencies while maintaining low core temperature. However, using low Er^{3+} concentrations results in increasing the fiber length in order to achieve sufficient pump absorption which causes higher costs and an increase in background loss. Hence, choosing an optimal concentration and fiber geometry is crucial for effective cascade laser operation.

The cascade lasing approach in fluoride fibers was used for the first time by Ghisler et al. and output power of 4.7 mW at 1.71 μm and about 24 mW at 2.7 μm were achieved by using an Er^{3+}:ZBLAN fiber [15]. In this demonstration, a pump wavelength of 791 nm was used to populate $^4I_{9/2}$ level by core pumping and instead of depopulation of $^4I_{13/2}$ level, co-lasing of 1.7 μm laser transition from $^4S_{3/2}$ level after an ESA process of $^4I_{13/2} \rightarrow {}^2H_{11/2}$ was used to suppress competitive laser transition of $^4S_{3/2} \rightarrow {}^4I_{13/2}$ at 850 nm. Then, by using the same approach with an optimized Er^{3+}:ZrF_4-based cavity, Pollnau et al. demonstrated laser emission of both 2.71 μm and 1.72 μm with a maximum output power of 158 mW at 2.71 μm and a slope efficiency of 22.6% [16]. Schneider demonstrated another approach of cascade operation at 1.55, 2.7 and 3.45 μm emissions in an Er^{3+}:ZrF_4 fiber by using GSA pumping at 650 nm [14]. Although the output power is limited to 1.2 mW at 2.7 μm due to the non-optimized mirror reflectivities, this work was the first demonstration of avoiding bottleneck of $^4I_{11/2} \rightarrow {}^4I_{13/2}$ by using the $^4I_{13/2} \rightarrow {}^4I_{15/2}$ laser transition. Then, three cascading transition at 1.7, 2.7 and 1.6 μm was demonstrated in a 3 mol.% Er^{3+}:ZrF_4 fiber with a slope efficiency of 25.4% and output power of 99 mW at 2.7 μm [17]. When considering the pump

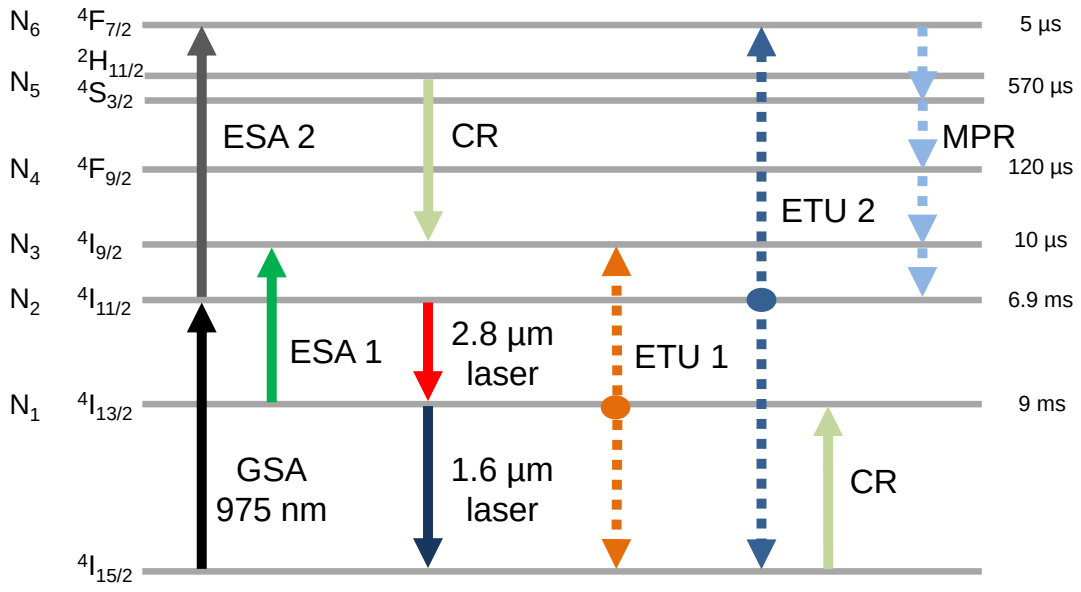

Figure I.10: Simplified energy level diagram of Er^{3+}:ZrF_4 for cascade transition at 1.6 and 2.8 μm: CR, cross-relaxation; MPR, multiphonon relaxation.

wavelength of 792 nm in this work, the slope efficiency at 2.7 μm is at 90% of the Stokes limit. All the demonstrations mentioned above are based on core-pumping approach due to the unavailability of high quality double clad fluoride fibers at that time, thus using high-power multimode diodes was not possible. In addition to that, pumping Er^{3+}-fluoride fibers at 790 nm leads to lasing at 850 nm ($^4S_{3/2} \rightarrow {}^4I_{13/2}$) due to ESA from $^4S_{3/2}$ level which saturates the 3 μm laser emission. With the advances of double-clad ZrF_4 fibers, watt-level cladding-pumped cascaded fiber lasers started to be demonstrated. Jackson developed a novel diode-pumped cascade operation at 1.61 and 2.83 μm in an Er^{3+}:ZBLAN fiber, where 4.6 W of output power at 2.83 μm with a slope efficiency of 13% with respect to the incident pump at 976 nm was achieved [34]. Another demonstration using the same approach and careful selection of Er^{3+} concentration achieved an output power of 8.2 W and a slope efficiency of 19% at 2.8 μm with respect to the absorbed pump power [41]. Recently, Li et al. reported a cascaded fiber laser based on a lightly-Er^{3+}-doped (1.5 mol.%) fluoride fiber with slope efficiencies of 26.7% and 7.1% at 2.8 μm and 1.6 μm, respectively [45]. This demonstration was the first 10-W-level 3 μm-class fiber laser with a maximum output power of 15.2 W at 2885 nm. Lastly, 2.8 and 1.6 μm cascaded laser emissions were reported from an FBG-based 1 mol.% Er^{3+}:ZrF_4 fiber cavity and a slope efficiency of 50% at 2.8 μm (exceeding the Stokes limit by 15%) with respect to absorbed pump power at 976 nm was achieved [47]. This result was interpreted by taking into account a new process ESA_1 which overlaps the 1.6 μm cascade emission and contributes to populate the $^4I_{11/2}$ level. The research work involving the demonstration of the cascade laser with a 50% slope efficiency is given in Chapter 1.

The simplified energy level diagram of Er^{3+}:ZrF_4 for cascade lasing is presented in Fig. I.10. After the excitation of ions by GSA around 975 nm, different processes namely, ESA_1, ESA_2, ETU_1, ETU_2 and MPR occur. The effect of ETU_1 on the efficiency of both laser wavelengths is lower in lightly-doped systems compared to heavily-doped ones. The simulation results show that ETU_1 contributes only to the efficiency at 2.8 μm before the emergence of the 1.6 μm transition, while ETU_2 has a much lower impact on both efficiencies [114]. The lasing threshold of both 1.6 and 2.8 μm increases with higher ETU_1 but it also reduces the populations in the $^4I_{13/2}$ level and makes a positive contribution to the slope efficiency of the 3 μm laser. Besides, ESA_2 has the same effect as in heavily-doped systems; it removes ions from the $^4I_{11/2}$ level and affects the performance of both laser transitions by lowering the slope efficiencies and increasing the threshold of the 1.6 μm transition. Nevertheless, the overall effect of ETU_2 and ESA_2 is significantly much lower than in heavily-doped systems [143] since ion-ion interaction is weaker due to the low Er^{3+} concentration. Previous numerical models have shown that 1 to 3 mol.% Er^{3+} concentration range is ideal for achieving an optimum slope efficiency and threshold levels with a low core temperature in cascaded Er^{3+}:ZrF_4 laser systems [143]. ESA_1, on the other hand, has been recently discovered within the scope of this PhD project in Er^{3+}:ZrF_4-based fibers and is centered at 1.675 μm on the $^4I_{13/2}$ to $^4I_{9/2}$ transition. It partially overlaps the cascade emission at 1.6 μm. Therefore it has a positive effect on 2.8 μm transition by enabling an additional recycling process [47]. This phenomenon is explained in Chapter 1 in detail. The rates for ETU_1, ETU_2, ESA_2, GSA, CR are the same as in equations (2), (3), (4), (5) and (6), respectively. The rate for the new ESA_1 can be defined as

$$R_{ESA_1}(z,t) = \frac{\lambda_{s_2}\Gamma_{s_2}\sigma_{ESA_1}}{hcA_{core}} N_1(z,t) \times \left[P^+_{s_2}(z,t) + P^-_{s_2}(z,t)\right] \tag{15}$$

where λ_{s_2} is located around 1.6 μm. The re-emission on the $^4I_{9/2} \rightarrow {}^4I_{13/2}$ transition is neglected since $\tau_{^4I_{9/2}} \ll \tau_{^4I_{13/2}}$. The laser transition rate for 2.8 μm is similar to Eq. (7) and it could be defined for 1.6 μm transition as

$$R_{SE_{1.6}}(z,t) = \frac{\lambda_{s_2}\Gamma_{s_2}}{hcA_{core}} \left[N_1(z,t)\sigma_{ems} - N_0(z,t)\sigma_{abs}\right] \times \left[P^+_{s_2}(z) + P^-_{s_2}(z,t)\right]] \tag{16}$$

where λ_{s_2} is the laser wavelength, Γ_{s_2} is the power filling factor, σ_{ems} and σ_{abs} are the emission and absorption cross-sections at laser wavelength, respectively, $P^+_{s_2}$ is the forward signal power, $P^-_{s_2}$ is the backward signal power.

The rate equations of the energy levels for the cascaded laser operation in Er^{3+}:ZrF_4 medium are similar to heavily-doped systems for the N_6, N_5, N_4 levels and given in Eqs. (8), (9), (10), respectively. The other rate equations including the 1.6 μm transition and ESA_1 could be defined for cascade laser operation as below.

$$\frac{dN_3(z,t)}{dt} = \sum_{i=4,5,6} \left[\beta_{i3}\tau_i^{-1}N_i(z,t)\right] + R_{ETU_1}(z,t) + R_{CR}(z,t) - \tau_3^{-1}N_3(z,t) + R_{ESA1}(z,t) \tag{17}$$

$$\frac{dN_2(z,t)}{dt} = \sum_{i=3...6} \left[\beta_{i2}\tau_i^{-1}N_i(z,t)\right] - R_{ESA_2}(z,t) - R_{SE_{2.8}}(z,t) - 2R_{ETU_2}(z,t) + R_{GSA}(z,t) - \tau_2^{-1}N_2(z,t) \tag{18}$$

$$\frac{dN_1(z,t)}{dt} = \sum_{i=2...6} \left[\beta_{i1}\tau_i^{-1}N_i(z,t)\right] + R_{SE_{2.8}}(z,t) + R_{CR}(z,t) - 2R_{ETU_1}(z,t) - R_{SE_{1.6}}(z,t) - \tau_1^{-1}N_1(z,t) - R_{ESA_1}(z,t) \tag{19}$$

$$N_{core} = \sum_{i=0,...6} N_i \tag{20}$$

Lifetime quenching by Pr^{3+}co-dopant

Co-doping of Er^{3+} with Pr^{3+} is an alternative method for 3 μm laser operation to energy recycling by ETU or cascade laser operation. In this method, the lower laser transition level $^4I_{13/2}$ of the Er^{3+} ion is depopulated through energy transfer (ET) to the Pr^{3+} co-dopant ion. Thus, the energy configuration of the medium turns into a four-level laser system. The simplified energy level diagram of Er^{3+},Pr^{3+}:ZrF_4 medium is shown in Fig. I.11. There are two main ET taking place from Er^{3+} to Pr^{3+}, namely ($^4I_{13/2}$, $^3H_4$) ET_1 ($^4I_{15/2}$, $^3F_3$) and ET_2 ($^4I_{11/2}$, $^3H_4$) $\rightarrow$ ($^4I_{15/2}$, $^1G_4$). Fortunately, ET_1 rate is higher than the detrimental ET_2 rate due to larger oscillator-strength product; thus population inversion is indeed favored for the 3 μm laser transition. Moreover, due to strong life-time quenching of the $^4I_{13/2}$-level thanks to ET_1, the rate of ground state bleaching reduces and the undesired ESA becomes negligible [135].

Efficient depletion of the $^4I_{13/2}$ level in Er^{3+},Pr^{3+}:ZrF_4 through ET was experimentally demonstrated for the first time by Schneider et al., in which an output power of 26 mW at 2.71 μm with a slope efficiency of 13.3% was achieved [13]. In another demonstration by pumping a piece of Er^{3+},Pr^{3+}:ZrF_4 fiber at 790 nm ($^4I_{9/2}$ level), 660 mW of output power at 2.7 μm with a slope efficiency of 13% was achieved [24]. Subsequently, the first watt-level 3 μm-class laser was demonstrated. In this work, 1.7 W of output power at 2.71 μm with a slope efficiency of 17.3% with respect to pump power at 790 nm was achieved from a core-pumped Er^{3+},Pr^{3+}:ZrF_4 fiber [22]. Direct pumping of the $^4I_{11/2}$ level via a 980 nm pump in a Er^{3+},Pr^{3+}:ZrF_4 double-clad fiber enabled 5.4 W of output power with a slope efficiency of 21% [29]. A tunable version of the Er^{3+},Pr^{3+}:ZrF_4 fiber laser from 2.7 to 2.8 μm at 1 W was also demonstrated by direct pumping of the $^4I_{11/2}$ level [32]. Pulsed operations based on Er^{3+},Pr^{3+}:ZrF_4 active media was also reported. Coleman et al. demonstrated a Q-switched Er^{3+},Pr^{3+}:ZrF_4 fiber laser cavity producing 250 ns pulses with a pulse energy of 19 μJ [144].

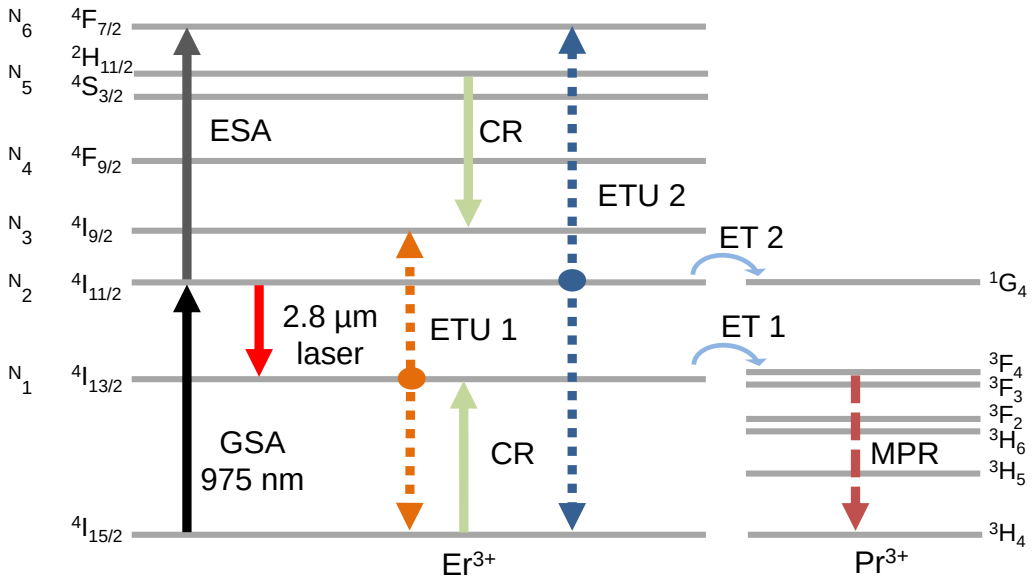

Figure I.11: Simplified energy level diagram of Er^{3+},Pr^{3+} co-doped ZrF_4 fiber: CR, cross-relaxations; MPR, multiphonon relaxation.

The rate coefficients for ET_1 and ET_2 in this regime could be defined as [135]

$$R_{ET_1}(z) = W_1 N_1 N_{Pr}(z,t) \tag{21}$$

$$R_{ET_2}(z) = W_2 N_2 N_{Pr}(z,t) \tag{22}$$

where, W_1 and W_2 are the ET coefficients for ET_1 and ET_2, respectively. The rate equations for the population densities in N_6, N_5, N_4, N_3 levels of the Er^{3+},Pr^{3+}:ZrF_4 medium could be defined similarly as in Eqs. (8), (9), (10) and (11), respectively. For N_2 and N_1 they are given by

$$\begin{aligned}\frac{dN_2(z,t)}{dt} = &\sum_{i=3\ldots6}\left[\beta_{i2}\tau_i^{-1}N_i(z,t)\right] - R_{ET_2}(z,t) - R_{SE_{2.8}}(z,t) - 2R_{ETU_2}(z,t) \\ &+ R_{GSA}(z,t) - \tau_2^{-1}N_2(z,t)\end{aligned} \tag{23}$$

$$\begin{aligned}\frac{dN_1(z,t)}{dt} = &\sum_{i=2\ldots6}\left[\beta_{i1}\tau_i^{-1}N_i(z,t)\right] + R_{SE_{2.8}}(z,t) + R_{CR}(z,t) - 2R_{ETU_1}(z,t) \\ &- \tau_1^{-1}N_1(z,t) - R_{ET_1}(z,t)\end{aligned} \tag{24}$$

$$N_{core} = \sum_{i=0,\ldots6} N_i \tag{25}$$

where, $R_{SE_{2.8}}$, R_{GSA}, R_{ETU_1}, R_{ETU_2}, R_{CR} are given by Eqs. (7), (5), (2), (3), (6), respectively.

Parameters	Value	Reference
β_{21}, β_{20}	0.37, 0.63	[141]
β_{32}, β_{31}, β_{30}	0.99, 0, 0.001	[141]
β_{43}, β_{42}, β_{41}, β_{40}	0.85, 0.006, 0.004, 0.14	[141]
β_{54}, β_{53}, β_{52}, β_{51}, β_{50}	0.34, 0.012, 0.015, 0.18, 0.44	[141]
W_{11} (SI) [m^3 s^{-1}]	3.6×10^{-23}	[145]
W_{11} (WI) [m^3 s^{-1}]	1×10^{-24}	[145]
W_{22} (SI) [m^3 s^{-1}]	1.2×10^{-23}	[145]
W_{22} (WI) [m^3 s^{-1}]	0.3×10^{-24}	[145]
W_{CR} (SI) [m^3 s^{-1}]	2.7×10^{-23}	[145]
W_{CR} (WI) [m^3 s^{-1}]	0.5×10^{-24}	[145]

Table I.1: Branching ratios and energy transfer parameters for Er^{3+} system. SI, strongly interacting condition; WI, weakly interacting condition.

I.4.2 Holmium as a gain medium

Laser emission near 3 μm from Ho^{3+}-doped fluoride fibers is realized by the $^5I_6 \rightarrow {}^5I_7$ transition and the most efficient pumping method is exciting the $^5I_6$ level by 1150 nm or the $^5I_5$ level by 890 nm pumping (Fig. I.12). Unlike for Er^{3+} ion, 3 μm transition in Ho^{3+} spans up to 3.1 μm and has a much higher gain at the water absorption peak near 2.94 μm. The peak emission wavelength of Ho^{3+}:ZrF_4 is located around 2.9 μm. On the other hand, similarly to the Er^{3+} ion, the population bottleneck problem also occurs in Ho^{3+}-doped fibers, in which the lifetime of the upper laser level ($^5I_6$) is 3.5 ms, whereas the lifetime of the lower one ($^5I_7$) is 12 ms. Therefore, similar methods as used in Er^{3+}:ZrF_4 fiber lasers are required to overcome this limitation as discussed below.

Cascade operation

The cascading approach in Ho^{3+}-doped media is similar to the one used in Er^{3+}-doped media. In Ho^{3+}-doped media, 2.1 μm laser is generated on the $^5I_7 \rightarrow {}^5I_8$ transition which contributes positively to the population inversion by depopulating the lower laser transition level of the 2.9 μm transition. Direct pumping of the $^5I_6$ level is achieved by GSA around 1150 nm. Pump diodes operating at 1150 nm are power limited but efficient and high-power generation of 1150 nm light can be obtained by Raman lasers pumped by Yb^{3+}-doped lasers. Indirect pumping of the $^5I_5$ level can also be achieved by GSA at 890 nm but leads to a lower quantum efficiency than pumping at 1150 nm. Nowadays, it is possible to find high-power industrial laser diodes operating near 890 nm in the market.

In Ho^{3+}-based systems, cascade-lasing regime was used for efficient 3 μm laser emission along with 2 μm laser emission by different research groups. Sumiyoshi et al. demonstrated simulta-

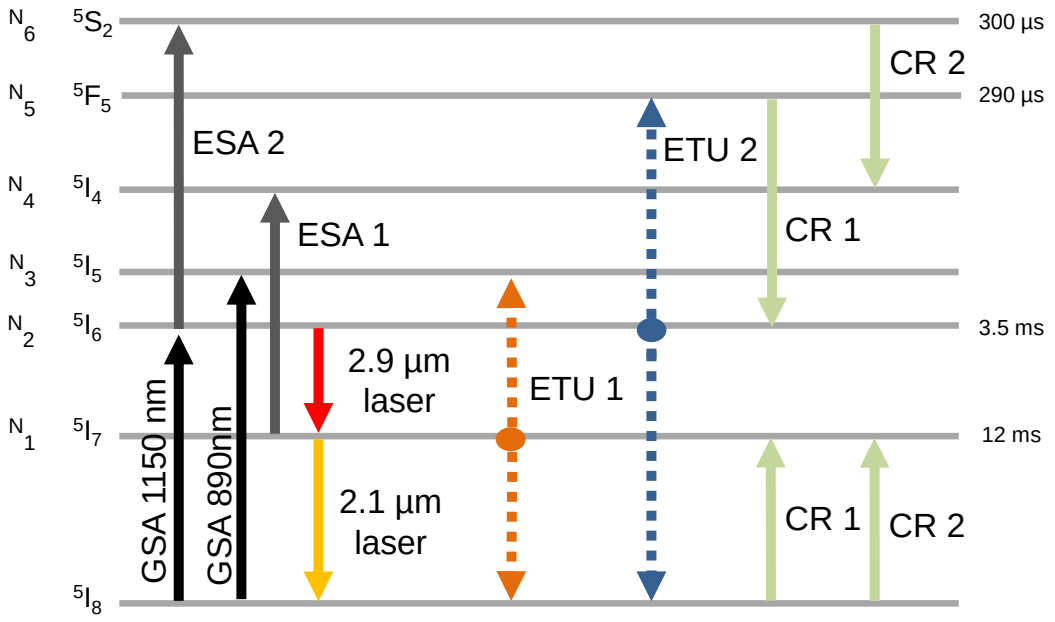

Figure I.12: Simplified energy level diagram of Ho^{3+}-doped ZrF_4 fiber. CR; cross relaxations.

neous laser emission at 2.93 and 2 μm via pumping a singly-doped Ho^{3+} fiber at 890 nm. This enabled 90 mW of output power at both wavelengths and a slope efficiency of 22% at 2.93 μm was achieved [19]. The same research group obtained 1.4 W output power at 3 μm with a slope efficiency of 30% by changing the pump wavelength to 1150 nm and optimizing the cavity [23]. Cascade operation at 3.002 μm and 2.1 μm through pumping at 1150 nm resulting in 0.77 W output power with a slope efficiency of 12.4% was also achieved [39]. This was the first fiber laser operating beyond 3 μm.

The simplified energy level diagram with cascaded transitions at 2.9 μm and 2.1 μm is shown in Fig. I.12. By pumping at 1150 nm, ESA_1 and ESA_2 processes are highly active and excite the ions to the $^5I_4$ and $^5S_2$ levels, respectively. In heavily-doped or core-pumped systems, ESA_1 and ETU_1 contribute positively to the population inversion of 3 μm laser transition by depopulating the $^5I_7$ level whereas ETU_1 is detrimental for the 2 μm transition. Moreover, in clad-pumped systems, ESA rates are much smaller than in core-pumped systems due to lower pump intensity [146]. On the other hand, ETU_2 has a detrimental effect on laser transition at 2.9 μm. Despite the contribution of ETU_1 to 3 μm laser transition, differently from Er^{3+}:ZrF_4 media, the rate of ETU_2 ($^5I_6 \rightarrow {}^5F_5$, $^5I_8$) is higher than the rate of ETU_1 ($^5I_7 \rightarrow {}^5I_5$, $^5I_8$). Hence, low-concentration of Ho^{3+} is ideal for cascade operation in Ho^{3+}-based 3 μm fiber laser. Numerical calculations show that the optimized doping concentration for cascade operation in Ho^{3+}:ZrF_4 fiber lasers is close to that of Er^{3+}:ZrF_4 fiber lasers (1-2 mol.%.). In addition, the lasing threshold for the 2 μm transition increases at higher concentration levels which reduces the overall slope efficiency [143]. However, similarly to the cascade approach in Er^{3+} fluoride

fiber lasers, cascade lasing in Ho^{3+}:ZrF_4 requires the use of longer fiber lengths due to the lower doping concentration.

The transition rates for 2.9 μm from $^5I_6$ level ($R_{SE_{2.9}}$) is similar to Eq. (7) and for 2.1 μm from $^5I_7$ is similar to Eq. (16). The ETU_1, ETU_2, ESA_1 and ESA_2 transition rates at 2.9 μm and at 2.1 μm for Ho^{3+}:ZrF_4 are also given by Eq. (2), (3), (4), (15), (7) and (16), respectively. On the other hand, the cross relaxations from $^5F_5$ and $^5S_2$ levels can be defined as

$$R_{CR_1}(z,t) = W_{CR_1} N_6(z,t) N_0(z,t) \tag{26}$$

$$R_{CR_2}(z,t) = W_{CR_2} N_5(z,t) N_0(z,t) \tag{27}$$

Energy transfer and cross relaxation parameters for weakly and strongly interaction conditions are given in Table I.2. Based on all processes in Ho^{3+}:ZrF_4, rate equations for the population densities in N_6, N_5, N_2, N_1 levels can be written as

$$\frac{dN_6(z,t)}{dt} = R_{ESA_2}(z,t) - R_{CR_2}(z,t) - \tau_6^{-1} N_6(z,t) \tag{28}$$

$$\frac{dN_5(z,t)}{dt} = R_{ETU_2}(z,t) - R_{CR_1}(z,t) + \beta_{65}\tau_6^{-1} N_6(z,t) - \tau_5^{-1} N_5(z,t) \tag{29}$$

$$\begin{aligned}\frac{dN_2(z,t)}{dt} = &\sum_{i=5,6} \left[\beta_{i2}\tau_i^{-1} N_i(z,t)\right] + R_{GSA}(z,t) + R_{CR_1}(z,t) + R_{CR_2}(z,t) \\ &- \tau_2^{-1} N_2(z,t) + R_{ETU_1}(z,t) - 2R_{ETU_2}(z,t) - R_{ESA_2}(z,t) \\ &+ R_{ESA_1}(z,t) - R_{SE_{2.9}}(z,t)\end{aligned} \tag{30}$$

$$\begin{aligned}\frac{dN_1(z,t)}{dt} = &\sum_{i=2,5,6} \left[\beta_{i2}\tau_i^{-1} N_i(z,t)\right] + R_{SE_{2.9}}(z,t) + R_{CR_1}(z,t) + R_{CR_2}(z,t) \\ &- 2R_{ETU_1}(z,t) - R_{ESA_1}(z,t) - R_{SE_{2.1}}(z,t) - \tau_1^{-1} N_1(z,t)\end{aligned} \tag{31}$$

$$N_{core} = \sum_{i=0,1,2,5,6} N_i \tag{32}$$

The branching ratios are given in Table I.2.

Lifetime quenching by Pr^{3+} co-dopant

Similarly as for Er^{3+}:ZrF_4 fiber lasers, Pr^{3+} can be used as a co-dopant in Ho^{3+}-doped fluoride fibers in order to depopulate the $^5I_7$ energy level by ET. In the Ho^{3+}, Pr^{3+}-doped systems, two energy transfer processes, ET_1 ($^5I_7$, $^3F_2$) $\rightarrow$ ($^5I_8$, $^3H_4$) and ET_2 ($^5I_6$, $^3F_4$) $\rightarrow$ ($^5I_8$, $^3H_4$) from the Ho^{3+} ion to the Pr^{3+}, take place in which the ET_1 rate is larger than the ET_2 rate. The simplified energy level of the Ho^{3+}, Pr^{3+}:ZrF_4 system is shown in Fig. I.13. The overall ET rates should be higher than both ETU_1 and ETU_2 rates to achieve an efficient deactivation of the $^5I_7$ level. Moreover ET rates depend on the concentration levels of both Ho^{3+} and Pr^{3+}

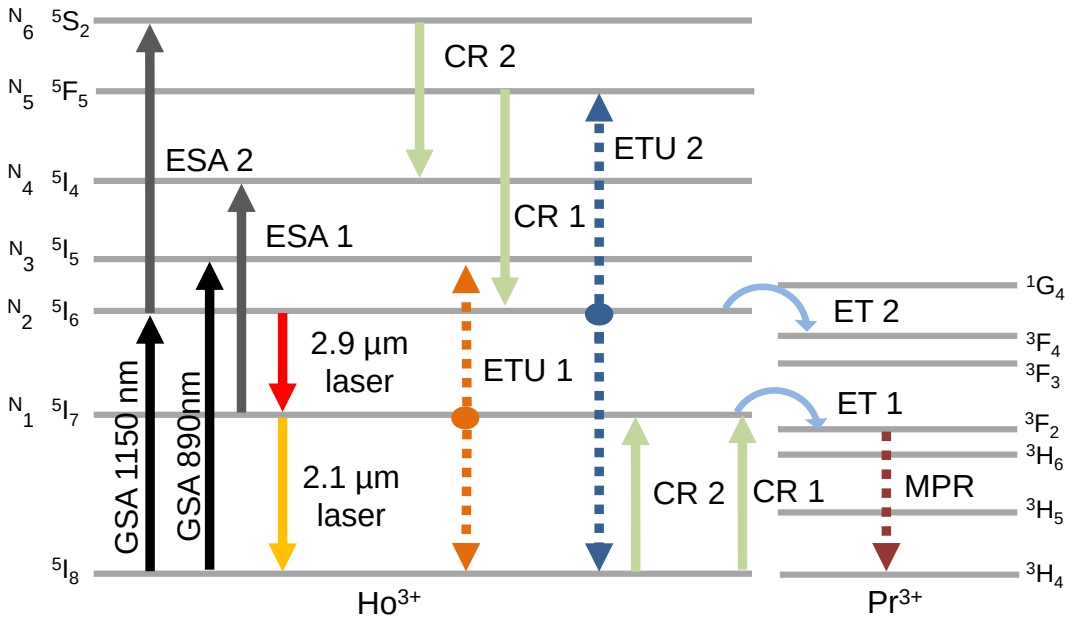

Figure I.13: Simplified energy level diagram of Ho^{3+}, Pr^{3+}-doped ZrF_4 fiber: MPR, multi phonon relaxations; CR, cross relaxations.

ions. It was demonstrated that the optimal concentration ratio for Ho^{3+}:$Pr^{3+}$is 10:1 to keep the scattering losses due to Pr^{3+} low enough and to provide an effective ET process [28].

The deactivation of the lower laser level by the Pr^{3+} co-dopant in Ho^{3+}-doped systems to achieve efficient 3 μm transition was reported in different laser architectures. The first $^5I_7$ level desensitisation in a 3 μm-class Ho^{3+}, Pr^{3+}:ZrF_4 laser was based on a core-pumped configuration using a Yb^{3+} laser at 1100 nm, in which 210 mW of output power at 2.84 μm was reported with a slope efficiency of 3.2% with respect to the absorbed pump power [25]. Jackson et al. demonstrated another core-pumped Ho^{3+}, Pr^{3+}:ZrF_4 laser delivering 2.5 W of output power at 2.86 μm with an efficiency of 29% [28]. The same amount of power with a slope efficiency of 32% from a simplified clad-pumped Ho^{3+}, Pr^{3+}:ZrF_4 laser architecture was achieved [33]. A watt-level tunable Ho^{3+}, Pr^{3+} fluoride fiber laser tunable from 2825 to 2900 nm was also demonstrated by Hudson et al., in which an output power of 1 W at a slope efficiency of 28.5% was achieved [40]. Then, Crawford et al. demonstrated a 3.4 W Ho^{3+}, Pr^{3+} fluoride fiber laser at 2.9 μm with a slope efficiency of 20.9% while pumped at 1150 nm [43]. Pulsed versions of Ho^{3+}, Pr^{3+}:ZrF_4 fiber lasers operating around 3 μm and based on Q-switched configurations were also demonstrated. Actively and tunable Q-switched configurations producing ns pulses at 2.8 μm based on a Ho^{3+}, Pr^{3+}:ZrF_4 fiber were reported [147; 148; 149]. However, in such pulsed demonstrations, pulse energies were limited to the 10 μJ-level. Therefore, a Ho^{3+}, Pr^{3+}:ZrF_4-based MOPA seeded by an OPA showed the amplification potential of Ho^{3+}:ZrF_4 by producing watt-level average output power with 124 μJ sub-ns pulses at 2.85 μm [150].

Moreover, numerical studies show that the contribution of ESA_1 and ESA_2 is negligible in cladding pumped systems. On the other hand, in core-pumped systems, ESA_1 and ESA_2 have a high impact on laser slope efficiency.

ETU_1, ETU_2, ESA_1, ESA_2, CR_1, CR_2, ET_1, ET_2 and 2.9 μm transition rates in the Ho^{3+}, Pr^{3+}:ZrF_4 system are given by Eq. (2), (3), (4), (15), (26), (27), 21), (22) and (7), respectively. The rate equations for the population densities in N_6 and N_5 are the same as in Eq. (28) and (29), respectively and N_1 and N_2 can be written as [146]

$$\begin{aligned}\frac{dN_2(z,t)}{dt} =& R_{GSA}(z,t) + \beta_{32}\tau_3^{-1}N_3(z,t) + CR_1(z,t) + CR_2(z,t) - \tau_2^{-1}N_2(z,t) \\ &+ R_{ETU_1}(z,t) - 2R_{ETU_2}(z,t) - R_{ESA_2}(z,t) + R_{ESA_1}(z,t) \\ &- R_{SE_{2.9}}(z,t) - R_{ET_2}(z,t)\end{aligned} \tag{33}$$

$$\begin{aligned}\frac{dN_1(z,t)}{dt} =& \sum_{i=2,3}\left[\beta_{i2}\tau_i^{-1}N_i(z,t)\right] + R_{SE_{2.9}}(z,t) + CR_1(z,t) + CR_2(z,t) \\ &- 2R_{ETU_1}(z,t) - R_{ESA_1}(z,t) - \tau_1^{-1}N_1(z,t) - R_{ET_1}(z,t)\end{aligned} \tag{34}$$

$$N_{core} = \sum_{i=0,1,2} N_i \tag{35}$$

Energy recycling by ESA

In addition to cascading and co-doping strategies for 3 μm emission from Ho^{3+}-media, using ESA_1 originating from $^5I_7$ level to depopulate lower laser transition level is another alternative method. The cross-section of the ESA_1 overlaps with GSA cross-section, thus, depopulation of $^5I_7$ level using pump sources at this wavelength ($\sim$ 1150 nm) can be realized.

A 340 mW output power at 2.92 μm from a 13 μm core size singly-Ho^{3+}-doped fiber with an efficiency of 5% was obtained by core-pumping at 1100 nm [27]. Another demonstration at 2.95 μm based on the same approach was shown by using a singly-doped Ho^{3+} fiber which is pumped at 1175 nm and 650 mW output power with a slope efficiency of 43 % were achieved [115].

In this approach, the efficiency of the laser transition is high in heavily-doped media since ESA_1 and ETU_1 rates are higher and core-pumping is the ideal method to enhance their rates. On the other hand, ESA_2 and ETU_2 reduce the population in $^5I_6$ level but at high concentration ESA_1 is the most dominant process which enables to achieve an efficient 3 μm transition [146]. For laser cavities based on such approach, the population densities for N_6 and N_5 levels are the same as in Eq. (28) and (29), respectively and N_1 and N_2 can be written as [146]

$$\begin{aligned}\frac{dN_2(z,t)}{dt} =& R_{GSA}(z,t) + \beta_{32}\tau_3^{-1}N_3(z,t) + R_{CR_1}(z,t) + R_{CR_2}(z,t) - \tau_2^{-1}N_2(z,t) \\ &+ R_{ETU_1}(z,t) - 2R_{ETU_2}(z,t) - R_{ESA_2}(z,t) + R_{ESA_1}(z,t) \\ &- R_{SE_{2.9}}(z,t)\end{aligned} \tag{36}$$

$$\begin{aligned}\frac{dN_1(z,t)}{dt} =& \sum_{i=2,3}\left[\beta_{i2}\tau_i^{-1}N_i(z,t)\right] + R_{SE_{2.9}}(z,t) + R_{CR_1}(z,t) + R_{CR_2}(z,t) \\ &- 2R_{ETU_1}(z,t) - R_{ESA_1}(z,t) - \tau_1^{-1}N_1(z,t)\end{aligned} \tag{37}$$

$$N_{core} = \sum_{i=0,1,2} N_i \tag{38}$$

where the ETU_1, ETU_2, ESA_1, ESA_2, CR_1, CR_2, ET_1, ET_2 and 2.9 μm transition rates for the Ho^{3+}:ZrF_4 are given by Eqs. (2), (3), (4), (15), (26), (27), (21), (22) and (7), respectively.

Parameters	Value	Reference
β_{10}	1	[143]
β_{21}, β_{20}	0.46, 0.54	[143]
β_{52}, β_{51}, β_{50}	0.9972, 0.0016, 0.0012	[143]
β_{65}, β_{62}, β_{61}, β_{60}	0.1176, 0.0529, 0.3, 0.5382	[143]
W_{11} (SI) [m^3 s^{-1}]	7×10^{-24}	[146]
W_{11} (WI) [m^3 s^{-1}]	0.53×10^{-24}	[146]
W_{22} (SI) [m^3 s^{-1}]	5×10^{-23}	[146]
W_{22} (WI) [m^3 s^{-1}]	0.42×10^{-23}	[146]
W_{CR_1} (SI) [m^3 s^{-1}]	1×10^{-23}	[146]
W_{CR_1} (WI) [m^3 s^{-1}]	0.83×10^{-24}	[146]
W_{CR_2} (WI) [m^3 s^{-1}]	2×10^{-24}	[146]
W_{CR_2} (WI) [m^3 s^{-1}]	0.17×10^{-25}	[146]

Table I.2: Branching ratios and energy transfer parameters for Ho^{3+} system. SI, strongly interacting condition; WI, weakly interacting condition.

I.4.3 Dysprosium as gain medium

The spectral range between 3 to 3.4 μm could obtained filled by using Dy^{3+} which has an emission cross section extending even this range. Laser emission around 3 μm in Dy^{3+} can be achieved on the $^6H_{13/2} \rightarrow {}^6H_{15/2}$ transition through pumping with 1.1 μm, 1.3 μm and 1.7 μm pump sources, or via 2.8 μm in-band pumping as shown in Fig. I.14. The Dy^{3+}-based laser studies are scarce compared to Er^{3+}- and Ho^{3+}-based sources. This is believed to be caused by the observation that the 3 μm laser transition by 1.1 or 1.3 μm pumping will not efficient leading to strong ESA processes, and pump sources at 1.7 μm are power limited. On the other

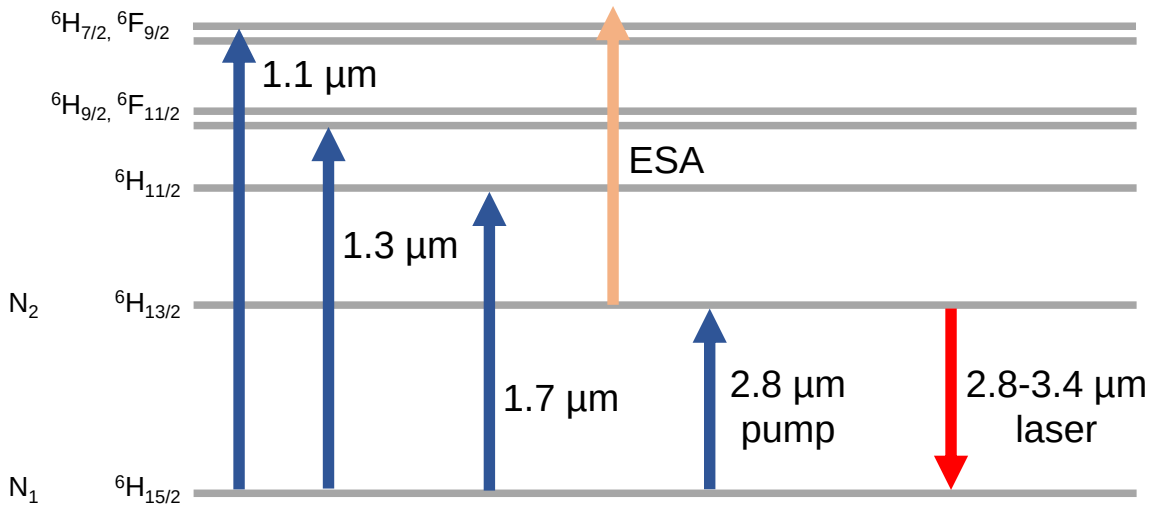

Figure I.14: Simplified energy level diagram of Dy^{3+}-doped ZrF_4 fiber.

hand, in-band pumping of Dy^{3+} enables to achieve higher efficiencies by significantly reducing the quantum defect. Recently, with the advances in 3 μm high-power monolithic lasers, highly efficient and high-power laser systems based on in-band pumping of Dy^{3+}:ZrF_4 fibers were demonstrated.

Lasing at 3 μm by Dy^{3+} ion was first demonstrated in a LaF_3 crystal pumped with a neodymium laser at 1.1 μm [151]. Twenty years after this demonstration, under the optical pumping by an Yb^{3+}-based fiber laser pump source operating at 1.1 μm, Jackson demonstrated the first Dy^{3+}-doped fluoride fiber laser operating at 2.9 μm with a CW output power of 0.275 W and a slope efficiency of 4.5% [26]. Then, a 2.96 μm quasi-continuous wave Dy^{3+}-doped fiber laser pumped by a Nd:YAG laser at 1.3 μm was demonstrated by Tsang et al. [152]. In this work, a slope efficiency of 20% with respect to the absorbed pump power was achieved. The effect of in-band pumping on the slope efficiency was experimentally confirmed by the demonstration of a Dy^{3+} fiber laser operating at 3.04 μm with a slope efficiency of 51% when pumped at 2.825 nm [46]. Then, in order to present the broad tuning properties of Dy^{3+}:ZrF_4 fibers, the first tunable operation of a Dy^{3+} fiber laser covering the 2.95 to 3.35 μm was developed with in-band pumping via 2.8 μm Er^{3+}:ZrF_4 fiber laser [153]. The same research group then demonstrated another tunable Dy^{3+} laser from 2.8 to 3.4 μm based on same approach as in [153] but using an 1.7 μm Raman pump source [70]. Recently, Fortin et al. demonstrated a monolithic 10 W Dy^{3+} fluoride fiber laser operating at 3.24 μm with a slope efficiency of 58% [51]. In this work, the laser cavity is bounded by FBGs which are written directly into the Dy^{3+} doped fiber and it is core pumped by a 2.83 μm Er^{3+}:ZrF_4 fiber laser with 20 W of output power.

The processes during in-band pumping of the Dy^{3+}:ZrF_4 system are absorption of ions to

$^6H_{13/2}$, stimulated emission ($^6H_{13/2} \rightarrow {}^6H_{15/2}$), radiative and non-radiative decays. In Dy^{3+} media, R_{GSA} and R_{SE} are given by Eq. (5) and Eq. (16), respectively; the rate equations for the in-band pumping scheme of Dy^{3+}-based media could be defined as

$$\frac{dN_1(z,t)}{dt} = R_{GSA} - R_{SE} - N_1(z,t)/\tau_1 \tag{39}$$

$$N_{core} = N_1 + N_0 \tag{40}$$

I.5 Current status of high-power 3 μm fiber laser systems

In all the operational modes, CW, pulsed or tunable, fluoride fiber lasers have shown great progress in terms of output power, pulse energy and peak power in recent years. This section presents an overview of high-power 3 μm fiber lasers with respect to their gain media and pumping schemes. The advantages and disadvantages of different laser configurations for achieving high-power operation near 3 μm will also be discussed.

I.5.1 CW operation

Depending on the laser medium, the cavity configuration for the generation of 3 μm varies. In all types of medium, approaches to overcome bottleneck problem are determined according to requirements for output power, slope efficiency, and spectral characteristics. This subsection presents the approaches to build high-power CW fluoride fiber lasers according to their gain media.

Overview of erbium as gain medium

Watt-level CW fluoride fiber lasers operating near 3 μm based on different gain media and pumping schemes demonstrated so far are listed in Table I.3. It is clearly seen that laser cavities based on energy recycling process by ETU in Er^{3+}-doped medium is the most studied approach to achieve 3 μm high-power laser emission. The first reason for that is because heavily-doped fibers enable using a short segment of fiber which makes this approach cost-effective. Second, background loss and the possibility of encountering defects and impurities in fluoride fiber are reduced by using short segment of fibers. Third, pumping directly by cost-effective high-power pump diodes operating around 975 nm is possible with the Er^{3+} ion. Lastly, by direct pumping of the upper laser transition level, it is possible to achieve a slope efficiency larger than the quantum defect limit in a heavily-doped Er^{3+} fiber laser cavity [38]. However, using heavily-doped fibers causes high thermal load along the active fiber under heavy pumping conditions. Therefore an efficient heat dissipation is required for protecting the components and for stable laser operation. All of the above 20 W fiber laser demonstrations at 3 μm are based on energy recycling by ETU approach and the highest output power (41.6 W) was achieved in the scope of this PhD project. This research work is given in Chapter 3. In this part of the project, thermal load on the Er^{3+}:ZrF_4 fiber and OH degradation were

the main limitations. Thermal load effects was mitigated by reducing the ESA rate in $^4I_{11/2}$ level through shifting the central wavelength of pump diodes near 982 nm, optimizing FBGs according to maximum temperature in the fiber core, and pumping the cavity from both ends to share pump heat load on fiber. The thermal load problems along the gain fiber with the proposed solutions are given in section I.6.

Cascade-lasing operation in Er^{3+}-doped medium based on 1.6 μm and 2.8 μm emissions, on the other hand, enables using low concentration fibers resulting in much lower heat generation along the active fiber compared to energy recycling by ETU approach. In addition, along with the new ESA found from $^4I_{13/2}$ level in the scope of this PhD project, it was shown that achieving a slope efficiency of 49.5% at 2.8 μm, which exceeds the Stokes limit by 15%, is possible via low-concentration Er^{3+}:ZrF_4 fibers in a diode-pumped laser configuration [47]. Nevertheless, these systems may require using a long segment of erbium fiber due to low-concentration; therefore, cost and background losses are expected to be high. On the other hand, at high pump power, it was observed that the temporal instabilities follow self pulsing that limits the maximum output power and causes catastrophic damage which is mentioned in Chapter 1. Today, high fluoride fiber costs complicate building fiber lasers based on cascade approach. Even though the output power achieved from the laser cavity presented in Chapter 1 is 13 W and maximum output power achieved by such approach is 15.2 W [45], the cascade approach still has a great potential for achieving record output power levels near 3 μm.

The introduction of the Pr^{3+} desensitizer into to the Er^{3+} fiber also leads to overcome bottle-neck problem by depleting the lower laser level via energy transfer to Pr^{3+} ion and enables an efficient 3 μm laser emission. The main advantage is undesired ESA and ground state bleaching is minimum compared to other approaches. In this method, the concentration of both Er^{3+} and Pr^{3+} ions should be chosen carefully to have efficient laser operation. At higher Pr^{3+} concentration, while the lower laser state is quenched faster, the ETU_1 rate is restricted. Due to lower ETU_1 rate, the theoretical slope efficiencies of co-doped media are lower than heavily-doped Er^{3+}-doped media which is also supported by simulation results [141]. The number of demonstrations and maximum achieved output power levels by lifetime quenching approach are limited. In one demonstration, an output power of 5.4 W at 2.8 μm and a slope efficiency of 21% were achieved by using 2 mol.% Er^{3+} and 0.5 mol.% Pr^{3+} co-doped fibers [29]. In this work, gain fiber was pumped through free space injection and fiber concentration was not optimized. The major advantage of this approach for high-power emission is that choosing medium doping concentration levels (2.5 to 5 mol.%) is possible. Therefore, the thermal load along the fiber during heavy pumping is expected to be lower than what is achieved through energy recycling by ETU approach and higher than the one obtained in the cascade lasing regime. By an optimized fiber with monolithic laser architecture, lifetime quenching regime can be an alternative to scale up output power of 3 μm fiber lasers in the future.

Gain medium	Wavelength (μm)	Average power (W)	Pump wavelength (nm)	Slope efficiency (%)	Approach	Year	Reference
Er^{3+}	2.8	1	970	25	ETU	1999	[21]
Ho^{3+}	3	1.4	1150	30	Cascade	1999	[23]
Er^{3+},Pr^{3+}	2.71	1.7	790	17.3	LTQ	1999	[22]
Ho^{3+}, Pr^{3+}	2.86	2.5	1100	29	LTQ	2004	[28]
Er^{3+},Pr^{3+}	2.7	5.4	975	21	LTQ	2004	[29]
Er^{3+}	2.79	10	975	21	ETU	2007	[31]
Ho^{3+}, Pr^{3+}	2.94	2.5	1150	32	LTQ	2009	[33]
Er^{3+}	2.83	4.6	976	13	Cascade	2009	[34]
Er^{3+}	2.82	5	976	32	ETU	2009	[35]
Er^{3+}	2.94	5.2	976	26.6	ETU	2009	[36]
Er^{3+}	2.82	20.6	976	35.4	ETU	2009	[38]
Er^{3+}	2.84	8.2	976	19	ETU	2011	[41]
Er^{3+}	2.82	27	976	30	ETU	2013	[42]
Ho^{3+}, Pr^{3+}	2.9	3.4	1150	20.9	LTQ	2014	[43]
Er^{3+}	2.94	30.5	975	16	ETU	2015	[44]
Er^{3+}	2.8	15.2	976	26.7	Cascade	2016	[45]
Er^{3+}	2.82	12.95	976	49.5	Cascade	2017	[47]
Er^{3+}	2.82	19.8	976	24.5	ETU	2018	[108]
Er^{3+}	2.82	41.6	980	22.9	ETU	2018	[50]
Dy^{3+}	3.24	10.1	2825	58	In-band	2019	[51]

Table I.3: Watt level CW fluoride fiber lasers operating near 3 μm. LTQ, lifetime quenching.

Overview of holmium as gain medium

The major advantage of Ho^{3+}-doped medium is that it has a higher emission cross section for laser emission beyond 2.8 μm compared to Er^{3+}. The direct excitation of $^5I_6$ upper laser level is possible under 1150 nm pumping which enables higher Stokes efficiency than Er^{3+} systems under 980 pumping. However, high-power 1150 nm pump sources are not available as industrial diodes so that complicated Yb^{3+} Raman sources are required for the direct pumping of the upper laser level. Alternatively, pump diodes operating at 890 nm allowing to pump $^5I_5$ level are commonly available.

Cascade operation in Ho^{3+}:ZrF_4 fiber systems based on laser transitions of 2.9 μm and 2.1 μm is an efficient approach since it is possible to use low-doping concentration fibers resulting in reduced heat generation as in Er^{3+}:ZrF_4-based systems. The simulation results also show that the core temperature excursion as a function of launched pump power for the Ho^{3+}:ZrF_4 medium is lower than that of Er^{3+} due to weaker MPR processes in Ho^{3+}-based media [143].

However, in such systems, there is no dominant ESA process for the recycling of the ions to the upper laser level as in Er^{3+}:ZrF_4 medium that limits the maximum achievable slope efficiency of 3 μm emission. Moreover, for the Er^{3+} cascade regime case, longer fiber length, which means higher fiber cost and background loss, is required to ensure an effective pump absorption. Therefore, demonstrations based on cascade operation in Ho^{3+} fiber is limited and maximum output power demonstration near 3 μm is 1.4 W with a slope efficiency of 30% under 1150 nm pumping [23].

Depopulation of the lower laser level by ET in Ho^{3+}, Pr^{3+}:ZrF_4 is one of the most common approaches for 3 μm fiber laser development. The rates of ESA_1 and ETU_1 originating from the lower laser level and ESA_2 and ETU_2 rates originating from the $^5I_6$ level are much lower than GSA in this configuration. Therefore, it is expected to achieve higher 3 μm laser emission rates. Moreover, it is possible to use intermediate doping concentrations which allows building cavities with shorter fiber compared to the cascade approach. In case of laser emission at longer wavelength than 2.9 μm, higher slope efficiencies than one in Er^{3+},Pr^{3+} medium is expected thanks to longer gain beyond 2.8 μm. Demonstrations by using lifetime quenching of lower level in Ho^{3+}, Pr^{3+}:ZrF_4 fiber lasers are more common than the ones in Er^{3+},Pr^{3+}:ZrF_4. In one demonstration, the maximum efficiency achieved from a 2.5 W Ho^{3+}, Pr^{3+}:ZrF_4 fiber laser operating at 2.86 μm under 1100 nm pumping is 29% which is far from the Stokes efficiency limit of 39% [28]. At that time, this laser scheme was however the most effective reported for generating 3 μm emission in a fiber laser. Later, using 1150 nm pump source, which overlaps GSA peak better than 1100 nm, 2.5 W of output power with 30 % efficiency was reported at 2.94 μm, which is the highest efficiency achieved from a fiber laser operating at water absorption peak [33].

ESA process from $^5I_7$ can help to overcome the bottleneck problem in singly-doped Ho^{3+}-based systems through energy recycling of the ions to the upper levels. However, this approach requires core pumping near 1150 nm and pump sources at such wavelength are complicated and power limited. Thus, achieving a high-power laser operation is much difficult in core-pumped fibers compared to clad-pumped configuration. The demonstration based on singly-doped Ho^{3+} systems is limited to a power below the watt-level with slope efficiencies around 5% [27].

Overview of dysprosium as gain medium

The Dy^{3+} ion provides an efficient and broader emission coverage than Er^{3+} and Ho^{3+} media beyond 3 μm. However, exciting upper energy levels for emission near 3 μm is not efficient due to strong ESA processes from these levels. The most efficient method demonstrated so far is using in-band pumping scheme which allows achieving theoretical slope efficiency of 80% at emission beyond 3 μm. However, it is necessary to use pump-sources operating around 2.8-3 μm spectral range for such a pumping scheme. A 10-W-level in-band pumping Dy^{3+} fiber laser cavity was reported with a slope efficiency of 58% in which pump source was a 2.83 μm

Er^{3+}:ZrF_4 fiber laser [51]. Therefore, it can be stated that the maximum output power from an efficient in-band Dy^{3+} system highly depends on the advances in output power of lasers operating near 2.8 μm.

I.5.2 Pulsed operation

3 μm pulsed laser operation in fluoride fibers can be achieved by using different techniques such as gain switching, Q switching, and mode locking. In addition to these, laser pulses produced from another source can be amplified through MOPA configuration for further power scaling. Each technique has advantages and disadvantages depending on the requirements for output parameters. Gain- and Q-switching are ideal techniques for producing pulses in the microsecond and the nanosecond regimes. In both approaches, the main advantage is to achieve higher average output power near 3 μm compared to other techniques. Watt-level 3 μm-class pulsed fluoride fiber laser sources demonstrated so far are listed in Table I.4. As shown in the table, Er^{3+}-doped gain medium was the most studying configuration for generating efficient pulses with μJ-level pulse energies at tens of kHz repetition rates via gain- and Q-switched laser cavities. In addition, advances in FBGs lead to build simple monolithic 10-W-level pulsed laser cavities [109]. However, in these techniques, peak power is limited due to several reasons. First, minimum obtained pulse duration through such techniques is limited to nanosecond-range. Second, the maximum laser signal peak power is limited by peak power of pump diodes, namely achieving high peak power level requires higher pump power. Hence, maximum peak power obtained from gain- or Q-switched cavity is far from the 100-kW-level. Therefore, lasers based on such techniques are not capable of being used for the applications which require high peak power.

As mentioned in section I.2, 3 μm pulsed fiber lasers have the potential to be used in medical applications for soft-tissue processing. High-precision processing is enabled by pulses with sub-ns duration, which is shorter than the average thermal relaxation timescale of water in biological tissues. Mode-locking is used to generate ultrashort pulses (fs- or ps-level) by means of various saturable absorbers and such short pulse duration allows to achieve high laser peak power. However, their average output pulse energies are in the nJ-level and their output power levels are quite limited. The maximum output so far achieved from a mode-locked oscillator is 1 W, in which the maximum pulse energy is 44 nJ [154].

High pulse energy, high output power and short pulse duration can be obtained all together by using MOPA configuration involving mode-locked oscillators or any other laser system producing short pulses as a seed laser source. A watt-level pulsed fluoride fiber laser amplifier near 3 μm was demonstrated for the first time by using a Q-switched Er^{3+}:ZrF_4 fiber laser as a seed and a piece of Er^{3+}:ZrF_4 fiber as an amplifier [140]. Although 4.2 W of output power was obtained from this system, peak power was limited to the watt-level due to pulse duration in the μs-regime. Then, by using both Er^{3+}:ZrF_4 and Ho^{3+}, Pr^{3+}:ZrF_4 as gain media and a

Gain medium	Technique	Average Power (W)	Pulse energy (μJ)	Pulse duration (ns)	Repetition rate (kHz)	Peak power (kW)	Year	Reference
Er^{3+}	Gain-switch	2	20	300	100	0.068	2011	[136]
Er^{3+}	Q-switch	12	100	90	120	0.9	2011	[137]
Er^{3+}	MOPA	4.2	59	2300	71.7	0.03	2016	[140]
Er^{3+}	Gain-switch	4.8	37	250	150	0.36	2017	[138]
Er^{3+}	Gain-switch	11.2	80	170	140	0.42	2018	[109]
Ho^{3+}, Pr^{3+}	MOPA	2.45	122	0.5	20	245	2018	[150]

Table I.4: Watt-level pulsed fluoride fiber laser sources operating near 3 μm.

picosecond OPG source at 2.8 μm, 245 kW of peak power near 3 μm was obtained from a fluoride fiber amplifier in the scope of this PhD project [150]. In this configuration, one Er^{3+} and two Ho^{3+}, Pr^{3+} fiber lengths were used as amplification stages. A seed signal of 12 mW produced by an OPG source was amplified up to an average power of 2.45 W through the three-stage amplification process. It delivers 500 ps pulses at a repetition rate of 20 kHz, and 122 μJ pulse energy, which is the highest ever produced from a 3 μm-class fiber amplifier system. The article of this research is presented in Chapter 2. In this research, it was shown that one can expect to achieve higher pulse energy levels through fiber amplifiers over the next few years. Today, active ions in fluoride fiber amplifiers are pumped via free-space optics since fluoride fiber pump combiners are not yet available. Therefore, free-space injection is necessary for both the pump and the seed into fiber that might lead to parasitic lasing processes and complex designs. Especially after the development of reliable fluoride fiber-based pump and signal combiners, ultrashort pulses produced by a mode-locked fluoride oscillator could be used as a seed source of an amplifier which enables to demonstrate compact and simple amplifiers.

I.6 Major challenges and proposed solutions

The development of high-power 3 μm-class fiber lasers is facing many challenges related to the lack of mid-infrared fiber components, which have been explained in section I.3. Some of the problems such as optical or thermal induced tip damages or gain fiber heating are similar to those encountered with silica fiber lasers. Nevertheless, there are major challenges specific to fluoride-based systems such as OH degradation affecting the performance and long-term operation of the laser systems and limiting the maximum output power. Thus, novel approaches are required to resolve these issues. In this section, major problems occurring in high-power fluoride fiber lasers and possible solutions to these problems will be discussed.

Thermal load along the gain fiber

High thermal load in active fibers and in-fiber laser cavity components is an undesired effect because it can limit the performances of the laser system by decreasing the power, leading to instabilities, or causing catastrophic failures. Especially in heavily-doped ZrF_4 fibers at high-power operation, the high thermal load can lead to fiber melting or breaking. FBGs directly written in the core of the active fiber are also be affected from heat which causes the spectral instability of laser operation due to the change in refractive index of the core and thermal expansion under heavy pumping. Besides, the fused components such as splices, fiber endcaps and fiber facets in free space pumped systems, can also be affected by heat load.

The heat in an active fiber is caused by several reasons. The quantum defect increases at longer laser wavelengths; associated with the rare-earth dopants in which pump radiation is converted into heat in the medium. The doping concentration level of the active fiber, is another factor to consider in heavily-doped fibers, where pump radiation is absorbed quickly, causing much higher heat load at the beginning of the active fiber segment. Lastly, the fiber geometry which determines the efficiency of pump absorption has also to be considered, in conjunction with the doping concentration.

The ideal pump wavelength for keeping quantum defect low is the one close to the lasing wavelength. However, in 3 μm fiber lasers, except for in-band pumping Dy^{3+} media, the pump wavelength is far from lasing wavelength compared to 1 μm silica fiber lasers. Hence alternative methods depending on the active ion can be used to increase the optical conversion efficiency. Cascade lasing is the efficient solution for managing the thermal load in gain fibers. First of all, cascade regime enables to use low doping concentration fibers since the lower lasing level is depopulated by 1.6 μm in Er^{3+}:ZrF_4 and by 2.1 μm in Ho^{3+} systems. Especially in Er^{3+}:ZrF_4 fiber lasers, along with the new ESA from 1.6 μm $^4I_{13/2} \rightarrow {}^4I_{9/2}$, it has enabled to achieve 50% efficiency and reduced heating along the fiber much more than any other configuration [47]. In heavily doped systems, ETU processes might also cause the heat load in fiber core through multiphonon relaxations from higher energy levels. ETUs are generated by ion-ion interactions, which depends on doping concentration; thus it can be reduced by decreasing the rare-earth dopant level until it is suitable enough to achieve a satisfactory ETU rate. Moreover, depending on the rare-earth ion, the central wavelength of the pump radiation might also be the part of the reason for the heat load through ESA. For instance, in Er^{3+}:ZrF_4 media, the cross-section of the ESA from the $^4I_{11/2}$ level coincides with GSA near 975 nm and it recycles the pump excitation to the upper level ($^4F_{7/2}$). Hence, it is necessary to choose a suitable pump wavelength which is a compromise between a good amount of GSA for the pump excitation and minimum ESA in such systems. Lowering the thermal distribution also depends on the geometry of the gain fiber so it is required to have an optimized fiber design depending on the rare-earth ion and the approach for achieving 3 μm transition with ideal heat dissipation. In clad-pumped fiber lasers, which enable high output power levels, the pump absorption rate is

proportional to the core-clad ratio. Thus, optimization of the core-clad ratio for effective pump absorption and output power with lower heat load is crucial in high-power fluoride fiber laser systems. The background loss at the signal and pump wavelengths might be another factor of heat generation along the fiber but today commercial ZrF_4 fibers have negligible losses at 3 μm and at pump wavelengths near 1 μm.

In heavily pumped systems, one of the most effective solutions for fiber cooling is spooling the fiber with a metallic groove cooled by water or forced air draft. After the spooling process, the contact between the fiber, in-fiber components, and metallic groove is realized by using an appropriate adhesive. Polymers generally used for such adhesive have different expansion coefficients and thermal behaviour during the laser operation; therefore choosing the proper polymer is crucial to ensure maximum contact between metallic groove and fiber. The optical quality of such polymer at both the pump and signal wavelength is also crucial. In addition, the shape of the metallic groove matching with the fiber size is another important parameter for effective cooling. In free space pumped or short-length cavities, fibers can be fixed on a simple metallic plate instead of a groove. In this approach, the contact of the fiber can be ensured by polyimide-based tapes or UV-cured polymers. Liquid cooling is another method which was already used for cooling of a 3 μm fluoride fiber laser and its components by soaking all the active fiber in a fluorocarbon liquid [37]. During the laser operation, the temperature of the active fiber and its components are monitored by using a thermal imaging camera. Since it is not possible to monitor core temperature, an estimation of core temperature according to polymer temperature and clad size is a necessary precautions to take during the laser operation. Moreover, because the pump is more absorbed at the beginning of the gain fiber, the temperature in this region is higher than in other parts; the cavity can be pumped from both ends to distribute the heat load along all the fiber.

To sum up, optimization of the fiber heating starts with a gain fiber design with optimized core-clad ratio, concentration, and geometry, as well as optimized in-fiber components. Then choosing the ideal pumping scheme, components and equipment for the cooling are the major safety measures to ensure a stable and long-term high-power laser operation.

3 μm absorption of polymer coatings

In general, fluoroacrylate polymers mostly contains H, O, C, N atoms that are known for their high degradation potential upon humidity and temperature. Optical fibers are coated with commercial ultraviolet (UV) cured low refractive index (1.34-1.4) fluoroacrylate polymers which also have a high amount of absorption around 2.9 μm based on O-H stretch, across 2.8 to 3.2 μm based on N-H stretch and between 3.3 to 3.45 based on CH-stretch. Thus, degradation of such polymers by scattered laser radiation can lead to performance losses in output laser beam or catastrophic failure of the fibers. Absorption behaviours of three different low refractive index fluoroacrylate polymer samples are shown in Fig. I.15. Polymers presented

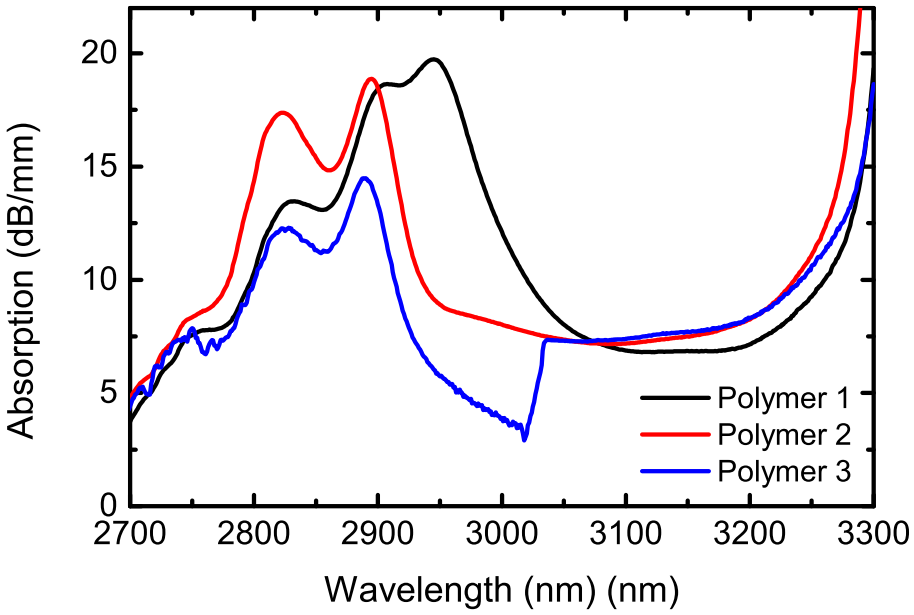

Figure I.15: Absorption of three different low refractive index fluoroacrylate polymers.

in this figure mainly serve as coating materials of the fibers used in this PhD work. They have the lowest absorption value around 3 μm compared to other polymers used during this research. As shown in the figure, absorption peaks of the polymers near 3 μm vary between 15 to 20 dB/mm; in fact, depending on polymer type, some coating polymers might have absorption rates higher than 200 dB/mm.

The laser light might scatter in different ways and be absorbed by the polymer, especially in double clad fibers. First, laser light might scatter from the splice point between two ZrF_4 fibers resulting in local hot points on the polymer used for recoating. This situation is sketched in Fig. I.16(a). Hence, especially after splice, fluoroacrylate polymers used for recoating the stripped fiber should be chosen carefully depending on their absorption at the lasing wavelength. It is also required to have a splice-junction with minimum loss. The same care should be taken for the polymer applied after writing the FBGs on stripped fibers. Second, a Fresnel reflection occurs at the air-glass interfaces of output fiber end of the cavity as sketched in Fig. I.16(b). The laser radiation around 3 μm due to Fresnel reflection from even slightly angled cleaves is directed towards polymer coating and this situation may lead to hot spots in this region. Parasitic lasing around 3 μm due to feedback from the end-face can be avoided by increasing the cleave angle of the output fiber tip. The heat due to polymer absorption is required to be minimized by thermal management with heat sink components and be monitored by a thermal camera during the laser operation.

In addition to all this, the high absorption of polymers around 3 μm can change the pumping configuration of the system. For instance, 3 μm transition is generated in an in-band pumping configuration for high efficiency in Dy^{3+}-based laser cavities by using a pump source close to

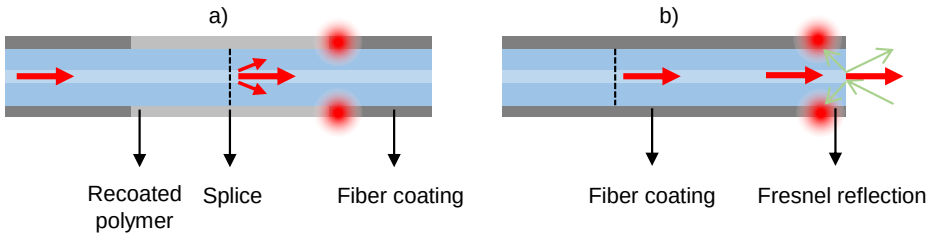

Figure I.16: Demonstration of (a) the scattering of laser from splice point and (b) Fresnel reflection at the air-glass interface.

lasing wavelength. Hence, it is necessary to use core-pumped configuration to ensure pump guiding and to avoid possible hot spots due to polymer absorption.

OH-related fiber tip degradation

Photodegradation of the fiber facet in 3 μm-class fluoride fiber lasers is one of the major problems resulting in catastrophic damage on fiber tip, especially during high-power laser emission. The degradation process is an avalanche-type effect based cumulative phenomenon of cascaded processes and power-dependent in such lasers. First, due to the highly reactive nature of the fluoride fibers with atmospheric water, the properties of the fluoride glass changes by the penetration of the water resulting ZrF_4 crystal growth and OH contaminants on the glass surface [97; 98]. Along with such natural process in ZrF_4 fibers, high-power radiation near 3 μm is absorbed by such OH contaminants which accelerates the diffusion process leading to catastrophic fiber tip damage. The representation of the OH diffusion on a fiber tip is shown in Fig. I.17(a) and a microscope image of degraded fiber tip under 3 μm high-power radiation is shown in Fig. I.17(b).

In this PhD work, even though the highest power around 3 μm from a fluoride fiber was achieved at 41.6 W, it was failed after a short time of operation (Fig. 3.6) and the long-term operation of the demonstrated cavity was limited due to such phenomenon (Chapter 3). The degradation of the fluoride fibers can be slowed down by using an ultra-pure nitrogen flux directed toward the fiber facet [150; 50]. On the other hand, endcapping of the fiber facet is the most used method to slow down the degradation process. The fabrication of the endcaps is presented in section I.3.5. Endcap components could be non oxide-based fibers such as ZrF_4, AlF_3, oxide or crystalline fibers such as SiO_2, GeO_2, Al_2O_3 etc. A research study of endcapping of high-power 3 μm class fiber lasers was realized in the scope of this PhD project and is presented in Chapter 4. In this research, a novel method based on sputtering a Si_3N_4 nanoscopic film was used for the first time to suppress OH diffusion and was validated on ZrF_4, AlF_3 and Al_2O_3 endcaps. Today, thanks to research work presented in Chapter 4, it became possible to achieve stable operation at tens of watts of output power from a protected fiber tip.

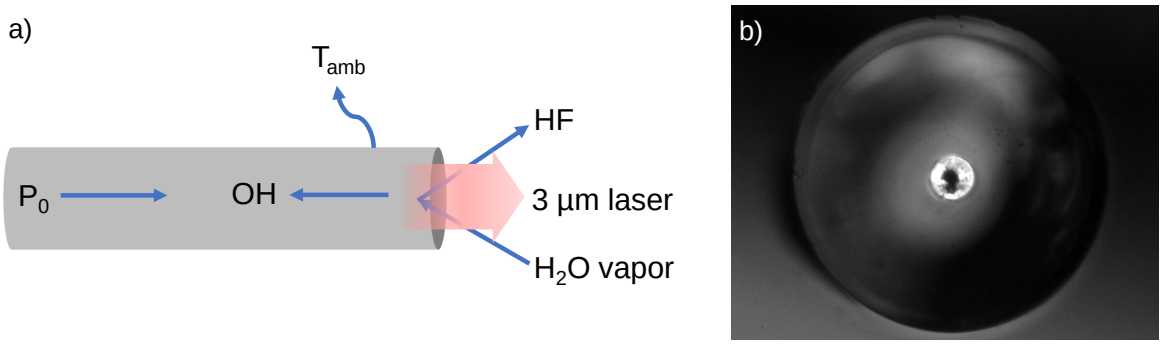

Figure I.17: (a) Schematic representation of the fiber degradation phenomenon (retrieved from [127]) and (b) microscope image of degraded fiber tip.

Laser-induced damage

One of the major challenges in all types of high-power lasers is laser-induced damage (LID) of the optical materials. LID of the optical components more often occur in the systems producing intense pulses, in which LID reduces the performance of the laser by catastrophic damages. The type of damage might be caused by thermal effects, self-focusing and nonlinear effects [155]; different kinds of origins might be responsible for the damage. In fiber lasers, they are generally observed at the output fiber facet or near such facet and it is crucial to take precaution against such damage mechanisms.

The mechanism of optical breakdown of fluoride fibers at short pulse duration is still unresolved and depends on many factors such as pulse duration, wavelength, fiber facet quality, fiber imperfections, etc. However, the major parameter to classify the damage is the peak intensity or the fluence of the laser beam. The LID damage might be as a form of microcrack on fiber facet or local deterioration. Moreover, depending on the pulse duration and the peak intensity, the damage might be based on self-focusing, absorption of heat or a cumulative effect of pulses.

LID of fluoride-fibers also greatly varies depending on the operational and physical conditions of the fiber facet. There are several demonstrations based on fluoride fiber pulsed lasers that reported stable operation with an output laser peak intensity of 100s of GW/cm^2. For instance, in femtosecond pulse regime, laser operation at GW/cm^2-level peak intensities was demonstrated by using a fluoride-based fiber amplifier. Duval et al. recently demonstrated a stable 160 fs fiber amplifier operating at 3.4 μm based on a single-mode Er:ZBLAN fiber [156]. This demonstration reported 2 W of average output power with more than 200 kW of peak power extracted from a 15 μm fiber core diameter, which corresponds to a peak intensity of more than 100 GW/cm^2. In the tens of picosecond pulse regime, Michalska et al. demonstrated a supercontinuum generation in a 6.8 μm core diameter fluoride fiber pumped by 70 ps pulses at a repetition rate of 1 kHz, where the damage threshold of the ZBLAN fiber was experimentally found to be 410 GW/cm^2 [157]. Similarly, a supercontinuum source was generated in a 9 μm core size ZBLAN fiber, by pumping with 24 ps pulses at a repetition rate of 93.6

MHz; this corresponds to more than 15 GW/cm^2 in laser peak intensity and more than 20 W of average power without failure [158]. In the hundreds of picoseconds pulse regime, a fiber amplifier demonstrated in Chapter 2 produced output pulses at more than 4 GW/cm^2 peak intensity from 85 μm core [150]. In this demonstration, there was still room for higher output power without damage but it was limited by the thermal load on fiber at pump end due to its high absorption.

Fiber facet damage threshold increases with the fiber core size. Thus, endcapping fiber tip with bigger core size fiber is major precaution which plays an important role to increase damage threshold. Gauthier et al. demonstrated supercontinuum generation in a fluoride fiber by using ps pulses, where fiber was damaged at a peak intensity of about 5 GW/cm^2 in a 15 μm core size fiber. Fiber tip damage in this work, while there is no endcapping, is seen in Fig. I.18(a). By using a proper endcap peak intensity was reduced by a factor of 60 at the fiber end. Another damage has occurred as the laser peak power became higher than the damage threshold of endcapped fiber. Damaged fiber photo through endcap is shown in Fig. I.18(b) and image taken from endcap splice interface is given in Fig. I.18(c). On the other hand, it is important to have stable pulsed operation in laser systems to avoid undesirable high-intensity pulses which might also cause catastrophic damage.

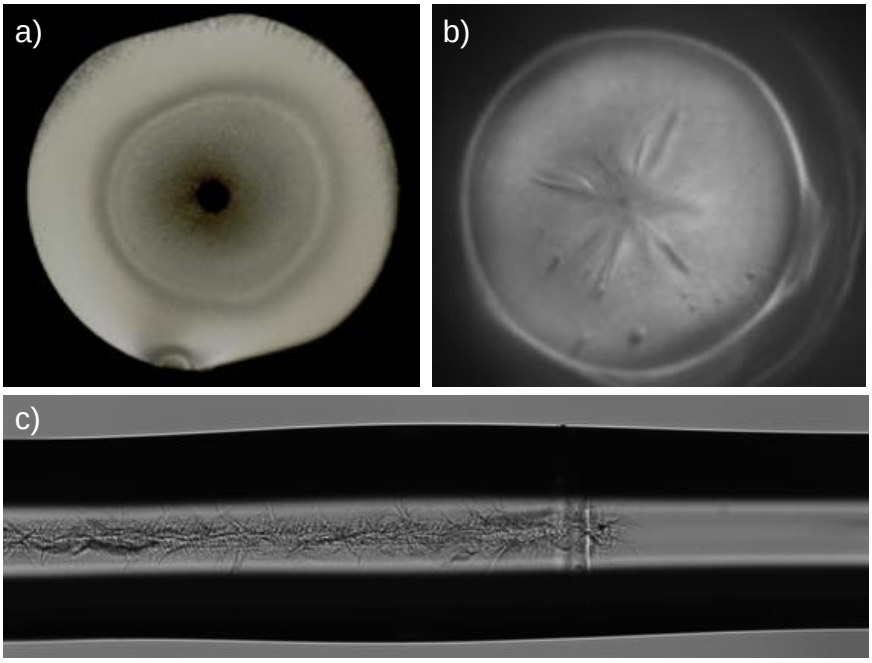

Figure I.18: Laser induced fiber tip damage images of (a) a fiber facet without endcap, (b) a fiber facet through the endcap and (c) an endcap splice interface. Images were taken during the experiments of the research work in [74].

I.7 Presentation of articles

Chapter 1 : Diode-pumped mid-infrared fiber laser with 50% slope efficiency

Publication date : 13 February 2017

Journal : Optica, Vol. 4, pp. 235-238

Authors : Y.O. Aydin, V. Fortin, F. Maes, F. Jobin, S.D. Jackson, R. Vallée, and M. Bernier

The article presented in Chapter 1 reports a cascade operation of Er^{3+}:ZrF_4-doped fiber laser pumped by 976 nm diodes, operating at 2.8 and 1.6 μm simultaneously. In the first part of the article, influence of the 1.6 μm transition on the 2.8 μm efficiency was investigated by arranging three different laser cavities with three different lengths (3, 7 and 10 m). The laser cavity is based on Er^{3+}:ZrF_4 fiber with a concentration of 1 mol.% bounded by an HR-DM as an input reflector at both wavelength, by broadband Fresnel reflection from the output endcap facet. In this part, efficiency dependency on active fiber length was studied and after reaching 1.6 μm transition threshold, an increase in slope efficiency of 2.8 μm emission was observed. On the other hand, fiber length had a positive effect on 2.8 μm efficiency by reducing its threshold.

Based on preliminary results, another laser cavity was arranged in the second part of the study. The laser in this part made of the same fiber with longer fiber length (21 m) to reduce the threshold and to increase the efficiency of 1.6 μm emission. The laser transition at 1.6 μm was realized by an HR-DM at input fiber facet and an output HR-FBG was written directly core of the Er^{3+}:ZrF_4 fiber to keep such transition as much as possible inside of the cavity. For the 2.8 μm transition, another HR-FBG was written in the core of the active fiber and Fresnel reflection was used as an output coupler for 2.8 μm transition. As in the first part, after 1.6 μm threshold is reached, the slope efficiency of 2.8 μm laser transition increased and a record slope efficiency of 49.5% with respect to the absorbed pump power was achieved.

In the last part of the research, by studying the absorption spectrum of the fiber while pumping at 976 nm, evidence of a new ESA in Er^{3+}:ZrF_4 was demonstrated. Such new ESA centered at 1.67 μm from $^4I_{13/2} \rightarrow {}^4I_{9/2}$ contributes to the efficiency of the 2.8 μm transition by leading to an additional recycling process of ions to $^4I_{11/2}$ level in Er^{3+}:ZrF_4 fiber.

Chapter 2 : High-energy picosecond pulses from a 2850 nm fiber amplifier

Publication date : 4 June 2018

Journal : Optics Letters, Vol. 43, pp. 2748-2751

Authors : Y.O. Aydin, V. Fortin, D. Kraemer, A. Fraser, R. Vallée, and M. Bernier

The article in Chapter 2 presents a Ho^{3+}, Pr^{3+} co-doped sub-nanosecond (sub-ns) fluoride

fiber amplifier operating at 2850 nm, seeded by a solid-state laser source based on optical parametric generation. A combination of solid-state laser and fiber technology was chosen given the limitations of both technologies with respect to the average power and pulse energy. In this work, 12 mW average power seed signal at a 20 kHz repetition rate was injected into a Er^{3+}:ZrF_4 fiber, which is spliced by two segments of Ho^{3+}, Pr^{3+}:ZrF_4 fiber. Firstly, the injected seed signal is amplified in an Er^{3+}:ZrF_4 fiber pumped by a 976 nm InGaAs diode; then two amplification stages were realized in two segments of Ho^{3+}, Pr^{3+}:ZrF_4 fiber by populating their ($^5I_5$) energy level with 915 nm InGaAs diodes. A controlled amplification process in Er^{3+}:ZrF_4 and Ho^{3+}, Pr^{3+}:ZrF_4 fiber was performed by controlling the spectral densities of each amplification stage.

At the end of the amplification process, pulsed signal with an average power of 2.45W, 122 μJ energy and 500 ps duration at a repetition rate of 20 kHz were achieved. In this study, the obtained pulse energy was the highest ever produced from a fluoride fiber amplifier operating around 3 μm, and the average power is a record for a sub-ns 3 μm-class fiber laser. In addition, as an alternative to common 1150 nm pumping technique, the Ho^{3+}, Pr^{3+} fiber gain is pumped at 915 nm with commercial high-power diodes for the first time.

Chapter 3 : Towards power scaling of 2.8 μm fiber lasers

Publication date : 14 September 2018

Journal : Optics Letters, Vol. 43, pp. 4542-4545

Authours : Y.O. Aydin, V. Fortin, R. Vallée, and M. Bernier

In Chapter 4, the article presents a splice-less 2824 nm Er^{3+}:ZrF_4 fiber laser cavity operating in CW regime with a record output power of 41.6 W.

A heavily doped Er^{3+}:ZrF_4 fiber (7 mol.%) was used as a gain medium. The cavity is bounded by an HR-FBG and an LR-FBG, pumped from both ends by 980 nm pump diodes. In this study, the temperature of the fiber plays a critical role for the stability of the system due to high thermal load on the heavily doped fiber; hence different precautions were taken to achieve the highest power during the experiment. Firstly, FBGs were optimized and annealed based on maximum core temperature obtained in preliminary tests. Secondly, an optimized pump diode wavelength was chosen in order to reduce ESA which has an impact on the temperature increase of the gain fiber. Lastly, the cavity was pumped from both sides instead of pumping only from the forward side in order to reduce the maximum temperature reached at the front end of the active fiber.

Such three basic optimization procedures led to achieving 41.6 W of output power at 2824 nm, which is the highest output power achieved ever from a mid-IR fluoride fiber laser cavity. At the end of the study, the potential solutions for achieving higher output power were proposed

and the long-term performance of AlF_3 and ZrF_4 endcaps was also investigated at high-power operation.

Chapter 4 : Endcapping of high-power 3 μm fiber lasers

Publication date : 22 July 2019

Journal : Optics Express, Vol. 27, pp. 20659-20669

Authors : Y.O. Aydin, F. Maes, V. Fortin, S.T. Bah, R. Vallée and M. Bernier

The article in Chapter 4 investigates the OH degradation of seven different endcap fibers manufactured from various materials under high-power 3 μm laser emission by monitoring their long-term degradation behaviours over 100 hours. In this study, different fiber endcap materials, namely non-oxide-based AlF_3, ZrF_4, oxide-based GeO_2, SiO_2 and crystalline Al_2O_3, Er:YAG were fabricated directly on output fiber tip of a 25 W 2.82 μm laser cavity similar to the system presented in Chapter 3.

We observed that, while the non-oxide based endcaps are degraded and failed during the experiments in less than 10 hours, the oxide-based fibers survived until the end of the experiment with lower degradation rates and continuously increasing temperature. In the next step of the study, sputtering an Si_3N_4 based nanoscopic film on the output facet of the oxide and non-oxide endcaps was investigated to overcome the OH diffusion problem. The experiments with Si_3N_4 coated ZrF_4, AlF_3 and Al_2O_3 fibers showed no degradation and no temperature increase during the 100 hours of experiments with 20 W average output power at 2.82 μm.

This research is the first demonstration of Si_3N_4 as an endcap coating material used in a 3 μm-class high-power fiber laser. The experiments demonstrated with 100 hours of operational time at 20 W of output power around 3 μm, which is the longest operational time without any thermal runaway for such fiber laser systems. A patent application reporting this invention was filled recently.

Chapter 1

Diode-pumped mid-infrared fiber laser with 50% slope efficiency

Y.O. Aydin[1], V. Fortin[1], F. Maes[1], F. Jobin[1], S.D. Jackson[2], R. Vallée[1], and M. Bernier[1]

[1] Centre d'optique, photonique et laser, Université Laval, Québec G1V 0A6, Canada

[2] MQ Photonics, Department of Engineering, Faculty of Science and Engineering, Macquarie University, North Ryde, NSW 2109, Australia

Published in Optica, Vol. **4**, 235-238 (2017).

1.1 Résumé

Jusqu'à présent, dans le domaine de recherche des lasers à fibre opérant dans l'infrarouge moyen, les performances ont été limitées par l'efficacité de Stokes. La conversion de photons provenant d'une diode de haute puissance fonctionnant à des longueurs d'onde de l'infrarouge proche vers une longueur d'onde dans l' infrarouge moyen entraîne nécessairement une charge thermique importante sur la fibre. Ce problème est aggravé par le fait que les verres transmettant dans l'infrarouge moyen sont thermomécaniquement plus faibles que les verres de silice, ce qui implique que la réduction de la puissance de sortie est un défi de longue date. Dans cet article, nous montrons qu'en cascadant les transitions de l'ion erbium à 2.8 et 1.6 μm dans une fibre à faible pertes en verre fluoré, l'efficacité du laser pour une émission à 2.8 μm peut atteindre 50%, dépassant ainsi la limite de Stokes de 15%. Nous montrons également qu'en utilisant une cavité fortement résonnante pour la transition de 1.6 μm, un processus d'absorption à l'état excité hautement non résonnant recycle efficacement l'excitation vers le niveau supérieur de la transition laser dans infrarouge moyen. Cette démonstration représente une avancée significative pour le domaine et ouvre la voie à de futures démonstrations qui dépasseront le niveau de puissance de 100 W.

1.2 Abstract

Until now, the field of mid-infrared fiber laser research has been constrained by the limitation imposed by the Stokes efficiency limit. The conversion of high-power diode light emission operating at near-infrared wavelengths into mid-infrared light invariably results in the deposition of significant amounts of heat in the fiber. This issue is compounded by the fact that mid-infrared transmitting glasses are thermomechanically weak, which means scaling the output power has been a longstanding challenge. In this report, we show that by cascading the adjacent transitions of the erbium ion at 2.8 and 1.6 μm in combination with a low-loss fluoride fiber, the slope efficiency for emission at 2.8 μm can reach 50%, thus exceeding the Stokes limit by 15%. We also show that by highly resonating the 1.6 μm transition, a highly non-resonant excited-state absorption process efficiently recycles the excitation back to the upper laser level of the mid-infrared transition. This demonstration represents a significant advancement for the field that paves the way for future demonstrations that will exceed the 100 W power level.

1.3 Introduction

Fiber lasers emitting in the high-energy portion of the mid-infrared (MIR) at around 3 μm have received significant attention in the past few years as a result of their potential for a vast number of applications in spectroscopy [159], biological tissue ablation [160], and infrared countermeasures [80]. Fiber lasers offer a number of important advantages over other MIR laser technologies resulting from their unmatched beam quality in addition to their compactness, long-term reliability, and great potential for power scaling [161].

The most convenient way to achieve laser emission near 3 μm is to utilize the $^4I_{11/2} \rightarrow {}^4I_{13/2}$ transition of erbium-doped fluoride glass by direct pumping of the $^4I_{11/2}$ level using 976 nm commercial InGaAs laser diodes (see Fig. 1.1). Achievement of a high slope efficiency is challenging because the quantum defect between the pump and the laser photon limits the maximum conversion efficiency to approximately 35%. In addition, the transition is potentially self-terminating because the lower state ($^4I_{13/2}$) has a longer lifetime than the upper laser level ($^4I_{11/2}$). Several strategies have been developed to reduce the potential of self-saturation of the output: for example, using heavily doped fibers to promote energy transfer upconversion (ETU 1 in Fig. 1.1, which can recycle the excitation back to the upper laser level) [38; 37; 44] or co-doping the fiber with Pr^{3+} de-sensitizer ions that resonantly transfer lower laser level excitation back to the ground state [135]. Cascade lasing at 2.8 μm ($^4I_{11/2} \rightarrow {}^4I_{13/2}$) and 1.6 μm ($^4I_{13/2} \rightarrow {}^4I_{15/2}$) [34; 45] is another promising solution to effectively depopulate the lower state of the 2.8 μm transition, with the significant advantage of reducing the heat generated by avoiding excitation to higher states and using photon emission down to the ground state.

Optical-to-optical conversion efficiencies of 3 μm-class Er^{3+}-fluoride fiber lasers have been significantly improved recently by using high-quality low-loss and heavily doped erbium fibers

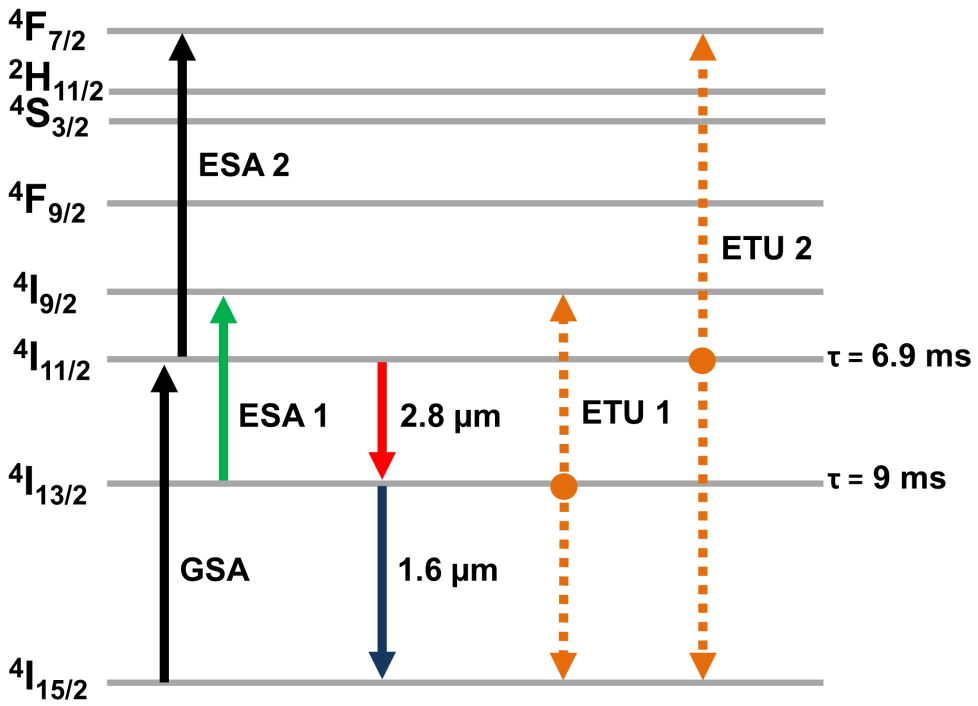

Figure 1.1: Partial energy level diagram of the relevant energy states of the erbium ions in fluoride glasses. ESA 1 corresponds to the ESA process introduced in this Letter.

to take advantage of the ETU 1 process. The first experimental evidence of pump recycling through ETU 1 was observed in a single-mode laser cavity that generated 20.6 W at a wavelength of 2.825 μm [38]; however, the slope efficiencies barely exceeded the Stokes limit and were far from reaching the predicted values of 50% for the erbium system at high doping concentrations [141]. Recently, Li et al. [10] reported a cascaded erbium-doped fiber laser based on a lightly Er^{3+}-doped (1.5 mol.%) fluoride fiber to produce efficiencies of 26.7% and 7.1% with respect to the absorbed pump powers of the 2.8 μm and 1.6 μm emissions, respectively. Overall, it has been widely understood that the slope efficiency could only be exceeded by exploiting the ETU in heavily doped fibers, which forces heat loads per unit length of the fiber that will certainly lead to problems in future power scaling attempts [37].

In this Letter, we report a highly efficient and passively cooled erbium-doped fluoride fiber laser operating at the 10 W level based on the cascade lasing scheme that sets a new slope efficiency record of 50% at the 2.8 μm emission wavelength with respect to absorbed pump power at 976 nm. The presence of an excited-state absorption (ESA) band centered at 1.675 μm between the $^4I_{13/2}$ and $^4I_{9/2}$ levels, which partially overlaps the cascaded emission at 1.614 μm, is observed and is believed to be responsible for the re- cycling of the excitation back to the upper laser level. One of the key features to result from this study is the need to highly resonate the emission from the lower transition of the cascade to maximize the efficiency at 2.8 μm.

1.4 Preliminary experiment

In the preliminary experiments, we used a simple fiber laser arrangement and different lengths of a gain fiber (3, 7, and 10 m) to study the efficiency dependence on the length of the cascaded outputs. The experimental setup of the cascade laser is shown in Fig. 1.2. The gain of the laser cavity is provided by an erbium-doped zirconium fluoride fiber from Le Verre Fluoré, France. The core had a 16.5 μm diameter, a numerical aperture (NA) of 0.12, and an erbium concentration of 1 mol.%. The propagation losses were measured to be less than 40 dB/km at 2.8 μm. The cladding had a 260 μm diameter (a circular shape with two parallel flats) and was coated with a low-index fluoroacrylate polymer to allow pump guiding with an NA of >0.46. The cladding pump absorption at 976 nm was approximately 0.3-0.35 dB/m, and the background losses were less than 0.1 dB/m at 976 nm.

The active fiber was pumped by two multimode laser diodes (IPG PLD-33) operating at approximately 976 nm, and each delivered up to 30 W in 105/125 μm, 0.12 NA silica fibers. A multi-pump combiner (ITF Technologies) with the same input fibers was used to combine the pump power into a 220/242 μm, 0.22 NA silica fiber. The input tip of the Er^{3+}-fluoride glass (Er^{3+}:FG) fiber was cleaved perpendicular to the axis of the fiber and was butt coupled to the output fiber of the combiner using a μm-resolution three-axis stage with copper V-grooves. The cleave angles of fibers were kept below 1° using an optimized cleave recipe to ensure butt coupling with a minimum air gap.

The laser cavity was made on one end of a highly reflective dichroic mirror (HR-DM) having a reflectivity of ~80% at both 1.6 and 2.8 μm and a transmission of more than 90% around 976 nm. The HR-DM was deposited on the tip of the output fiber of the combiner and consisted of a multilayer coating made of Ta_2O_5 and SiO_2, as described in [162]. At the other end of the Er^{3+}:FG fiber, a Fresnel reflection from a straight cleaved endface acted as the output coupler for both wavelengths.

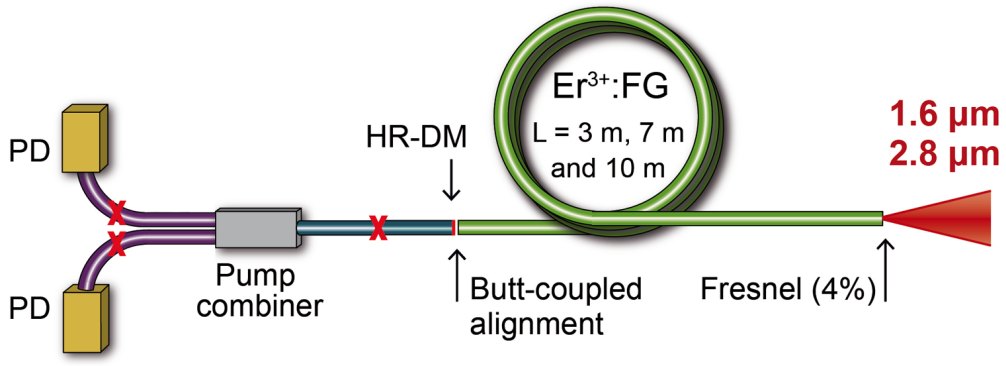

Figure 1.2: Experimental setup of the cascade laser operating at ~2.8 and ~1.6 μm that was used to test the performance against different gain fiber lengths (3, 7, and 10 m). Fresnel reflection was used for feedback. HR-DM, highly reflective dichroic mirror; PD, pump diode.

The output powers of the laser and residual pump were monitored with a thermopile detector (Gentec, UP19K-30H-H5) in combination with two different dichroic mirrors to isolate the 976 nm, 1.6 μm, and 2.8 μm power levels. Fig. 1.3 shows the measured output power of both cascaded transitions as a function of the launched and the absorbed pump power for the three different lengths of gain fiber tested.

The maximum launched pump power at 976 nm was limited to approximately 25 W for all setups. In some experiments, self-pulsing at 2.8 μm was observed in the vicinity of the 1.6 μm lasing threshold. These instabilities were most problematic for the 10 m length experiment, since they resulted in catastrophic failures along points in the fiber core as the 1.6 μm lasing threshold was reached at a high pump power. We believe this might be the result of a saturable absorption process from the ground- state Er^{3+} ions located in the unpumped end of the fiber, which results in giant Q-switched pulse formation at high pump powers [163].

We observe that the 2.8 μm slope efficiency strongly increases after the 1.6 μm transition threshold is reached (in agreement with [45]). Moreover, the threshold of the 1.6 μm transition (versus the absorbed pump power) is reduced as the fiber length is shortened, while its efficiency increases. On the other hand, the combined laser efficiency ($\eta_{\text{total}} = \eta_{1.6\mu\text{m}} + \eta_{2.8\mu\text{m}}$) slightly increases with the fiber length. The slope efficiency of 2.8 μm emission above the cascade threshold is observed, for the 10 m fiber length, to surpass the Stokes efficiency limit.

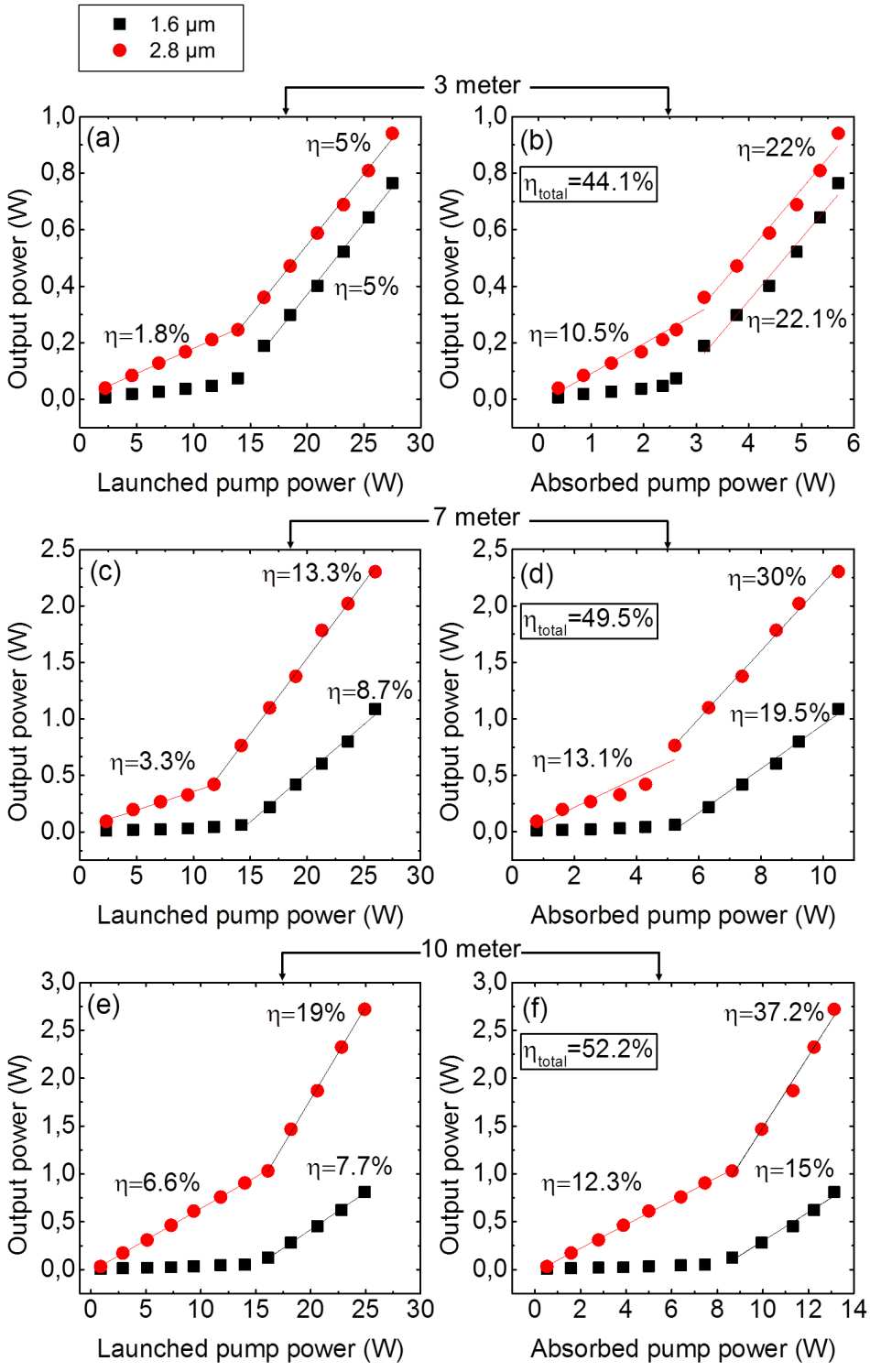

Figure 1.3: Measured output power with respect to the launched and absorbed pump powers for cavity lengths of (a), (b) 3 m, (c), (d) 7 m, and (e), (f) 10 m. The black and red dots, respectively, refer to 1.6 and 2.8 μm emissions.

1.5 Designing an optimized cavity

Based on these preliminary results, an optimized laser cavity was designed to maximize the laser efficiency for the 2.8 μm transition. For this purpose, a longer fiber has been selected to enhance the 2.8 μm efficiency at the expense of the 1.6 μm efficiency and to absorb a larger portion of the launched pump power. In addition, the total reflectivity of the cavity at 1.6 μm was raised to keep its threshold as low as possible, thus avoiding threshold-related instabilities at high pump levels. The optimized system therefore included fiber Bragg gratings (FBGs) to provide a higher and spectrally controlled feedback. The experimental setup of the optimized cascade laser is shown in Fig. 1.4.

The laser is made of a 21 m length of active fiber that was identical to the fiber used in the first experiments. The 2.8 μm cavity was bounded by a highly reflective input FBG (HR-FBG) having a maximum reflectivity of $\geq$ 99.5% centered at 2.825 μm and by the broadband Fresnel reflection from the output endcap face. As for the 1.6 μm cavity, it is composed of an HR-DM deposited on the butt-coupled silica endface with an effective reflectivity of ~80% near 1.6 μm and less than 10% near 2.8 μm, while the HR-FBG had a maximum reflectivity of $\geq$ 99.5% centered at 1.614 μm. The transmissions of the 976 nm pump through the input dichroic mirror and the HR-FBG at 2.825 μm were ~90% and ~98%, respectively. The FBGs used in this setup have respective FWHM bandwidths of 0.25 nm (HR-FBG at 1.614 μm) and 0.9 nm (HR-FBG at 2.825 μm) and were written directly in the Er^{3+}:FG fiber by a femtosecond laser at 800 nm using a phase mask, as described in [81]. The spectra of both the 1.6 and 2.8 μm signals are presented in the section 1.6. The polymer coating over the last 10 cm of the erbium fiber was removed in order to apply a UV-cured high-index acrylate polymer (n=1.54) to remove the unabsorbed residual 976 nm pump power. After the experiments were completed, the residual pump stripper was removed to measure the residual pump and to perform a cutback procedure for a precise evaluation of the absorbed pump power.

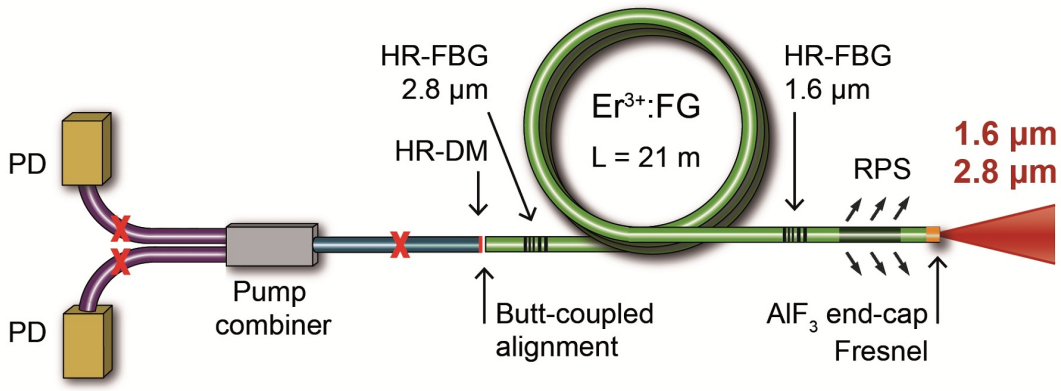

Figure 1.4: Experimental setup of the optimized cascade laser operating at 2.825 and 1.614 μm. The cavity is based on a 21 m gain fiber and includes FBGs. HR-DM, highly reflective dichroic mirror at 1.6 μm; RPS, residual pump stripper; PD, pump diode.

A short endcap (L=136 μm) is fabricated on the output tip of the Er-fluoride fiber by splicing an AlF_3-based multi-mode fluoride fiber (200/220 μm, 0.22 NA), which is then cleaved at a right angle (below 1°) to provide the broadband feedback of 0.5 to 0.75% for the 2.8 μm transition. The fusion splice was achieved with a filament-based splicer (Vytran GPX). AlF_3 endcaps are key components in high-power MIR fiber lasers to reduce the catastrophic optical damage associated with OH diffusion in the fiber tip [127]. The fiber was fixed on an aluminum plate for passive cooling. During the laser operation, the active fiber and the FBGs were also observed with a thermal imaging camera (Jenoptik IR- TCM 640) to anticipate the onset of hot spots in the laser cavity.

1.6 Results and discussion

The measured output powers with respect to absorbed pump power are shown in Fig. 1.5. The maximum launched pump power in the active fiber was 43.4 W, corresponding to 52.9 W of pump light delivered from the pump silica fiber (i.e., a ∼82% launching efficiency was achieved). As in the preliminary experiments, the slope efficiency of the 2.8 μm laser transition increases significantly when the 1.6 μm threshold is reached, from 16.6% to 49.5% with respect to absorbed pump power. The highest power achieved at 2.825 μm is 12.95 W with negligible (∼0.35 W) output power at 1.614 μm.

For most of the pump power range, the spectrum of the 2.8 μm signal was centered on the input FBG (2.825 μm). However, a secondary peak around 2.85 μm was observed for pump power levels near the maximum. This observation is consistent with the strong wavelength shift previously seen in a similar cascaded lasing scheme [45]. Moreover, we observed that the emergence of the second spectral peak triggered temporal instabilities and, in some cases, resulted in pulse formation that could lead to fiber damage at high pump powers. To avoid these problems, the Bragg wavelength of the 2.8 μm FBG will need to be increased. The optimal grating wavelength for such a cascade laser arrangement is still under investigation.

The efficiencies achieved in this study are the highest reported for a diode-pumped 3 μm fiber laser, but the mechanism underlying the performance is not fully understood. Generally, ESA and energy transfer processes play a vital role in the ion dynamics of erbium-based fluoride glass systems. In the current fiber, the concentration of Er^{3+} ions (1 mol.%) is believed to be too low for ion–ion interactions to play a major role and hence ESA, enhanced by the presence of high circulating 1.6 μm power in the core of the fiber, may lead to an additional recycling process. In an effort to isolate the mechanism, a pump/probe experiment in which a supercontinuum signal was launched in the Er^{3+}:FG fiber core with and without pumping at 976 nm was carried out (see Supplement 1). An ESA process, centered at 1.675 μm with the high energy portion overlapping the 1.614 μm emission, is identified. It originates from the $^4I_{13/2} \rightarrow {}^4I_{9/2}$ transition (ESA 1 in Fig. 1.1), which, according to previous spectroscopic

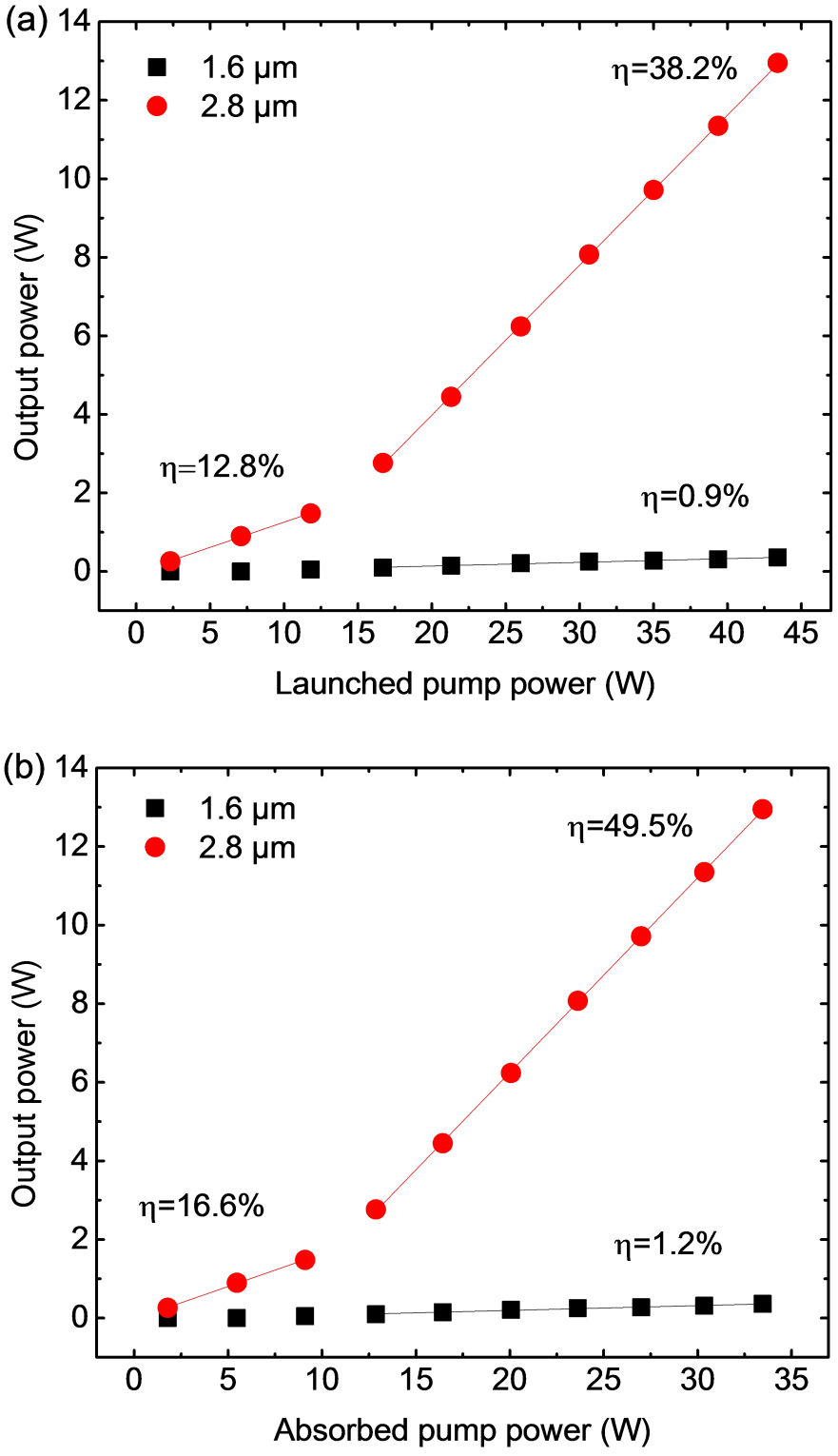

Figure 1.5: Measured output powers at 1.6 and 2.8 μm with respect to absorbed pump power for the 21 m fiber length.

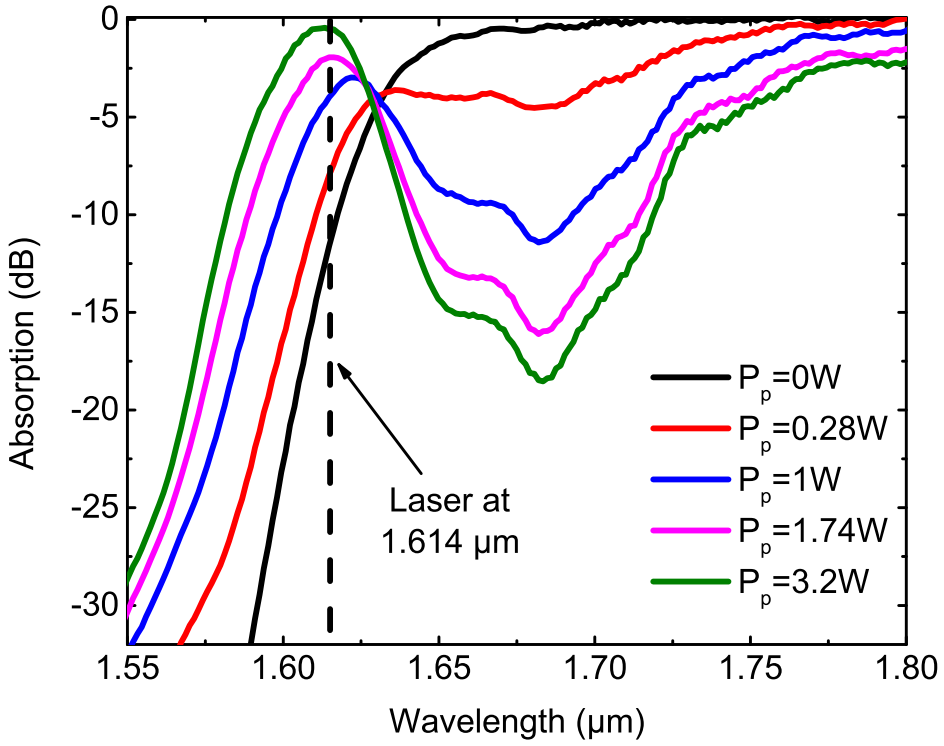

Figure 1.6: Absorption spectrum of a 90 cm length of the 1 mol.% Er^{3+}-doped fluoride fiber between 1.55 and 1.80 μm for varying launched pump powers from 0 to 3.2 W.

measurements [164], would correspond to an energy gap of 5886 cm^{-1} ($\sim$1.70 μm photon wavelength). Figure 1.6 shows the ESA spectrum centered around 1.675 μm, and part of the 1.5 μm ground-state absorption spectrum when a 90 cm length of active fiber is pumped at varying 976 nm pump powers. A maximum ESA of -18.5 dB occurs for a launched pump power of 3.2 W. While this transition has been measured in Er^{3+}:$LiYF_4$ crystals [165], to our knowledge, this is the first time it is observed in an erbium-doped glass.

The proposed process ${}^4I_{13/2} + h\nu_{1.6\mu m} \rightarrow {}^4I_{9/2}$ effectively cycles excitation back to the ${}^4I_{11/2}$ upper laser level. As a result, a longer gain fiber length increases the ESA of the 1.6 μm signal, leading to an efficiency increase at 2.8 μm.

Experimentally, the butt-coupled pump alignment could be replaced by a fusion splice [44] to obtain a monolithic laser system with enhanced efficiency and reliability. In the current experiment, the erbium fiber length was not optimized because the maximum length of a useful fluoride fiber is limited by scattering centers caused by geometrical defects and crystallization in the fabrication process [166]. Additional efficiency and output power scaling should be possible by extending the active fiber length and optimizing the 1.6 μm emission wavelength according to the ESA cross-section spectrum. The availability of longer defect-free fluoride fibers, combined with the above-mentioned improvement, could lead to output powers at 3 μm reaching the 100 W level.

1.7 Conclusion

In summary, a passively cooled cascade Er^{3+}-doped fluoride fiber laser with an output power of ∼13 W and a record slope efficiency of 50% at 2.825 μm has been reported. The influence of the 1.6 μm transition on the 2.8 μm efficiency was studied by changing the gain fiber length. The presence of the ESA process around ∼1.675 μm suggests that ESA-induced energy recycling may be responsible for significantly increasing the slope efficiency beyond the Stokes limit.

1.8 Supplementary material

This document provides supplementary information to "Diode-pumped mid-infrared fiber laser with 50% slope efficiency," https://doi.org/10.1364/optica.4.000235. We present experimental evidence for excited state absorption at 1.68 μm and discuss its effect on the slope efficiency of the 2.8 output in Er^{3+}-doped fluoride fiber cascade lasers. The output spectra of the laser signals and the transmission spectra of the fiber Bragg gratings are also presented.

1.8.1 ESA at 1.68 μm: measurement and analysis

The experimental setup shown in Fig. 1.7 was employed to measure the excited state absorption spectrum in the 1 mol.% Er^{3+}-doped fluoride fiber. In the setup, a near-infrared supercontinuum (SC) source (Koheras, SuperK) was used as a probe and a multi-mode diode at 976 nm (IPG PLD-33) was used as the pump. A longpass filter was placed in front of the SC collimator to suppress wavelengths below 1.3 μm. The probe signal was launched using a 16x aspheric lens into the 11 μm-diameter core (0.125 NA) of the silica fiber used in the central branch of a custom multi pump/signal combiner (MPC) from ITF Technologies while the pump was launched in one of the two 105/125 μm branches. The output from the MPC was the same 11/250 μm silica fiber with the probe light propagating in the core and the pump light in the cladding, which was guided by the low index polymer (NA $>$ 0.46). Using a set of metallic V-grooves and precision translation stages, the output fiber from the MPC was butt-coupled to a 90 cm long, 1 mol.% Er^{3+}-doped double-clad fluoride fiber. The last 15 cm of low-index coating of the doped fiber was stripped away, placed in a metallic V-groove and recoated with a high index UV-cured acrylate to suppress the residual unabsorbed pump light. During the experiment, the SC spectrum emitted from the end of the fiber sample was characterized by a mid-IR optical spectrum analyzer (Yokogawa, AQ6375L) whilst the launched pump power was varied from 0 to 3.2 W.

The spectrum of the emitted probe light from the core of the erbium fiber in the spectral range 1.5 to 2.1 μm is presented in Fig. 1.8. Three notable features can be observed. The feature centered at 1.5 μm corresponds to ground state absorption from the $({}^4I_{15/2} \rightarrow {}^4I_{13/2})$transition. The other two bands centered at 1.675 μm and 1.96 μm were only observed when the pump was launched and originates from excited state absorption (ESA). The 1.96 μm ESA feature is

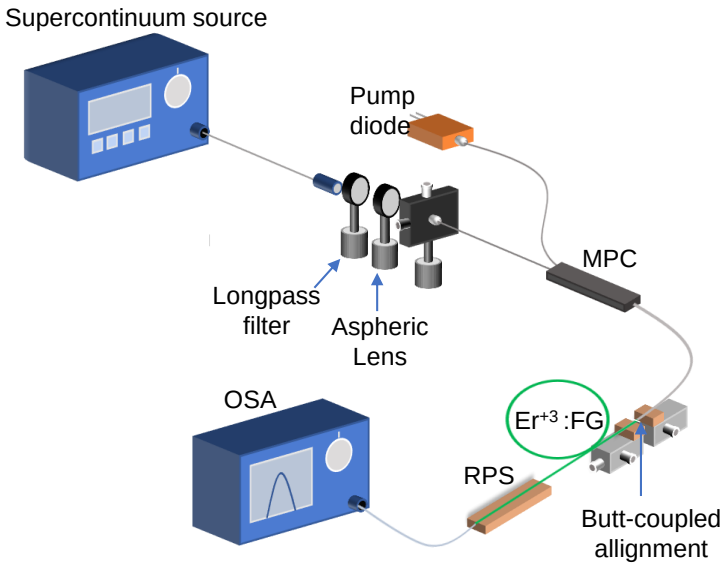

Figure 1.7: Experimental setup used for the measurement of the excited state absorption spectrum. RPS, residual pump stripper; MPC, multi-pump/signal combiner; OSA, optical spectrum analyzer.

associated with the ($^4I_{11/2} \rightarrow {}^4I_{9/2}$) transition and has been exploited for the generation of 3.5 μm laser emission from dual-wavelength pumped Er^{3+}-doped fluoride fiber lasers [167; 162] According to previous spectroscopic measurements [164], the average energy gap between of the energy levels comprising the ($^4I_{13/2} \rightarrow {}^4I_{9/2}$) transition is 5886 cm^{-1} which corresponds to the energy of a 1.70 μm photon. The ESA band located at 1.675 μm can therefore be associated with this transition.

Fluorescence from the $^4I_{13/2}$ level also contributes to the spectrum at the output from the fiber sample and impacts the measurement of the high energy part of the 1.675 μm ESA band (i.e. near the cascaded emission wavelength of 1.614 μm). This feature is seen in Fig. 1.8 by comparing the curves at $P_p = 0$ W and at $P_p = 3.2$ W, where fluorescence emission reduces the width of the ($^4I_{15/2} \rightarrow {}^4I_{13/2}$) band. Given the overlap between such fluorescence and the high energy part of the ESA band, it is clear that this ESA significantly influences the operation of the cascade laser, particularly at long fiber length when this ESA becomes strong enough to re-absorb a significant part of the laser emission.

Any photon absorbed by ESA at 1.614 μm will contribute to the slope efficiency of the transition at 2.8 μm by repopulating the $^4I_{11/2}$ upper laser level. Ions from the terminal energy state $^4I_{9/2}$ of the ESA process undergo rapid non radiative decay to the $^4I_{11/2}$ level through multiphonon relaxation (MPR). The increased slope efficiency can be understood using a simple model. Assume two 976 nm pump photons populate the $^4I_{11/2}$ level so that the $^4I_{13/2}$ level

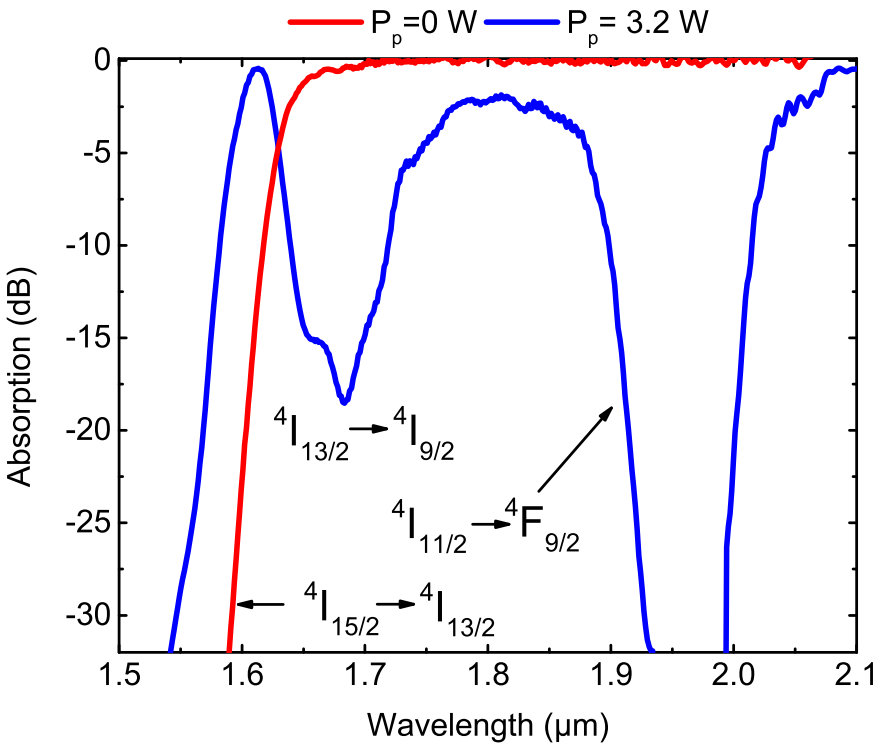

Figure 1.8: Absorption spectrum of a 90 cm length of the the 1 mol.% Er^{3+}-doped fluoride fiber between 1.5 and 2.1 μm when the 976 nm pump is turned off and on at a launched pump power of 3.2 W.

is subsequently populated from the stimulated emission of two 2.8 μm photons. One of these ions returns to the ground state by emitting a 1.615 μm photon which (assuming that all 1.614 μm photons are recycled) is absorbed by the second ion through ESA. This ion will repopulate the $^4I_{11/2}$ state after MPR from the $^4I_{9/2}$ level and will generate a third 2.8 μm photon from stimulated emission. Hence, for two 976 nm pump photons, it is possible to produce three 2.8 μm laser photons, which is equivalent to an efficiency of approximately 52%. This efficiency is in good agreement with our highest experimental slope efficiency of 49.5%. It should be noted that this analysis does not take into account the effect of energy transfers that could increase further the efficiency [141].

1.8.2 Spectra of laser signals and FBGs

Figure 1.9 shows the transmission spectrum of both FBGs along with the laser spectra. The measurements were performed using two different optical spectrum analyzers (Yokogawa, AQ6375L for 1.6 μm and AQ6376 for 2.8 μm). The 2.8 μm FBG spectrum was measured directly in transmission, probed by a custom made mid-infrared supercontinuum source. The 1.6 μm FBG spectrum had to be inferred from a reflectivity measurement since the transmission measurement was not possible at 1.6 μm due to the strong ground state absorption ($^4I_{15/2} \rightarrow {}^4I_{13/2}$) of the 21 m Er^{3+}:FG fiber. Such reflectivity measurement was performed

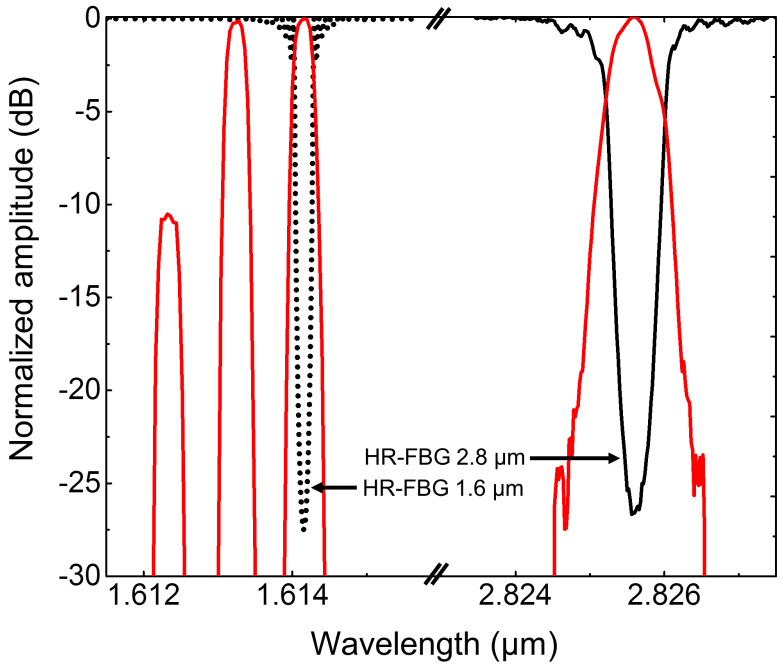

Figure 1.9: Transmission spectrum of both FBGs (black) and output emission spectrum from the cascade fiber laser (red).

using a near-infrared supercontinuum source (Koheras, SuperK) coupled to an optical fiber circulator. The single-mode fiber at the circulating branch of the circulator was butt-coupled to the multimode (at 1.6 μm) Er^{3+}:FG fiber by optimizing the coupling to probe only the fundamental mode of the fiber. By considering the measured reflectivity bandwidth of 0.25 nm and assuming a FBG with a uniform period of 538 nm over a length of 10 mm and a single-mode excitation, a numerical calculation of the transmission spectrum of the FBG was performed using Optiwave OptiGrating [168] with the result shown in Fig. 1.9 (dashed curve).

The multi-peak laser spectrum obtained from 1.612-1.614 μm is a result of the multiple transverse modes supported by the fiber at this wavelength, which are subject to slightly different effective refractive indices that see the same FBG structure.

Funding and acknowledgment

Funding: This research was supported by the Natural Sciences and Engineering Research Council of Canada (NSERC) (CG101779, CG112389); Canada Foundation for Innovation (CFI) (GF072345); Fonds de recherche du Québec - Nature et technologies (FRQNT) (CO201310, FT097991); Australian Research Council (ARC) (DP140101336).

Acknowledgment: The authors would like to thank Marc D'Auteuil and Souleymane Toubou Bah for the fabrication of the dichroic mirrors. The authors also thank David Ottaway for the initial discussions associated with excited-state absorption.

Chapter 2

High-energy picosecond pulses from a 2850 nm fiber amplifier

Y.O. Aydin[1], V. Fortin[1], D. Kraemer[2], A. Fraser[3], R. Vallée[1], and M. Bernier[1]

[1] Centre d'optique, photonique et laser, Université Laval, Québec G1V 0A6, Canada

[2] Light Matter Interaction Inc., 95 Advance Road, Toronto, Ontario M8Z 2S6, Canada

[3] Laserax Inc., 2811 Avenue Watt, Québec City, Québec G1X 4S8, Canada

Published in Optics Letters, Vol. **43**, 2748-2751 (2018).

2.1 Résumé

Nous rapportons la démonstration d'un amplificateur à fibre de verre fluoré co-dopé Ho^{3+} et Pr^{3+} pompé par une diode laser et opérant à 2850 nm avec une puissance moyenne de 2.45 W. Les impulsions produites sont d'une énergie de 122 μJ et d'une durée de 500 ps à une cadence de 20 kHz. À notre connaissance, la puissance moyenne et l'énergie des impulsions sont les plus élevées jamais démontrées par une source fibrée autour de 3 μm pour des impulsions d'une durée inférieure à la nanoseconde. L'amplificateur est alimenté optiquement par une source d'injection basée la génération paramétrique optique (OPG) et est pompé autour de 915 nm à l'aide de diodes laser InGaAs commerciales.

2.2 Abstract

We report the demonstration of a 2850 nm diode-pumped Ho^{3+}, Pr^{3+} co-doped fluoride fiber amplifier that delivers pulses with an average power of 2.45 W, 122 μJ energy and 500 ps duration at a repetition rate of 20 kHz. To the best of our knowledge, the average power and pulse energy are the highest obtained from a sub-nanosecond fiber source operating in the 3

μm spectral region. The amplifier is seeded by an optical parametric generation (OPG) source and is pumped around 915 nm using widely available InGaAs laser diodes.

2.3 Introduction

High power mid-infrared (mid-IR) laser sources operating around 3 μm have numerous applications in many fields such as spectroscopy and medicine [159; 160]. This wavelength range shows uniquely strong absorption in biomaterials due to resonance with the OH vibrational modes of water. However, in order to reduce the negative impact of thermal effects in biomaterials, the laser source must be operated in the pulsed regime, ideally with a pulse duration far shorter than both its thermal relaxation time of the material ($\sim$1 μs) and thermoelastic stress propagation time ($\sim$1 ns) [62; 169]. High-power picosecond pulsed 3 μm lasers have recently enabled advances in high-precision cutting and vaporization of biological tissues for surgery and biodiagnostics [170; 171]. Despite numerous promising applications, practical and efficient generation of high-power sub-ns mid-IR pulses remains a challenge. Er:YAG solid-state lasers operating around 2.94 μm have been studied extensively for several medical applications [172; 173]. When operated in the free-running regime, however, the pulse duration of such lasers is generally on the order of 100s of microseconds; longer than the average thermal relaxation timescale of the water in biological materials. These sources fail to minimize the thermal damage to adjacent tissues even in Q-switching configurations, where the pulse duration can be reduced to dozens of nanoseconds [173]. Furthermore, efficient amplification of sub-ns pulses to high power using Er:YAG is made impractical by the inherently low gain of short length crystals. Alternative gain materials, such as Cr:ZnS/Se, offer a potential solution, but require complicated nanosecond pump lasers, and careful management of strong thermal aberrations [174].

Fluoride glass fiber lasers emitting near 3 μm, based on either erbium- or holmium-doped fibers, have recently generated considerable interest due to their compactness, reliability and potential for power scaling. Erbium-doped fiber lasers operating on the $^4I_{11/2} \rightarrow {}^4I_{13/2}$ transition are undoubtedly the most mature technology since they have shown the highest efficiencies [47] and output powers [175] in this spectral range. Their success is in part attributable to the fact that high power pump diodes are commercially available at 975 nm. While holmium-doped fiber sources have not been studied as much, their longer peak gain wavelength (i.e. $\sim$2.85 μm instead of $\sim$2.79 μm) still makes them good candidates for medical applications as they can be operated closer to the 2.94 μm OH resonance peak. The best performances are usually achieved by co-doping the Ho^{3+} gain fiber with a deactivator ion, such as Pr^{3+}, which effectively quenches the lower state of the laser transition ($^5I_7$) and prevents a population bottleneck. While Ho^{3+}, Pr^{3+} co-doped fiber lasers are most often pumped around 1150 nm [33], this pumping scheme is not convenient since the laser diodes are less mature and power limited at this wavelength. Although Yb-doped and Raman fiber lasers can generate high power

emission around 1150 nm, such systems are much more complex and expensive compared to industrial diodes at 915 nm. As an alternative pump scheme, it is possible to pump the $^5I_5$ higher-lying level near 890 nm [176]. This absorption band is more suitable for power scaling since it can be pumped using common InGaAs industrial diodes even though they are slightly off-resonance of the $^5I_8 \rightarrow {}^5I_5$ transition at 900-915 nm. Both Er^{3+}- and Ho^{3+}-doped fiber lasers have been operated in different pulsed regimes such as Q-switching [137], gain-switching [136] and mode locking [76]. Direct amplification of pulses in doped fluoride fiber was also studied to achieve higher pulse energies. P. Wan *et al.* demonstrated 84 μJ pulse energies at a pulse duration of 24 ps around 2.8 μm from an Er:ZBLAN fiber but with a limited average power of 840 mW [139]. H. Luo demonstrated a one stage MOPA (master oscillator power amplifier) based erbium fluoride pulsed amplifier at 2.78 μm delivering maximum pulse energy of 60 μJ with pulse duration in the microsecond regime [140]. In all these demonstrations, however, their pulse energy and peak power were somehow limited compared to their solid-state laser counterparts. Thus there is a need for new solutions to generate sub-nanosecond pulses with higher energy levels.

In this Letter, we report the demonstration of a 2850 nm fiber amplifier based on a MOPA architecture. The system delivers 122 uJ, 500 ps pulses at a repetition rate 20 kHz with a peak power of 245 kW and an average power of 2.45 W. The amplifier is seeded with a picosecond optical parametric generation (OPG) source at 2.8 μm. Both Er^{3+}-doped and Ho^{3+}, Pr^{3+} co-doped fluoride glass fibers are used as gain media. As an alternative to 1150 nm pumping, the Ho^{3+}, Pr^{3+} fiber is pumped at 915 nm with commercial high-power diodes. This result sets a record for the highest pulse energy emitted from a fluoride fiber amplifier.

2.4 Experiment

The experimental setup of the MOPA laser system is shown in Fig. 2.1. The seed signal is produced by an OPG source (PIRL-VLP-2800, Light Matter Interaction Inc.) consisting of a PPLN nonlinear crystal pumped with a passively Q-switched microchip laser. It generates 875 ps pulses at a central wavelength of 2.81 μm with 25 mW of average power and a repetition rate of 20 kHz. The amplifier is made of three amplification stages based on two different doped fibers described in Table 2.1.

The first two stages rely on a co-directional (forward) pumping scheme whereas the last stage is pumped in the backward direction. The gain in the first amplification stage is provided by an 80 cm long Er^{3+}-doped zirconium fluoride (Er^{3+}:ZrF_4) double-clad fiber from *Le Verre Fluoré*. Such fiber is spliced to 50 cm of double clad Ho^{3+}, Pr^{3+} co-doped zirconium fluoride fiber (Ho^{3+}, Pr^{3+}:ZrF_4) from the same manufacturer, which is used as the second and third amplification stages. All the splices were made with a fiber splicer equipped with an iridium filament (Vytran GPX-3000) and splice losses were estimated to be less than 0.2 dB. Due to

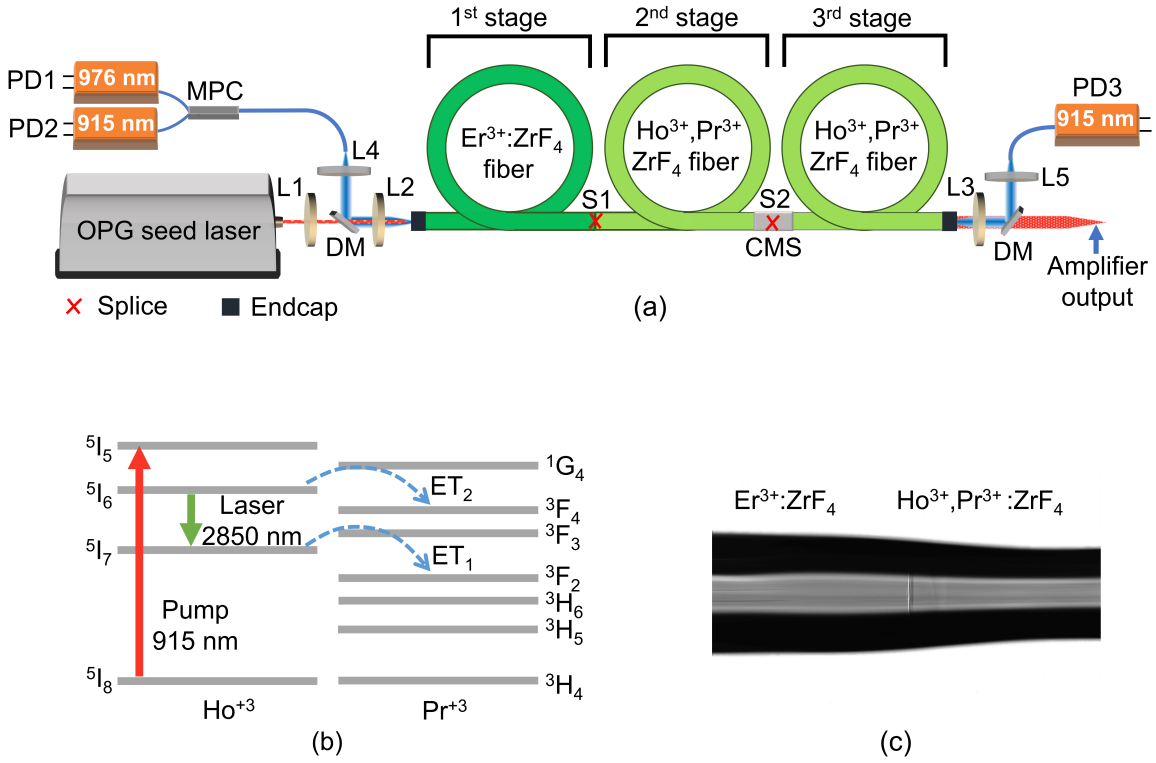

Figure 2.1: (a) Experimental setup of the laser amplifier; PD1-PD2-PD3, pump diodes; L1-L2-L3, ZnSe aspheric lenses; L4-L5, silica lenses; DM, dichroic mirror; HR at 915 and 980, HT at 2850 nm; CMS, cladding mode stripper; MPC, multi-pump combiner; S1-S2, splice points. (b) partial energy-level diagram for Ho^{3+}, Pr^{3+} doped fluoride fiber; ET_1,ET_2, energy transfer, and (c) image of the S1 splice.

the clad size difference at splice point S1 (see Fig. 2.1(c)), the filament was offset by ∼100 μm towards the Er^{3+}:ZrF_4 fiber. The splice point (S1 in Fig. 2.1) is recoated with a low index UV–cured acrylate (n=1.36) to allow pump propagation in the cladding. A high Ho^{3+} doping level (4.5 mol.%) was selected to increase the pump absorption while the Ho^{3+}/Pr^{3+} doping ratio (∼10) was chosen to maximize the 2.85 μm transition efficiency [177]. The core size was chosen large enough to reduce nonlinear effects and increase the damage threshold of the fiber. A 1 m length of the same Ho^{3+}, Pr^{3+}:ZrF_4 fiber is used as the last (third) amplifier stage. A high index UV-cured acrylate (n=1.54) is applied to the second splice point (S2 in Fig. 2.1) to eliminate the residual pump coming from the backward side. It should be noted that the splice S2 is not necessary in the system but we added it since we broke the fiber by trying to strip a polymer window inside of the Ho^{3+}, Pr^{3+}:ZrF_4 fiber segment to apply a cladding pump stripper (CPS). We therefore find easier to perform a low-loss splice between identcal fibers than stripping a polymer window along the gain fiber.

Short endcaps (L≈500 μm) were spliced on both input and output fiber tips. They were

made from an AlF_3-based multimode fluoride fiber (200/220 μm, 0.22 NA) to slow down the OH diffusion inside the fiber tip [127] and avoid damage at high power. Both endcaps were angle-cleaved at 6° to reduce the feedback in the amplifier.

The system was pumped with multiple near-infrared laser diodes. In the forward direction, a 976 nm multimode diode (30W, BWT, model K976DA3RN) and a 915 nm multimode diode (30W, BWT, model K915FA3RN) were used to pump the Er^{3+}:ZrF_4 fiber and the first segment of Ho^{3+}, Pr^{3+}:ZrF_4 fiber, respectively. The pumps were combined with a multimode pump combiner (ITF Technologies MMC03011081A) into a 220/242 μm, 0.22 NA silica fiber. In the backward direction, an additional 915 nm multimode 70W diode, (nLight, element e06) was used to backward pump the last Ho^{3+}, Pr^{3+}:ZrF_4 doped fiber segment. Silica plano-convex lenses (L4 and L5, f = 18.75 mm) were used to collimate the pump beams on both sides of the setup. The seed beam was collimated by a ZnSe aspheric lens (L1, f=50 mm) and both seed and pump beams were launched in the doped fiber through other ZnSe aspheric lenses (L2, f=12.7 mm) with respective efficiencies of 48% and 53% (including lenses and DM losses). A ZnSe lens (L3, f = 12.7 mm) was also used to collimate the output beam and for launching the 915 nm counter-propagated pump, with an efficiency of 49%. Two homemade dichroic mirrors (DM), having a high reflection at 915 and 980 nm and a high transmission at 2850 nm ($R_{980\ nm} \geq$ 99%, $R_{915\ nm} \geq$ 99% and $T_{2.85\ \mu m} \geq$90%), were placed between L3-L5 and L2-L4 lenses. The ends of both gain fibers were fixed straight in conduction cooling with UV-cured low index polymer in copper V-grooves. The rest of the fibers was fixed on an aluminum plate. A fan was also mounted above of the last 20 cm of Ho^{3+}, Pr^{3+}:ZrF_4 on the backward side (where absorbed pump is the highest) to provide forced-air cooling. In addition, a pressurized nitrogen flux was blown on the output AlF_3-based endcap to reduce ambient moisture and thus increase its optical damage threshold. The temperature of the output fiber tip, splice points and Ho^{3+}, Pr^{3+}:ZrF_4 gain fiber were monitored with a thermal imaging camera. The average power of the output signal was monitored with a thermopile detector (Gentec EO, XLP12-3S-H2). Figure 2.2 shows the output power as a function of launched pump power after each amplification stage. As shown in Fig. 2.3, the output spectrum was also characterized after each amplifier stage using a mid-IR optical spectrum analyzer (Yokogawa, AQ6376, not purged). The faded curves are the measured spectra at a resolution of 0.2 nm while the unfaded curves are averaged spectra obtained with the adjacent-average method over 1 nm.

Fiber type	**Core/Clad size (μm)**	**Core/Clad NA**	**Doping (mol.%)**
Er^{3+}:ZrF_4	16.5/260 μm	0.12/0.46	7
Ho^{3+}, Pr^{3+}:ZrF_4	85/190 μm	0.09/0.46	4.5/0.5

Table 2.1: Specification of doped fibers.

2.5 Results and discussion

In the first stage, the 12 mW average power seed signal was amplified up to a 151 mW with an efficiency of 6.5% (Fig. 2.2(a)). Besides providing preliminary amplification, the Er^{3+}:ZrF_4 fiber also served as a nonlinear medium to broaden and shift the seed spectrum up ∼2.85 μm, i.e. the gain peak of our Ho^{3+}, Pr^{3+}:ZrF_4 fiber (second amplification stage). The optimal Er^{3+}:ZrF_4 fiber length was evaluated at 80 cm to ensure a maximum overlap with the holmium gain spectrum. For a fiber exceeding this optimal length, a broad supercontinuum was generated with a significant part of its energy located beyond 3 μm [74]. The spectral density percentage between 2.8 and 2.9 μm is increased from 6.5% to 14.6% through amplification in the Er^{3+}:ZrF_4 fiber, as shown in Fig. 2.3 blue line. The signal is then amplified around 2.85 μm in the second amplification stage. The 50 cm Ho^{3+}, Pr^{3+}:ZrF_4 fiber is pumped with up to 8.9 W (at 915 nm), leading to a maximum amplified signal of 296 mW with a pulse energy of 14.8 μJ. As shown in Fig. 2.2(b), the output power efficiency with respect to launched pump power from the second amplifier stage is ∼1.55%. This can be explained by the combination of both a lower amplification efficiency in forward pumping (compared to backward pumping) and a low seeding power in the holmium gain bandwidth from the first amplifier with only 14.6% of the signal spectral density contained within 2.83 and 2.87 μm. In addition, more than 37% of the signal spectral density is contained within 2.83 and 2.87 μm at the output

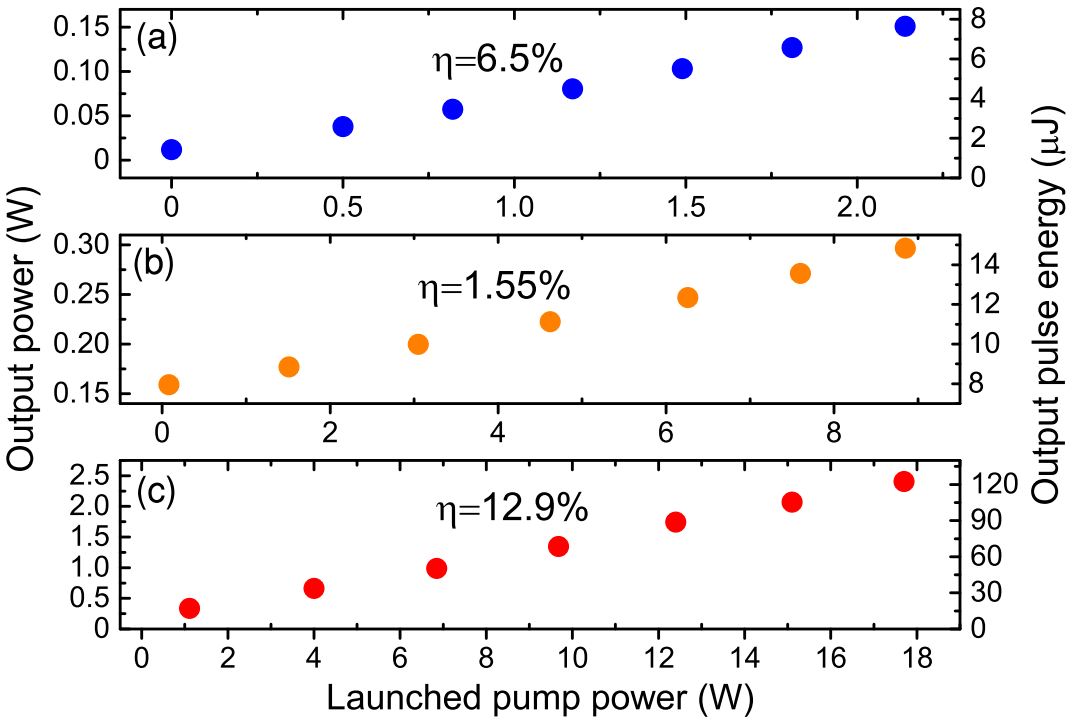

Figure 2.2: (a) Measured output power with respect to launched pump after (a) first (Er^{3+}:ZrF_4), (b) second (Ho^{3+}, Pr^{3+}:ZrF_4) and (c) third (Ho^{3+}, Pr^{3+}:ZrF_4) amplification stages.

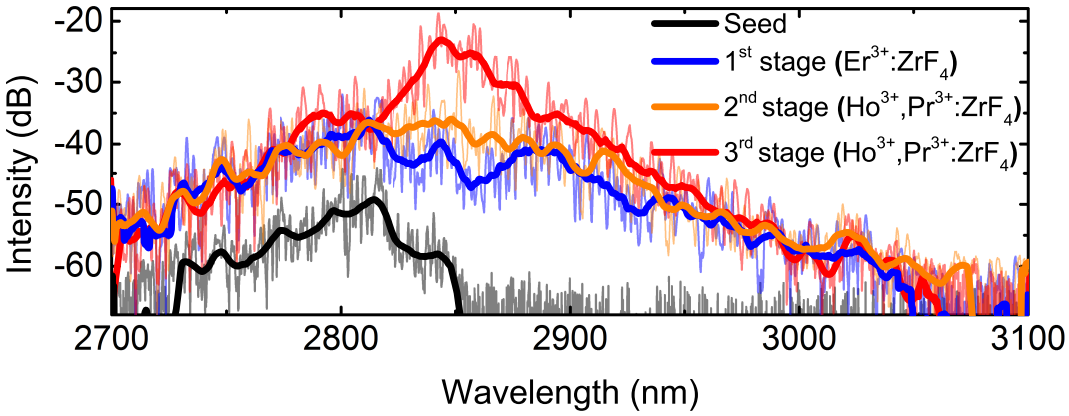

Figure 2.3: Spectrum of the seed source and evolution of the spectrum after each amplification stage.

of the 2nd amplifier stage. Finally, a last amplification stage was added to increase the gain by allowing higher pumping of the system and thus avoiding amplified spontaneous emission (ASE) to build up to a continuous laser operation in the second amplifier stage at higher forward pumping power. In the last amplification stage, the average output power and pulse energy are increased up to 2.45 W and 122 μJ respectively for a launched pump power of of 17.7 W at 915 nm. The percentage of energy between 2.83 and 2.87 μm rises to 75% and the output power slope efficiency is 12.9% (Fig. 2.2(c)). The pulse temporal profile before and and after amplification was recorded with a germanium-based photodetector (Alphalas UPD-100-IR1-P) connected to a 10 GHz oscilloscope (Agilent Infiniium DSO81004A). While the spectral range of the detector (0.4-2 μm) does not extend to the 3 μm region, it is possible to monitor the pulses through two-photon absorption as described in [178]. The temporal trace of the output signal obtained with two-photon absorption is shown in Fig. 2.4(a). FWHM

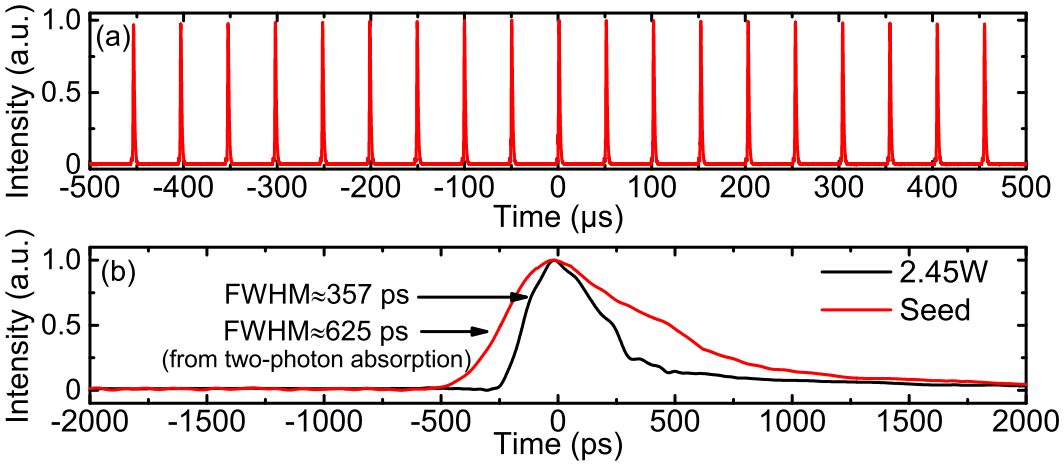

Figure 2.4: (a) Measured output pulse train and (b) pulse profiles of the seed and amplified pulses (P_{out} = 2.45 W).

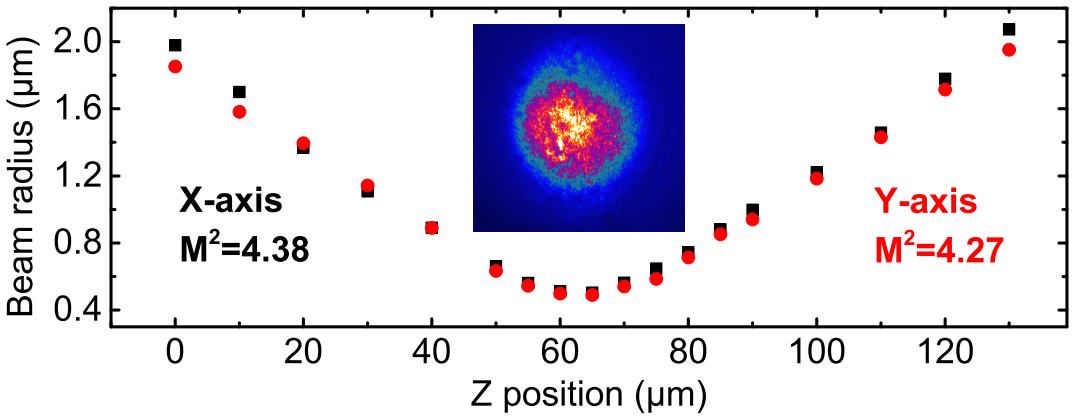

Figure 2.5: Beam quality (M^2) measurement for X and Y axes, inset; the image of the beam recorded with a InSb camera.

durations of 625 ps and 357 ps were measured respectively for the seed and amplified pulses (Fig. 2.4(b)). Assuming a Gaussian pulse shape, the actual pulse duration is thus evaluated at 875 ps for the seed and 501 ps after amplification, corresponding to a maximum output peak power of 245 kW at a 2.45 W of average output power. The output laser beam quality was characterized with a beam profile analyzer (Ophir Photonics, NanoModeScan M^2 Measuring System). The collimated beam was focused by a CaF_2 lens (f = 200 mm) along the optical axis of the instrument. Figure 2.5 shows the beam radius as a function of Z position. From this measurement we extracted an M^2 value around 4.4 and 4.3 for X and Y axis, respectively. The value is close to the theoretical M^2 value of 4.2, derived from the fiber geometry (NA and core diameter) and output wavelength. In addition, the output beam was sent to a flat aluminum surface and its shape was recorded using an InSb IR camera (Telops, TS-IR Series), as shown in the inset of Fig. 2.5. Finally, we monitored the output power stability near 1.5 W over a 1 h period as shown in Fig. 2.6. Root-mean-square (RMS) fluctuations of about 0.4% (0.7% peak to peak) were obtained. While the amplifier was stable at this power level, we noticed that the AlF_3 endcap and surrounding polymer started to deteriorate when the power was further increased. This degradation eventually led to power instabilities and fiber tip failure. By monitoring the temperature during the experiments, we observed that the combination

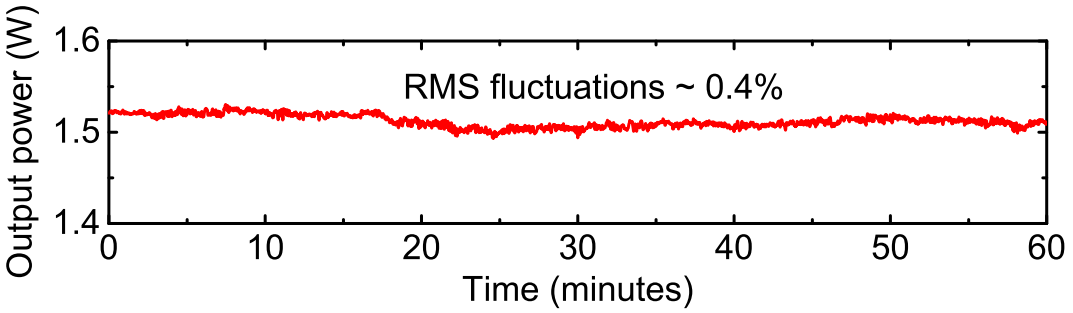

Figure 2.6: Evolution of the output power near 1.5 W over 1-hour time period.

of laser output at 2.85 μm and backward pumping at 915 nm raised the temperature of the fiber tip up to its melting point. This problem will have to be addressed for long-term stability of the amplifier and further scaling of the average output power. It should be noted that holmium- and erbium-doped fibers have different clad sizes and a residual pump coming from the backward pump of holmium-doped fiber increases the temperature on the S1 splice (Fig. 2.1). This is the main reason why the two segments of holmium-doped fiber were pumped separately and a CPS was used on the splice point to eliminate the unabsorbed pump. The cladding size mismatch between the two types of doped fibers limited the maximum 915 nm launchable pump power in the forward direction (i.e. damage occurred at high pump power levels). This problem could be solved by using cladding diameter matched fibers to achieve higher output levels. In addition, the amplifier system could be reduced to a single piece of Ho^{3+}, Pr^{3+}:ZrF_4 fiber by seeding the amplifier with an OPG source delivering higher pulse energies (>10 μJ) directly at 2.85 μm that would also simplify the free space launching.

2.6 Conclusion

In summary, we have demonstrated a 2.85 μm high energy fiber source based on the cascaded amplification in Er^{3+}:ZrF_4 and Ho^{3+}, Pr^{3+}:ZrF_4 fibers. The system delivers 500 ps pulses at 20 kHz with an average output power of 2.45 W, corresponding to a peak power of 245 kW. To the best our knowledge, the obtained pulse energy is the highest ever produced from a fluoride fiber amplifier operating around 3 μm. This work demonstrates the potential for future fluoride fiber amplifiers in the mid-IR to implement practical and efficient short pulsed laser sources for clinical based biomedical applications.

Funding and acknowledgment

Funding: Natural Sciences and Engineering Research Council of Canada (NSERC) (CG101779, CG112389, CG119242); Canada Foundation for Innovation (CFI) (GF072345); Fonds de recherche du Québec - Nature et technologies (FRQNT) (CO201310, FT097991).

Acknowledgment: The authors would like to thank Marc D'Auteuil and Stéphan Gagnon for technical assistance, and Stuart D. Jackson for discussion about fiber doping levels.

Chapter 3

Towards power scaling of 2.8 μm fiber lasers

Y.O. Aydin, V. Fortin, R. Vallée, and M. Bernier

Centre d'optique, photonique et laser, Université Laval, Québec G1V 0A6, Canada

Published in Optics Letters, Vol. **43**, 4542-4545 (2018).

3.1 Résumé

Nous rapportons la démonstration d'un laser à fibre de verre fluoré dopé à l'erbium refroidi passivement et délivrant une puissance de sortie moyenne record de 41.6 W en régime d'opération continu à 2824 nm. La cavité sans épissure est basée sur des réseaux de Bragg intracœurs inscrits directement dans la fibre de verre fluoré active dopée à l'erbium et pompée de façon bidirectionnelle à 980 nm pour distribuer la charge thermique. À notre connaissance, ce résultat correspond à la puissance moyenne de sortie la plus élevée obtenue avec un laser à fibre opérant dans l'infrarouge moyen. La performance à long terme de différents embouts protecteurs est également étudiée lors de l'opération à haute puissance.

3.2 Abstract

We report the demonstration of a 2824 nm passively cooled erbium-doped fluoride fiber laser delivering a record average output power of 41.6 W in continuous wave operation. The spliceless cavity is based on intra-core fiber Bragg gratings written directly in the active erbium-doped fluoride fiber, which is bidirectionally pumped at 980 nm to reduce heat load. To the best of our knowledge, this result is the highest average output power achieved with a mid-infrared fiber laser. The long-term performance of different protective endcaps is also investigated at high power operation.

3.3 Introduction

Mid-infrared fiber laser sources emitting near 3 μm have made significant progress in recent years [175; 137; 76], largely due to the advent of high quality double-clad fluoride fibers, high power InGaAs laser diodes and advances in fiber Bragg gratings (FBGs) inscription technology. Nonetheless, continuous efforts are still needed to improve their performances and meet the requirements of potential high-end applications in material processing [179], medicine [180] and defence & security [80].

Laser emission near 3 μm can be obtained with holmium- (Ho^{3+}) [27], dysprosium- (Dy^{3+}) [46] and erbium- (Er^{3+}) [16] doped fluoride fibers. However, the sources based on Ho^{3+} and Dy^{3+} are actually power limited because of the lack of high power pump diodes. Erbium-doped fiber lasers, on the other hand, can conveniently generate high power 3 μm emission through the $^4I_{11/2} \rightarrow {}^4I_{13/2}$ transition by using powerful commercial InGaAs laser diodes emitting around 976 nm. In this transition, the lifetime of the upper lasing level ($^4I_{11/2}$) is shorter than that of the lower lasing level ($^4I_{13/2}$). However, depleting mechanisms such as energy transfer upconversion (ETU) at high erbium concentrations [37], Pr^{3+} co-doping [22] and cascade lasing [134] are well-known solutions to depopulate the lower state of the 3 μm transition.

To date, most of the high power demonstrations of erbium fluoride fiber lasers reported [175; 37; 38; 31; 181] were based on heavily-doped fluoride glasses (>5 mol.%), which relied strongly on the ETU process ($^4I_{13/2}$, $^4I_{13/2}$) $\rightarrow$ ($^4I_{9/2}$, $^4I_{15/2}$) to reduce the effective lifetime of the lower lasing level. However, these active fibers usually suffer from a high heat load at the pump end due to the strong pump absorption, combined to the large quantum defect and poor thermal properties of fluoride glasses compared with silica. This issue is even more critical when the highly reflective FBG (HR-FBG) is directly written in the core of the active fiber. In fact, the large temperature increase can potentially shift its center wavelength outside the reflection band of the output FBG (LR-FBG), which can lead to instability issues and a decrease of the efficiency. For this reason, the HR-FBG is most often written in the core of a matching undoped single-mode fluoride glass fiber in high power demonstrations [175; 38; 42]. However, this approach requires an additional splice between dissimilar undoped and doped single-mode fluoride fibers, which increases the round-trip losses of the cavity and more importantly causes local hot spots by scattering 3 μm radiation on the strongly absorbing ($\approx$ 20-200 dB/mm) surrounding polymer. Eliminating intracavity splices by writing FBGs in the doped fiber is thus advantageous to simplify the laser cavity assembly, reduce the intracavity losses and remove potential points of failure from the system. Based on that approach, splice-less fluoride laser cavities at 2.82 and 2.94 μm have been demonstrated by Bernier [35] et al. and Faucher et al. [182], but were limited to average output powers around 5 W.

It was also shown in [175] that pumping only from one side of the cavity limits the maximum

launched pump power due to high thermal load on the heavily-doped fiber. Alternatively, the maximum temperature reached at the front end of the active fiber can be significantly reduced by pumping the cavity from both ends, so that they now share the pump heat load. In addition to this, using a longer wavelength pump source also helps to reduce ground state absorption (GSA) and excited state absorption (ESA), which have a significant impact on the temperature increase of the gain fiber [114].

In this work, we report a 41.6 W splice-less passively cooled fiber laser cavity operating at 2824 nm. Intracavity splices are avoided by writing both FBGs into the core of the gain fiber, through the polymer coating, using femtosecond pulses at 800 nm and the scanning phase-mask technique. The laser cavity is pumped at 980 nm in both directions simultaneously (bidirectional pumping) to distribute the heat load in the active fiber. This result represents an eightfold increase in average power compared to previous splice-less laser demonstrations operating in this spectral band. The performance of different endcaps is also evaluated and shows that fiber tip degradation is currently the main limitation for further power scaling.

3.4 Experiment

The experimental setup of the laser is shown in Fig. 3.1. A piece of 6.5 m length of 7 mol.% erbium-doped zirconium fluoride (Er^{3+}:ZrF_4) double clad fiber provided by *Le Verre Fluoré* is used as the gain medium of the laser cavity. The fiber core has a 15 μm diameter with a numerical aperture (NA) of 0.12, in agreement with a measured cut-off wavelength of around 2.4 μm. The fiber cladding has a truncated circular geometry with a diameter of 240x260 μm and an NA of 0.46. It is pumped from both sides (bidirectional pumping) by two high

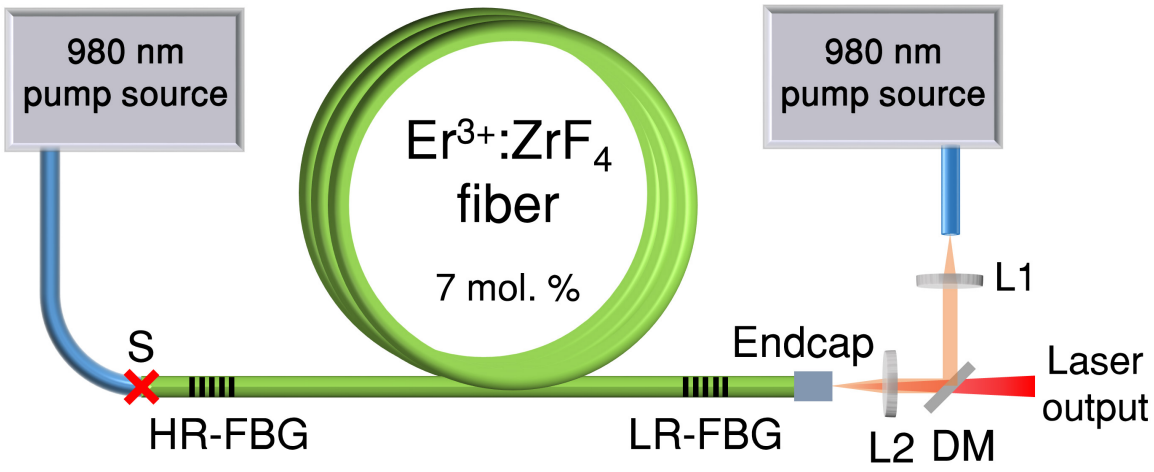

Figure 3.1: Experimental setup of the 42 W fluoride fiber laser at 2.824 μm. S, fusion splice between SiO_2 and Er^{3+}:ZrF_4 fibers; HR-FBG, highly reflective grating (R>99%); LR-FBG, low reflective grating (R=8%); DM, dichroic mirror; L1 and L2, coupling lenses.

power laser diode modules emitting around 980 nm at maximum power. Such pump modules are composed of several multi-mode diodes combined in a tapered fused bundle and provide respectively ∼145 W and ∼55 W of total continuous output power for the forward and backward side, into 220/240 μm, 0.22 NA multi-mode silica fibers, respectively. On the front end, the silica pump fiber is spliced to the fluoride fiber (S in Fig. 3.1) with a technique described in [123]. Free-space pumping at the rear end is realized using a pair of ZnSe aspheric lenses (L1 and L2; f=12.7 mm) with a launching efficiency of 63%, including lens losses, DM losses and mode coupling efficiency. The maximum launched pump powers into the front and rear ends are therefore 137.7 W and 34.5 W, respectively. A dichroic mirror (R >95% at 980 nm, T>96% at 2824 nm) is placed between lenses L1 and L2 to launch the backward pump and to eliminate unabsorbed forward pump.

Two FBGs with respective reflectivity of ≥99.5% (HR-FBG) and 8% (LR-FBG) are written in the core of the Er^{3+}:ZrF_4 fiber by using a 800 nm femtosecond laser, as described in [81]. The FBGs are written directly in the active fiber without removing the protective jacket, a process that preserves most of the pristine fiber's mechanical strength [183]. The Er^{3+}:ZrF_4 fiber and its FBGs are conductively cooled on an aluminum spool with a continuous V-groove. In addition, the thermal contact with the spool is ensured by applying a thin layer of UV-curable low index fluoroacrylate polymer on the whole cavity assembly. An AlF_3-based multimode fiber segment (L≈650 μm) with a 400 μm core size from *Fiberlabs* is used as an endcap in order to slow down OH diffusion in the fiber tip [127]. To fabricate the endcap, a long segment of AlF_3 fiber was first spliced to the gain fiber using a filament-based splicer (Vytran GPX-3000). Then, the spliced fiber was cleaved with a length of 650 μm and a 4° angle to reduce broadband feedback from the output fiber tip. The losses brought by the splicing are less than 1% in such procedure. It is then fixed in a copper V-groove filled with low index fluoroacrylate polymer (n = 1.36) to provide pump guiding from the backward side. A copper plate was also placed on top of the fiber tip to provide efficient conduction cooling and to reduce the temperature increase due to backward pumping. During laser operation, the output fiber facet was continuously purged from moisture by blowing an ultra-pure nitrogen flux on the fiber tip to further slow down its degradation due to OH migration.

Direct FBGs writing in the gain fiber of a high power system imposes some design constraints, particularly when fluoride glass fibers are used. In fact, its low glass transition temperature (Tg≈260 °C) that leads to a relatively poor thermal stability of the femtosecond written FBGs [81]. For that reason, an appropriate thermal annealing is required to stabilize the FBGs properties at a temperature significantly above the fiber core temperature under strong pumping (i.e. large heat loads). As shown in Fig. 3.2, the temperature increases of the fiber's jacket surface was monitored with a thermal imaging camera (Jenoptik, Variocam) equipped with a close-up lens. The temperature of the gain fiber's polymer surface reaches a maximum value of about 80 °C at the maximum heat load (i.e. at 110 W of launched forward pump power,

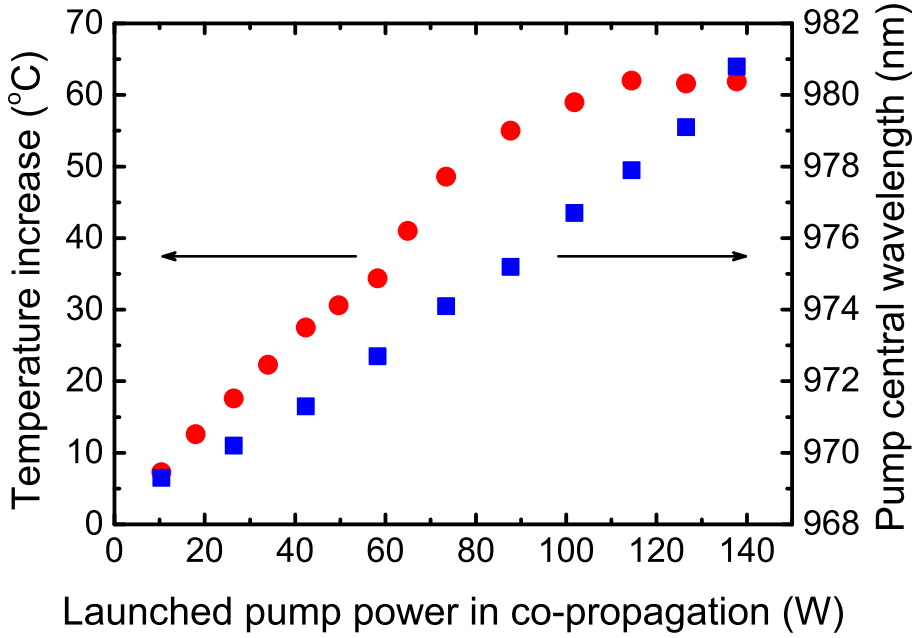

Figure 3.2: Maximum temperature increase of the Er^{3+}:ZrF_4 polymer jacket (red dots) along with pump central wavelength (blue squares) with respect to launched pump power.

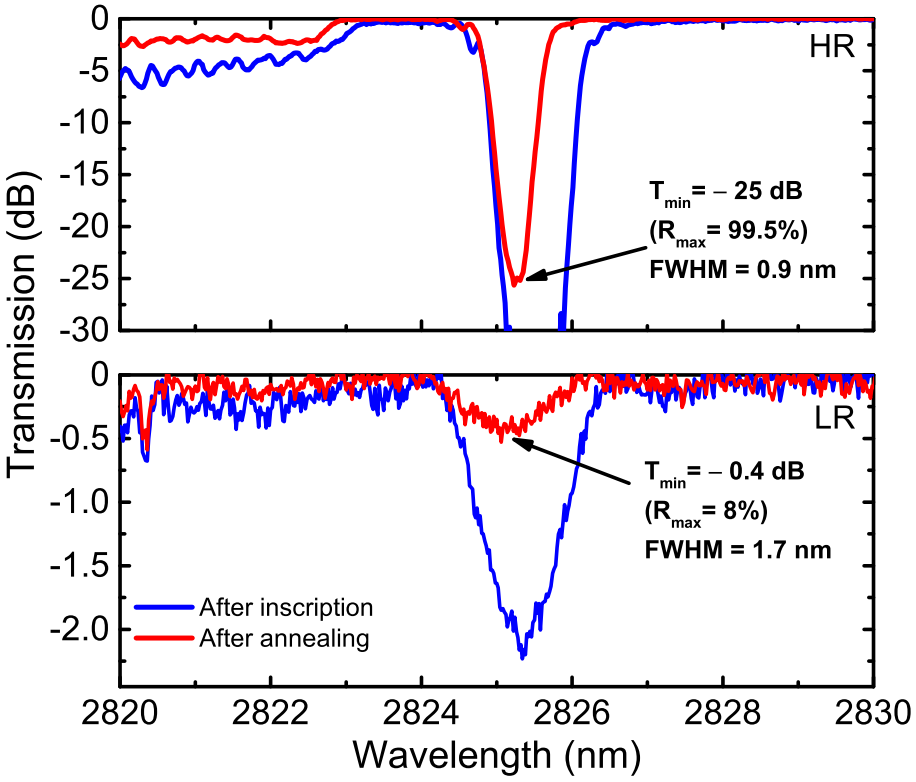

Figure 3.3: Transmission spectra of both HR- and LR-FBG after inscription and after thermal annealing at 150°C for 10 minutes.

as seen in Fig. 3.2) between the fusion splice (S) and the HR-FBG. Based on a simple model of heat conduction, the core temperature of the gain fiber is estimated to reach a maximum temperature of about 110°C. Consequently, the FBGs were thermally annealed at 150 °C for 10 minutes to ensure the long-term stability of their performances. Since the annealing process significantly reduces the FBGs refractive index modulation, a large initial index modulation (i.e. before annealing) was required to obtain a high reflectivity after annealing. We therefore designed the HR-FBG of this particularly challenging cavity with a long length (L = 30 mm), a uniform period (953 nm), a narrow reflectivity bandwidth (FWHM =0.9 nm), and a high final reflectivity (R≥99.5%). On the other hand, the LR-FBG was written with the same uniform period but had a much shorter length (L = 2 mm) to obtain a low final reflectivity (R≈8%) and a relatively large reflectivity bandwidth (FWHM = 1.7 nm) to ensure a good overlap with the HR-FBG during laser operation. Fig. 3.3 shows the transmission spectra of both HR- and LR-FBGs after inscription and after thermal annealing at 150 ℃ for 10 minutes.

3.5 Results and discussion

The output power of the laser was measured with a thermopile detector (Gentec UP25N-250F-H12-D0) as a function of the launched pump power (Fig. 3.4). A maximum of 41.6 W output power is reached when the cavity pumped with 172.2 W of overall (i.e. from both ends) launched pump power around 980 nm. The power of each pump source was increased by the same rate relative to its maximum power to keep the pump wavelength similar from both ends. A slope efficiency of 22.9% is obtained with respect to launched pump power, which is within the typical range for such erbium-doped fiber laser emitting near its maximum gain [38; 35].

Output spectra were also recorded for four different powers (10.8, 19.5, 29, 41 W) using a mid-IR optical spectrum analyzer (Yokogawa, AQ6376, spectral resolution set to 0.1 nm) and are shown in Fig. 3.5. The laser starts to oscillate directly at 2825.3 nm and its emission wavelength slightly drifts (-25 pm/W) as the output power is increased up to 25 W. This negative spectral drift is due to a thermally induced shift of the HR-FBG center wavelength caused by the negative thermo-optics coefficient of fluoride glasses ($dn/dT \approx -14 \times 10^{-6}$ K^{-1}) [184]. For output powers above 25 W, the lasing wavelength stabilizes near 2823.8 nm. We believe this behavior is explained by the temperature induced laser diodes shift of their central wavelengths from 969 nm to about 981 nm, as previously shown in Fig. 3.2. The evolution of the pump central wavelength with respect to the pump power is shown in Fig. 3.2. As a result, both the ground state absorption (GSA) and excited state absorption (ESA) originating from level $^4I_{11/2}$ are significantly reduced. Thus, at sufficiently high pump powers, the local temperature at the front end of the Er^{3+}:ZrF_4 fiber stabilizes so that the HR-FBG central wavelength stops shifting any further. Temperature stabilization of the fiber laser cavity front end was also evidenced in Fig. 3.2 showing the saturation in the temperature increase of the active fiber's jacket polymer surface. The reduced ESA at high pump levels is also known to

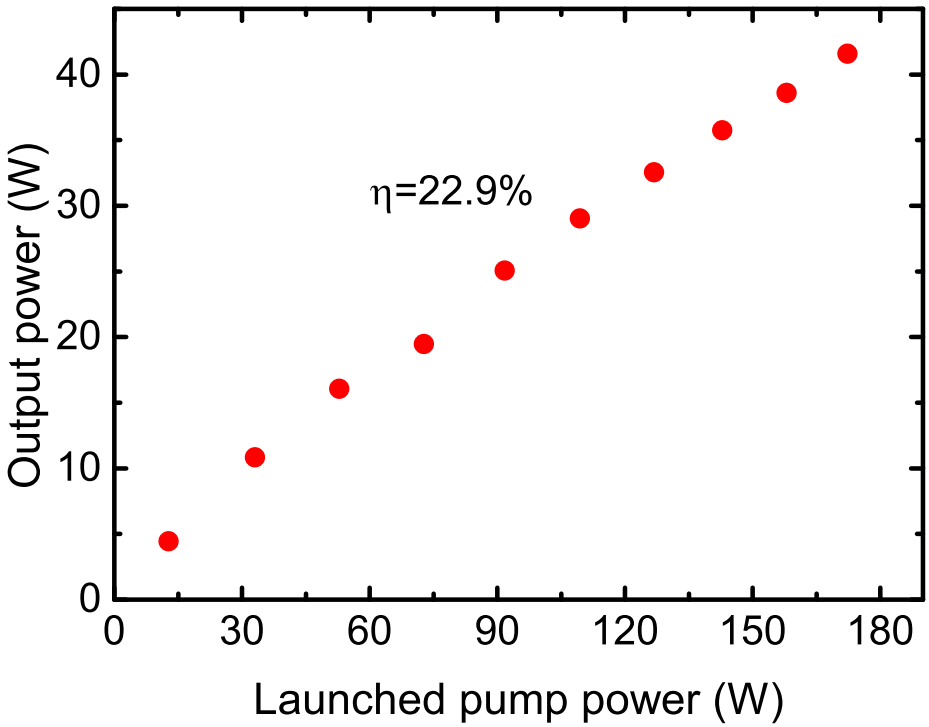

Figure 3.4: Measured output power at 2824 nm as a function of the total (forward and backward) launched pump power around 980 nm.

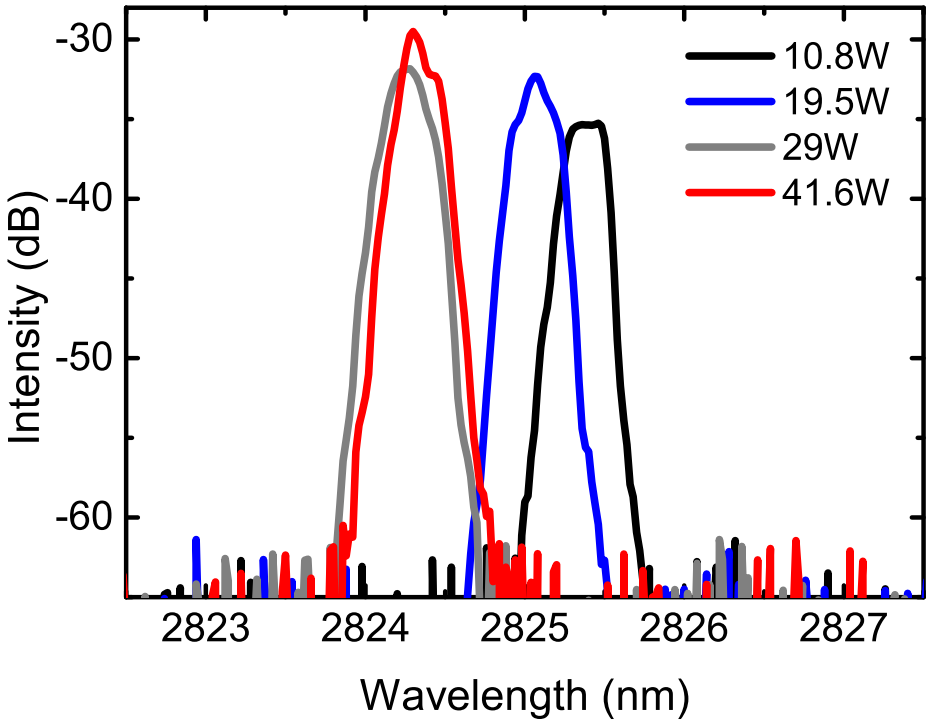

Figure 3.5: Output laser spectra measured at 10.8, 19.5, 29 and 41.6 W.

have a positive effect on the slope efficiency of the laser, as discussed in [114]. It is believed that a pump source with a wavelength between 980 and 984 nm would be optimal to keep temperature of the gain fiber in safe limits and to maximize the slope efficiency of the 2.8 μm transition.

3.6 Fiber tip degradation

Protective endcaps are key components in 3 μm-class lasers to increase the damage threshold associated with OH diffusion in the fiber tip [127] and thus ensure long-term operation. Therefore, we proceeded with a long-term laser test while monitoring the temperature of the AlF_3 endcap. For comparison, we also repeated the experiment with an undoped ZrF_4 endcap (L≈650 μm, Øcore=400 μm) under the same lasing conditions. The tests were performed without nitrogen flux and the laser cavity was operated at 20 W of average power by pumping from the front end side only. The temperature of endcaps was recorded with the same thermal camera described above with a 1 s time delay between each temporal data point. The temper-

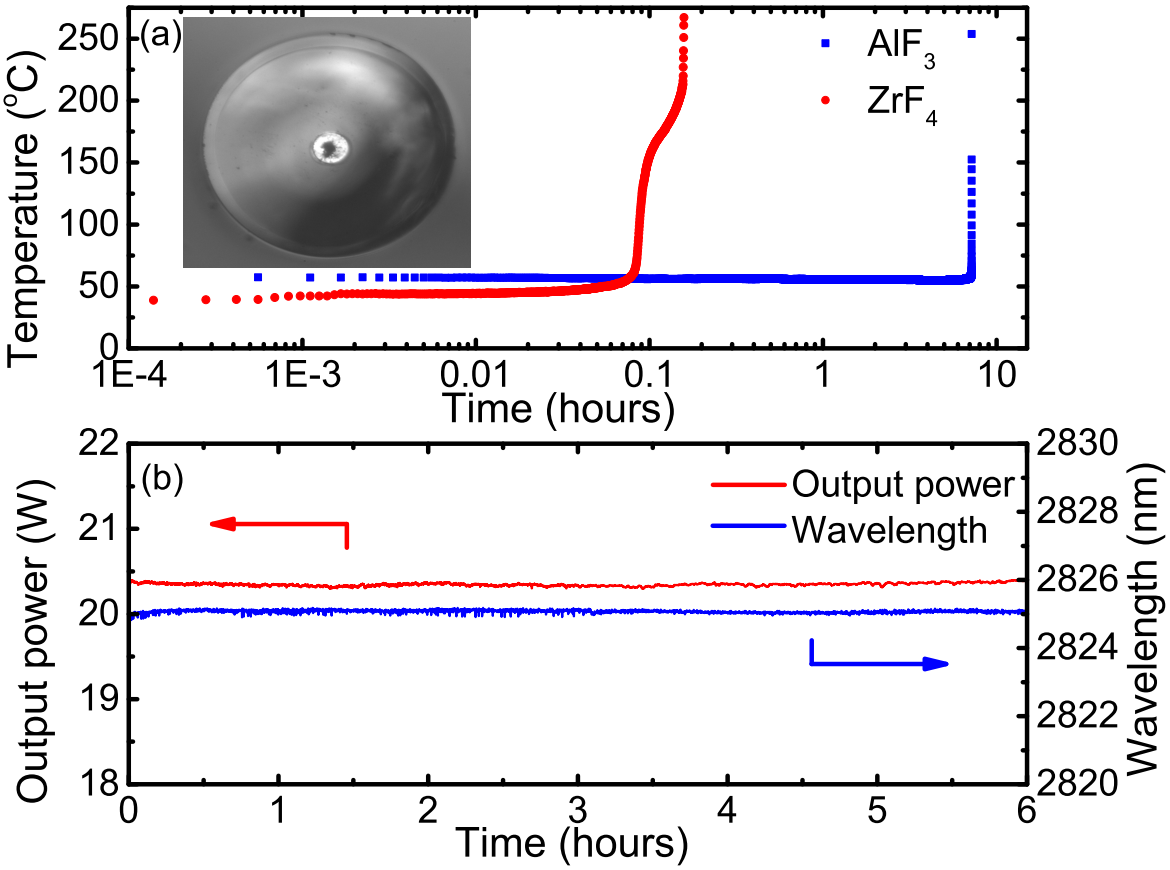

Figure 3.6: (a) Temperature evolution of the AlF_3 and ZrF_4 endcaps at 20 W average output power at 2.8 μm, the optical microscope image of AlF_3 tip (inset) and (b) evolution of the output power and central output wavelength near 20 W over a 6 h time period.

ature evolution of both AlF_3 and ZrF_4 endcaps as a function of time is shown in Fig. 3.6(a). Photo-degradation of the AlF_3 endcap was observed after 7 hours of continuous operation, whereas this duration was less than 10 minutes for the ZrF_4 endcap. While AlF_3 based glasses are at least ten times more resistant to the photodegration process than ZrF_4 glasses [128], these results clearly show that they are still not a good option for long-term operation of high power fiber lasers near 3 μm. The optical microscope image of the degraded AlF_3 tip is shown in inset of Fig. 3.6(a), where catastrophic damage due to OH diffusion is clearly observed. In order to achieve higher output powers and long-term stability, other endcap materials that are less permeable to OH contamination need to be considered. For the power scaling, the temperature on the gain fiber could also be reduced by improving the fiber design, either by lowering the Er^{3+} concentration or by reducing the core-clad ratio. Moreover, using a pump source having a fixed operating central wavelength between 980 and 984 nm would help to reduce the thermal load by lowering the GSA and ESA. In the near future, pump combiners might provide an interesting solution for pumping erbium-doped fluoride fiber cavities from both ends with higher pump launching efficiencies while maintaining heat load to a reasonable level [131].The output power and central output wavelength near 20 W were also measured during a 6-hour stability test. In these measurements, root-mean square (RMS) fluctuations of 0.09% and 0.014% were respectively obtained for the output power and output wavelength (Fig. 3.6(b)).

3.7 Conclusion

In conclusion, we have demonstrated an erbium-doped fluoride glass fiber laser delivering a maximum output power of 41.6 W at 2824 nm using a simple splice-less cavity design. This result is the highest average output power ever achieved from a mid-infrared laser cavity. We showed that fiber tips degradation is still one of the main problems for power scaling and long-term reliability of 3 μm fiber lasers. We also investigated the effect of pump wavelength on the temperature load of the gain fiber. This study represents a significant advance for further power scaling of erbium-doped fiber lasers emitting near 3 μm.

Funding and acknowledgment

Funding: This research was supported by Natural Sciences and Engineering Research Council of Canada (NSERC) (CG101779, CG112389, CG119242); Canada Foundation for Innovation (CFI) (GF072345); Fonds de recherche du Québec - Nature et technologies (FRQNT) (CO201310, FT097991).

Acknowledgment: The authors would like to thank Marc D'Auteuil and Stéphan Gagnon for technical assistance.

Chapter 4

Endcapping of high-power 3 μm fiber lasers

Y.O. Aydin, F. Maes, V. Fortin, S.T. Bah, R. Vallée and M. Bernier

Centre d'optique, photonique et laser, Université Laval, Québec G1V 0A6, Canada

Published in Optics Express, Vol. **27**, 20659-20669 (2019).

4.1 Résumé

La durée de vie des lasers et des amplificateurs fibrés de haute puissance opérant à 3 μm est actuellement limitée par la photodégradation de l'embout de sortie causée par la diffusion OH. Dans ce contexte, nous investiguons la résistance à la diffusion OH d'embouts de protection en verre fluoré et en verre d'oxyde fabriqués à partir de fibres de ZrF_4, AlF_3, GeO_2, SiO_2 et Al_2O_3. À cette fin, les embouts de protection sont fusionnés à la sortie d'un laser à fibre émettant 20 W en régime continu à 2.8 μm et leur dégradation est mesurée sur une période de 100 heures. Tandis que les embouts de protection en verre fluoré se sont totalement dégradés en moins de 10 heures, les embouts en verre d'oxyde ont survécu à l'expérience, bien qu'ils ont démontré un certain degré de dégradation s'étant manifesté par une élévation de la température de la face de sortie en fonction du temps. Afin de pallier à ce problème, nous proposons une nouvelle méthode pour éliminer complètement la diffusion OH consistant en la déposition par pulvérisation cathodique d'une couche mince nanoscopique de nitrure de silicium (Si_3N_4) sur la face de sortie de l'embout de protection. L'efficacité de cette méthode est validée sur des embouts de protection en Al_2O_3, ZrF_4 et AlF_3 qui n'ont montré aucun signe de dégradation après avoir été utilisés sur une période de plus de 100 heures à la sortie d'un laser à fibre haute-puissance opérant à 3 μm.

4.2 Abstract

Fiber tip photodegradation through OH diffusion currently limits the long term operation of high-power fiber lasers and amplifiers operating near 3 μm. To address this issue, we investigate the resistance to OH diffusion of fluoride and oxide endcaps manufactured out of ZrF_4, AlF_3, GeO_2, SiO_2 and Al_2O_3 fibers. To this extent, the endcaps are spliced at the output of a 20 W continuous-wave fiber laser operating at 2.8 μm and their degradation over a 100 h time period is monitored. While the fluoride-based endcaps underwent failure during the first 10 h, their oxide counterparts survived the experiment, although showcasing degradation which was reflected as an increase of the endface temperature over time. To overcome this issue, we propose a novel method to completely suppress OH diffusion which consists in sputtering a nanoscopic diffusion barrier film made of silicon nitride (Si_3N_4) on the output face of the endcap. The effectiveness of the approach is validated on Al_2O_3, ZrF_4 and AlF_3 endcaps which show no sign of degradation after being used for more than a 100 h at the output of a 3 μm high-power fiber laser.

4.3 Introduction

Fiber laser technologies are playing an instrumental role in the development of various applications [185]. However, as the output power of fiber laser systems increases, the likelihood of end-face damage increases accordingly. In the case of the well-known Yb^{3+}:silica fiber lasers operating at 1 μm, such failure is related to the fact that their output intensity exceeds the air-glass surface damage threshold, and damage occurs either due to overheating in continuous-wave (CW) regime or laser-induced breakdown due to intense pulses [186]. To mitigate this issue, fiber-based endcaps, spliced at the output of the fiber laser systems, have been developed to allow the beam to expand in a controlled manner and therefore lower its intensity below the glass' damage threshold. Such endcaps have enabled the demonstration of fiber laser systems delivering over 100 kW of output power in CW operation [4].

Fluoride-based fiber lasers provide the means to achieve powerful laser emission between 2.8 and 4 μm [50; 51; 187; 188], although their current output power is significantly less than their silica counterparts. Yet, we recently reported an erbium-doped zirconium fluoride fiber laser delivering 42 W of CW output power at 2.83 μm which highlighted the potential of 3 μm fiber lasers for further power-scaling up to the 100 W level [50]. Such all-fiber laser sources are coveted in the development of biological tissue ablation and remote-sensing applications given their excellent overlap with the OH bond's strong vibrational absorption band, their unrivalled beam-quality as well as their compact yet rugged design [166]. Nonetheless, the widespread deployment of high-power 3 μm-class all-fiber lasers is currently hindered by the short lifetime of such laser sources due to fiber tip degradation. Contrarily to silica fiber laser systems, this issue is the direct consequence of operating within the OH absorption band at 3

μm and the hygroscopic nature of fluoride-based glasses. Through analytical modeling, it was shown that the time elapsed before catastrophic failure of the fluoride fiber tip was inversely proportional to the square of the 3 μm output power [127]. As a result, for a 20 W power level, the all-fiber cavity reported in [50] lasted less than 10 h before the fiber laser's fluoride-based endcap underwent catastrophic failure due to OH diffusion.

To address this issue, this work investigates the efficiency of different endcap materials to mitigate fiber tip degradation of 3 μm-class high-power fluoride fiber lasers. To this extent, we monitored over a 100 h time period the degradation of endcaps made out of fluoride-based glass fibers (zirconium and aluminum fluoride), oxide-based glass fibers (fluorogermanate and silica) as well as single crystal sapphire fibers when spliced at the output of a high-power fiber laser operating near 3 μm. Upon experimentation, fluoride-based endcaps underwent catastrophic failure after less than 10 h during the test, suggesting they should only be used in low-power (Watt - level) 3 μm fiber laser systems. Although the oxide and crystal-based endcaps survived the 100 h long experiment, they showcased a significant rise of their temperature over time, hence indicating they should only be used in medium-power (20 W - level) fiber laser systems to ensure long term operation. Finally, this work proposes a definitive method to suppress OH diffusion within any type of endcap material by using an efficient OH diffusion barrier. This method, which consists in sputtering a thin-film of silicon nitride (Si_3N_4) on the output face of the endcap, was validated on ZrF_4, AlF_3 and Al_2O_3 endcaps which have shown no sign of degradation under high-power 3 μm radiation over more than 100 h of experimentation.

4.4 Experimental setup

The home-made high-power 3 μm-class fiber laser used to investigate the degradation of the different endcap materials is depicted in Fig. 4.1 and is similar to the system reported in [50]. Briefly, it is made out of a 6.5 m double-clad 7 mol % erbium-doped fluorozirconate (Er^{3+}:ZrF_4) fiber manufactured by *Le Verre Fluoré*. The 15 μm diameter core of the fiber has a numerical aperture of 0.12 enabling singlemode operation above 2.4 μm. The fiber laser cavity is bounded by two intracore fiber Bragg gratings (FBGs) written through the polymer of the fiber using femtosecond pulses with the scanning phase-mask technique [81; 189]. The entrance high-refectivity (HR) FBG has a reflectivity > 99 % at 2.825 µm while the output low-reflectivity (LR) FBG has a reflectivity of 8 %. The active fiber and the HR and LR-FBGs were spooled on a 32 cm diameter grooved and fan cooled aluminum spool, and secured with UV-cured polymer.

In contrast to the system reported in [50], the system was solely pumped from the forward end by a 135 W commercial InGaAs 980 nm multimode laser diode whose silica delivery fiber was fusion-spliced (S1) to the Er^{3+}:ZrF_4 fiber. At the output of the fiber laser cavity, a residual cladding pump stripper (RCPS) was fabricated by applying high-index UV-cured polymer on

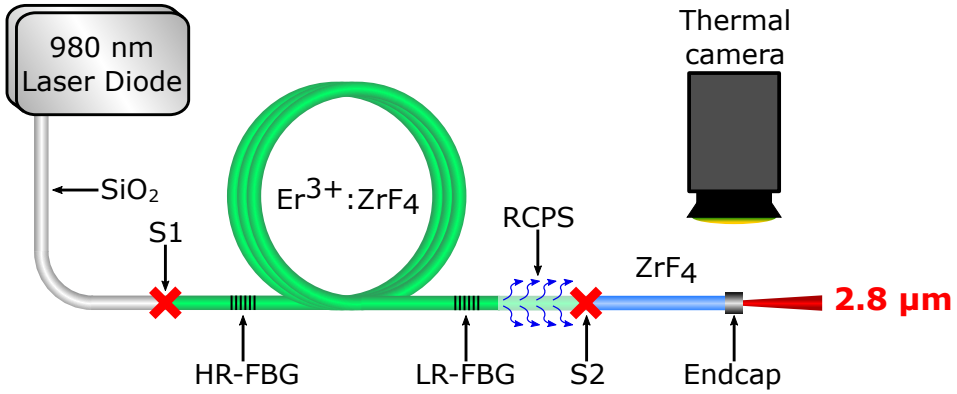

Figure 4.1: Experimental setup used to monitor the degradation over time of the different endcaps when subjected to 20 W of output power at 3 μm.

the bare Er^{3+}:ZrF_4 fiber. This pumping scheme enabled an efficiency of 23 % with respect to the launched pump and a pump power limited maximum output power of around 29 W at 2.825 µm. A singlemode fusion-splice (S2) was made between the output Er^{3+}:ZrF_4 fiber and a mode-matched passive ZrF_4 relay fiber to carry out multiple endcap degradation experiments. The relay fiber has a 15 μm core diameter, a numerical aperture of 0.12 and a 250 μm cladding diameter. The high-power all-fiber laser cavity was operated at an output power of around 20 W for all degradation experiments.

The degradation over time of the various endcaps was monitored by measuring the temperature of the endcaps' output face with a thermal camera (Jenoptik, Variocam) equipped with a close-up lens. Simultaneously, the output power of the laser system was recorded with a thermopile detector (Gentec E-O, UP25N-250F-H12-D0) to ensure it operated at a 20 W output power level throughout the experiment. It should be noted that the laser cavity was operated at this power level with the same nominal performances for over 800 h during these experiments with a stability similar to the one showcased in [50], i.e. RMS fluctuations less than 0.1%.

4.5 Endcap splicing and manufacturing

In this investigation, we studied the degradation of 6 different endcap fiber materials: fluorozirconate (ZrF_4 - BaF_2 - LaF_2 - AlF_3 - NaF - SrF_2 - HfF_4), fluoroaluminate (AlF_3 - $AlCl_3$ - NaF - ZrF_4 - YF_3 - SrF_2 - BaF_2 - LaF_2), fluorogermanate (GeO_2 - ZnO - PbO - K_2O - PbF_2), silica (SiO_2) and sapphire single crystal (Al_2O_3). All endcap materials were provided in fiber (or single crystal fiber) form and their specifications are presented in Table. 4.1. The silica fiber was home-drawn using a *Heraus* preform composed of a F-300 pure silica core and a F-320 fluorine-doped silica cladding [190]. Manufacturing an endcap out of a 50 %-doped Er^{3+}:YAG single crystal ($Y_3Al_5O_{12}$) fiber was also studied given the unavailability of an undoped YAG fiber. Moreover, in the remainder of this work, the endcap materials will be referred to by their main constituent, for example ZrF_4 for fluorozirconate.

The endcaps were fusion-spliced to the passive ZrF_4 relay fiber using a Vytran GPX system equipped with an iridium filament (Vytran, FRAV4). For the ZrF_4 endcap, the filament was positioned at the splice point between the relay fiber and the endcap fiber. All other fibers were spliced to the ZrF_4 relay fiber by offsetting the longitudinal position of the filament in direction of the endcap fiber material as detailed in [194]. Once the fusion splice was achieved, the endcap fiber material was cleaved at a given length with a Vytran LDC cleaver. Images of the final endcaps resulting from this manufacturing process are presented in Figs. 4.2(a)-4.2(c). Typical output power losses at 2.83 μm after splicing the fluoride and GeO_2 endcaps were around 4% and 8%, respectively, including fiber transmission losses and Fresnel reflections at the output endcap face and splice interface. Prior to the degradation tests, the assembly was secured using a low-index UV-cured polymer in a copper V-groove to ensure good heat conduction from the endface to the heat sink. Special care was taken to limit the length of the endcap protruding out of the copper V-groove. In contrast to natural convection, which was used in the past to study the degradation of ZrF_4 fiber tips [127], thermal conduction was chosen in the current experiment given this cooling method is more efficient, thus limiting at maximum the endface temperature.

In contrast to fluoride and GeO_2 fibers, the SiO_2, Er^{3+}:YAG and Al_2O_3 fibers form no thermal bonds when spliced to the ZrF_4 glass fiber. To overcome this limitation, we relied on the fact that the thermal expansion of ZrF_4 glass is significantly larger than that of all the oxide-based fiber materials tested, as seen in Table 4.1. Hence, by pushing in a controlled manner the oxide-based fiber material into the ZrF_4 fiber, after the former has been heated sufficiently, a permanent and robust joint is created as seen in Fig. 4.2(d)-(f). The joint's strength is

Table 4.1: Endcap specifications[a].

Endcap	Manufacturer	n[b]	α[c] [$\times 10^{-6}$ K^{-1}]	T_g[d] [°C]	$\varnothing_c$[f] [μm]	L[g] [μm]
ZrF_4	Le Verre Fluoré	1.49	17.2	265	200	480
AlF_3	Fiberlabs	1.46	18.6	390	200	450
GeO_2	Infrared Fiber Systems	1.83	10.9	420	230	380
GeO_2	Le Verre Fluoré	1.83	10.9	420	230	410
SiO_2	Heraeus F-300	1.42	0.55	1175	242	190
Er^{3+}:YAG	Shasta Crystals	1.79	6.14	$T_f = 1940$[e]	220	320
Al_2O_3	Shasta Crystals	1.72	5 - 5.6	$T_f = 2030$[e]	240	N.A.

[a] Optomechanical properties taken from [190; 191; 192; 193].
[b] Refractive index around 3 μm.
[c] Thermal expansion coefficient.
[d] Transition temperature.
[e] Melting temperature.
[f] Core diameter.
[g] Length.

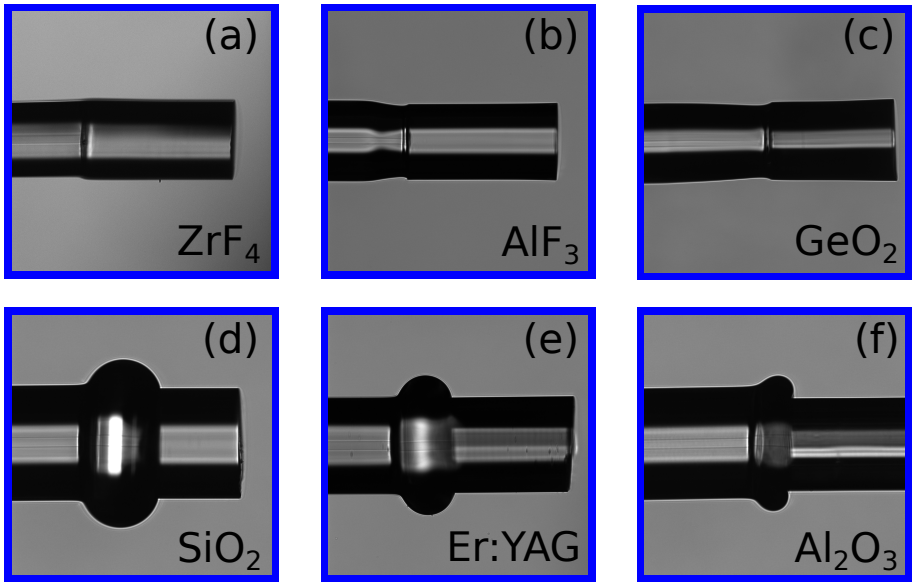

Figure 4.2: Photographs of the different endcaps taken with the imaging system of the Vytran GPX.

provided by the ZrF_4 glass which tightly wraps around the oxide-based fiber material once the splice point cools down. In fact, all fusion-splices resulting from this splice procedure were proof-tested at a tension of 200 g (roughly 4.4 MPa) prior to being used in the tests. It should be noted that this splicing method was also used to achieve the splice (S1) between the silica delivery fiber of the InGaAs multimode laser pump diode and the active Er^{3+}:ZrF_4 fiber shown in Fig 4.1. A similar splicing method, relying on the same principle but using a CO_2 fusion-splicer, was recently shown to enable robust single-mode splices between silica and ZrF_4 fibers [119]. This principle was most-likely also employed in a number of other reports where silica and ZrF_4 fibers, or silica and chalcogenide fibers, were fusion-spliced [195; 196; 125; 197; 116]. The typical output power losses at 2.83 μm after splicing the SiO_2, Er^{3+}:YAG and Al_2O_3 endcaps were 8%, 10% and 16%, respectively.

In the case of the SiO_2 and Er^{3+}:YAG endcaps, it was possible to cleave the fiber material after the splice process, as seen in Fig. 4.2(d)-(e), and cool the assembly in the same manner as the fluoride and GeO_2-based endcaps. It should be noted that the length of the SiO_2 endcap was shortened as much as possible due to the fiber's high absorption losses of ~ 25 dB/m near 2.825 μm. For the Er^{3+}:YAG endcap, cleaving was greatly simplified by the fact that that the crystalline planes of the Er^{3+}:YAG fiber are perpendicular to its optical axis, as shown in [198]. A photograph of the splice interface between the ZrF_4 fiber and the SiO_2 and Er^{3+}:YAG endcap is shown in Fig. 4.3(a)-(b). From these images, it is clear that the interface between the SiO_2 endcap and the ZrF_4 fiber is smooth and that it does not deteriorate the quality of the laser beam. For the Er^{3+}:YAG endcap, one can see some bubbles at the interface which might degrade the beam-quality if they are located in the beam path. However, we believe

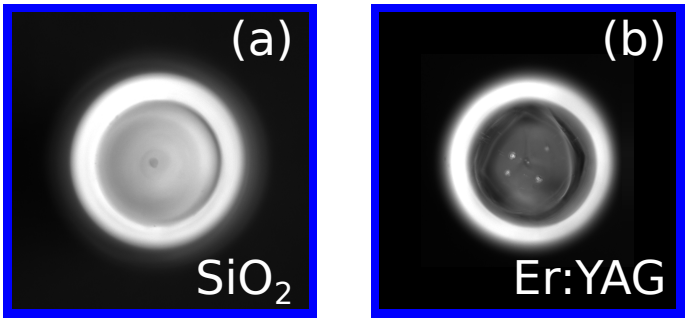

Figure 4.3: Photographs of the interface between the ZrF_4 relay fiber and (a) the SiO_2 and (b) the Er^{3+}:YAG endcaps.

optimization of the splice recipe can prevent the formation of such bubbles and enable flawless splice interfaces similar to that of the SiO_2 endcap. For the sapphire single crystal fiber, it was not possible to cleave or polish the fiber material without breaking the splice point. This stems from the fact that the crystalline planes are at 45° with respect to the optical axis of the fiber and also from its high mechanical strength. Therefore, the whole length of the sapphire fiber (50 cm) was kept for the degradation test. Given the sapphire fiber is coreless, any attempts at cooling the fiber extremity using the copper assembly described above resulted in leakage of the 3 μm signal fom the side and the eventual failure of the assembly. Therefore, the sapphire fiber tip was tested under natural heat convection instead of heat conduction as for the other endcaps.

4.6 Results and discussion

4.6.1 Endcap degradation

Figure 4.4 showcases the degradation of the various endcaps under the action of 20 W CW output power at 2.83 μm over a 100 h time period. The initial temperature of the various endcaps varies between 40 - 75 °C, a variation accounted for by the difference of initial OH compound concentration, absorption coefficient at 2.83 μm, thermal conductivity [127] as well as their refractive index which determines the intensity of the Fresnel reflection at the endcap interface. As reported in [50], the fluoride fiber-based endcaps did not survive the experiment more than 10 h. While the initial temperature of the multimode ZrF_4 fiber endcap was the lowest of all the endcaps that were tested (40 °C), it underwent catastrophic failure after only 10 minutes. The degradation curve of the ZrF_4 endcap, as well as the time elapsed before failure, are in agreement with the results found in [127]. It should be noted that in the latter, the fiber tip experienced natural heat convection which increased the thermal resistance between the fiber and its surroundings, and resulted in an accelerated degradation rate. As for the AlF_3 endcap, it survived for about 10 h under similar conditions given its glass matrix is more than ten times more stable in water than that of ZrF_4 [128]. It is therefore clear that

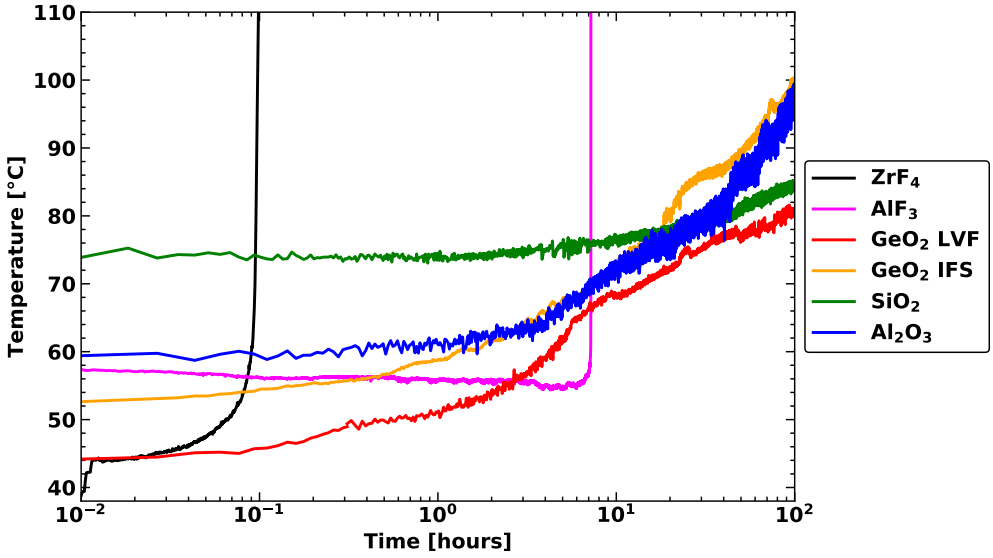

Figure 4.4: Measured temperature of the endcaps' output face as a function time for a constant 3 μm output power of 20 W.

AlF_3, and even more so ZrF_4,-based endcaps are not suitable long term solutions when dealing with output powers above a few watts around 3 μm. Based on the different reports having used AlF_3 endcaps to protect fiber laser systems from photo-degradation [150; 156], it can be stated that AlF_3 endcaps should be restricted to 3 μm fiber laser systems delivering output powers of a few watts in order to guarantee their long term operation. On the other hand, multimode ZrF_4 fiber endcaps should only be used in low-power systems where the output power is kept below the watt-level range. However, due to their perfectly matched refractive index, ZrF_4 endcaps produce the lowest splice interface reflection among all the tested endcaps; a significant advantage for mode-locked and in-amplifier supercontinuum Er^{3+}:ZrF_4 fiber laser systems. In both cases, the performance of these systems is greatly limited by parasitic lasing at 2.8 μm and it is therefore paramount to use an endcap producing the lowest possible feedback [74; 76].

From Fig. 4.4 it can be seen that all the oxide-based and crystalline endcaps that were tested survived the 100 h long degradation experiment. However, the experiment also revealed that their temperature increased over time, hence indicating the existence of some degradation phenomenon. Table 4.2 summarizes the degradation performance of the SiO_2 and GeO_2-based endcaps. The initial temperature of the SiO_2 endcap (74 °C) is significantly higher than that of the GeO_2 endcaps ($\approx$ 50 °C), a direct result of the strong absorption of SiO_2 around 3 μm. Given the constant ambient temperature during the experiment of 20 °C, the initial temperature rise of the SiO_2 endcap per watt of output power at 3 μm is found to be 2.7 °C/W while that of GeO_2 endcaps is roughly twice less, i.e. 1.4 °C/W. Hence, in the perspective of

Table 4.2: SiO_2 and GeO_2 endcap performances.

Endcap	T_i[a] °C	ΔT_i / ΔP[b] °C / W	$T_{i,100W}$[c] °C	$\Delta T/\Delta t$[d] °C / hr
GeO_2 LVF	44	1.20	140	0.37
GeO_2 IFS	53	1.65	218	0.47
SiO_2	74	2.70	290	0.10

[a] Initial temperature.
[b] T_i variation with 3 μm output power.
[c] Extrapolated T_i at 100 W of output power.
[d] Temperature variation over time.

power-scaling the output power of 3 μm-class all-fiber lasers to 100 W, we can expect a SiO_2 endcap to reach an initial temperature of 290 °C while the temperature of a GeO_2 endcap would be between 140 - 218 °C. This allows us to conclude that GeO_2 endcaps are better candidates for high-power 3 μm systems since the splice between the SiO_2 endcaps and the ZrF_4 fiber cannot sustain temperatures in excess of the transition temperature of ZrF_4 (i.e. 270 °C [191]). Nonetheless, for medium-power systems (≈20 W), SiO_2 fibers could be considered a better alternative than GeO_2 fibers, given their degradation rate is more than three times slower than that of GeO_2. This fact has enabled the SiO_2 endcap to reach after 100 h a similar final temperature as the GeO_2 (*LVF*) endcap although their initial temperature difference was 33 °C. Moreover, SiO_2 fibers, comparatively to GeO_2 fibers, are less expensive and significantly easier to handle and process. Additionally, the refractive index of SiO_2 around 3 μm (1.42) is closer to the refractive index of ZrF_4 glass (1.49) than that of GeO_2 (1.83). This characteristic also favors SiO_2 endcaps in the design of powerful MIR mode-lock or in-amplifier fiber lasers [74; 76], as discussed earlier. It should be noted that both GeO_2 endcaps that were tested behaved similarly during the experimentation, although the endcap manufactured out of the fiber provided by *Le Verre Fluoré* had a lower initial temperature. However, it is difficult to assess if this is the result of a less OH diffusion prone glass composition or a more efficient cooling.

As stated earlier, the Al_2O_3 fiber tip surprisingly showed signs of degradation over time under the influence of high power 3 μm laser light. The initial temperature of the Al_2O_3 fiber tip was 60 °C and its final temperature is 97 °C, which results in a 0.37 °C/h degradation rate. While the initial temperature and degradation rate of the Al_2O_3 fiber tip is comparable to those of GeO_2 endcaps, it should be noted that the former experienced natural convection instead of heat conduction, a condition which accelerates degradation by easily a tenfold [127]. Therefore, we believe Al_2O_3 endcaps are potentially an interesting solution for high-power 3 μm fiber laser systems, contingent upon the ability to manufacture endcaps out of single crystal Al_2O_3 fibers. An alternative to manufacturing such endcaps would be to inscribe depressed cladding single-mode waveguides with femtosecond pulses in the Al_2O_3 rod fiber, as shown recently in [199]. This method would preserve the beam-quality of the 3 μm fiber laser although long

lengths of Al_2O_3 fiber are used for beam delivery purposes.

Similarly to fluoride-based endcaps, we believe the degradation witnessed in the SiO_2 and GeO_2 endcaps is related to ambient water vapor diffusion within the glass matrix. In both cases, the OH vapor could be incorporated into the glass matrix in the form of GeOH or SiOH groups, as discussed in [200; 201; 202; 203]. It is unlikely that water vapor diffused within the matrix of the single-crystal Al_2O_3 fiber given the high degree of order of its crystalline matrix. Instead, we believe the temperature increase observed during the experiment is related to water vapor adsorption at the polished surface of the sapphire fiber [204]. The occurrence of water adsorption is caused by the fact that at the surface of the single-crystal sapphire fiber, the chemistry of a pure crystal does not hold given Al-O-Al compounds are deprived of neighboring compounds. This gives rise to various chemical mechanisms through which OH can bind itself to the surface and alter the latter's properties with increasing pressure, humidity, temperature and time. However, further investigations need to be conducted in order to validate how ambient OH vapor interacts with the different oxide-based and crystalline endcaps

As for the Er^{3+}:YAG endcap, it could not be tested given its temperature at a 3 μm power level of 2.4 W was already around 120 °C. This temperature was measured at the splice point between the relay fiber and the Er^{3+}:YAG endcap. By analyzing with a near-infrared optical spectrum analyzer the output of the 2.83 μm all-fiber laser cavity, a clear, yet weak, peak at 980 nm was observed. This indicated that some residual cladding pump remained at the output of the laser cavity which was absorbed by the heavily-doped (50%) Er^{3+}:YAG endcap and caused its excessive heating. In spite of this, we believe undoped YAG single crystal fibers are highly interesting endcap materials given they possess thermal and mechanical properties similar to Al_2O_3 fibers while simultaneously offering the possibility to be easily processed into endcaps at the tip of ZrF_4 fibers. It should also be noted that coreless calcium fluoride (CaF_2) crystals have been recently used to endcap 3 μm fiber laser systems operating at 16 W near 2.8 μm [131]. However, given the unavailability of such material to the authors, it was not possible to evaluate its long term degradation behaviour in the current experiment.

4.6.2 Si_3N_4 coatings for high-power 3 μm fiber lasers

In order to inhibit in a definite manner OH diffusion within endcap materials, we propose to coat the output face of the endcap with a nanoscopic thin-film of silicon nitride (Si_3N_4). Such materials are already extensively used in electronics as a diffusion barrier for SiO_2 dielectric layers or passivation layers in flexible electroluminescent devices [205].

In this experiment, the Si_3N_4 thin-films were deposited on the facet of the endcaps using reactive ion beam-assisted double magnetron sputtering as described in [206] under a 1.46×10^{-3} Torr environment. The target material was a 6" diameter 99.99 % pure silicon

disk. The temperature of the substrate was kept at 115 °C and deposition of the thin-film was done at a 0.24 nm/s. The argon gas flow was maintained at 32 sccm during the sputtering process and the reactive gas nitrogen gaz (22 sccm) was introduced into chamber by the ion source. The uniformity of the deposited thin-film was enhanced by a rotating the substrate holder at 80 rpm.

Figure 4.5 compares the degradation of Si_3N_4-coated and uncoated ZrF_4, AlF_3 and Al_2O_3 endcaps under the impact of 3 μm light over a 100 h long time period. For the ZrF_4 and AlF_3 endcaps, the Si_3N_4 coating had a 25 nm thickness and the output power of the 3 μm fiber laser was 7 W, while in the case of the Al_2O_3 endcaps they were 100 nm and 20 W, respectively. For both ZrF_4 and AlF_3, the coating thickness was limited to less than 1% of the wavelength to limit the Fresnel reflection given the high refractive index of ($n \sim 1.95$) Si_3N_4. Moreover, all endcaps experienced natural convection to accelerate the photodegradation process. From Fig. 4.5 it is clear that the Si_3N_4 coating inhibits OH diffusion for all the tested endcaps given no increase of temperature over time is recorded. It also demonstrates that Si_3N_4 coatings can be applied on a variety of fiber materials.

However, some Si_3N_4 coatings showed signs of cracking a few months after their deposition upon the fibers as result of high surface stresses. Such stresses can nonetheless be relieved through the deposition of thinner Si_3N_4 thin-films. Hence, future investigation will attempt to find a thickness range where Si_3N_4 coatings do not crack over time while simultaneously preserving their OH impermeability. These investigations will also consider the introduction of oxygen within the Si_3N_4 matrix which has been show to improve its flexibility [207]. Finally, the Si_3N_4 coating optimization will also be facilitated by the number of potential endcap

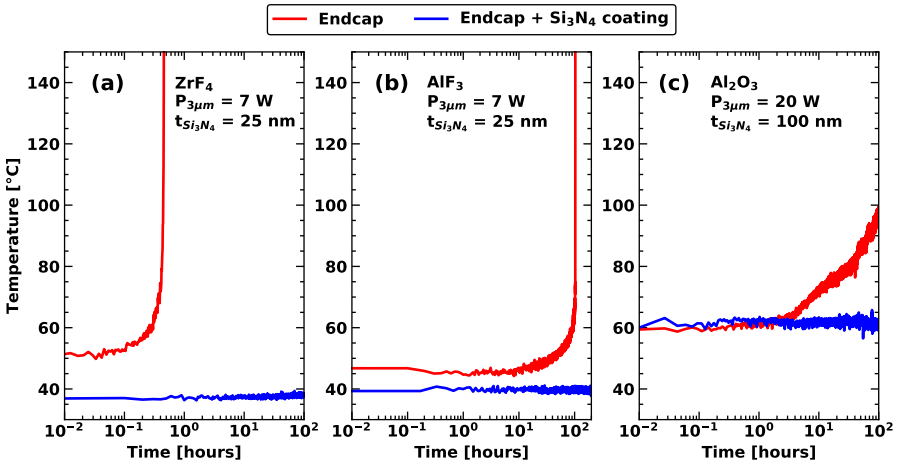

Figure 4.5: Measured temperature of the (a) ZrF_4, (b) AlF_3 and (c) Al_2O_3 endcaps compared to their Si_3N_4 coated counterparts as a function of time. The 3 μm output power and Si_3N_4 coating thickness used for the ZrF_4 and AlF_3 endcaps were 7 W and 25 nm, respectively, while those for the Al_2O_3 endcap were 20 W and 100 nm, respectively.

substrates upon which they can be deposited, i.e. ZrF_4, AlF_3, GeO_2, SiO_2, YAG and Al_2O_3. We believe that an optimized endcap properly coated with Si_3N_4 will enable the long term operation ($>$ 10,000 h) of 100 W - level 3 μm-class fiber laser systems in the near future. It should be noted that silicon nitride or silicon oxynitride could also be used to coat the outer glass cladding of optical fibers. Such coatings could constitute a transparent alternative to thin carbon, metallic or ORMOCER® coatings which have been shown to provide an excellent protection against OH diffusion within SiO_2-based fibers [208; 209; 210].

4.7 Conclusion

In this work, the OH degradation of various endcaps spliced at the output of a 20 W all-fiber laser at 3 μm was monitored over a 100 h time period. This investigation showed that fluoride, i.e. ZrF_4 and AlF_3,-based endcaps lasted for less than 10 h before undergoing catastrophic failure, hence indicating they should only be used for low-power applications. On the other hand, the oxide-based endcaps (GeO_2 and SiO_2) as well as the tip of a Al_2O_3 fiber survived the experiment, which makes them interesting endcap solutions for medium-power systems ($\sim$ 20 W). To the best of our knowledge, this is the first report in which oxide-based materials are spliced and processed into endcaps at the output of a fluoride fiber laser. Nonetheless, all oxide materials showcased a clear temperature increase over time, an observation which is believed to stem from OH diffusion in the GeO_2 and SiO_2 glass matrix or presumably OH adsorption in the case of Al_2O_3.

In order to inhibit OH interaction with endcap materials under the irradiation of intense 3 μm light, we also propose in this work to coat the output face of endcaps with a silicon nitride (Si_3N_4) thin-film. The effectiveness of the proposed method is demonstrated on Si_3N_4 coated ZrF_4 and AlF_3 endcaps, as well as on an Al_2O_3 fiber tip. Upon illumination with 3 μm light for a 100 h, the coated endcaps and fiber tip showed no sign of degradation, whereas their uncoated counterparts either underwent catastrophic failure (ZrF_4 and AlF_3) or showed a significant temperature rise (Al_2O_3). We believe optimized Si_3N_4-coated endcaps will allow the long-term operation of 100 W-level 3 μm class all-fiber lasers in the near future, and spark the development of cutting-edge mid-infrared applications.

Funding and acknowledgements

The authors wish to thank Yannick Ledemi for insightful discussions and acknowledge the financial support of the Canada Foundation for Innovation (CFI) (5180), the Fonds de Recherche du Québec—Nature et Technologies (FRQNT) (144616), the Natural Sciences and Engineering Research Council of Canada (NSERC) (IRCPJ469414-13, CG112389).

Conclusion and perspectives

The objective of this dissertation is to present the achievement of high-power fluoride fiber sources operating near 3 μm. This objective has been clearly achieved by the demonstration of the most efficient and the most powerful output performances through three main fluoride fiber laser systems based on different architectures. The critical in-fiber components of these fiber laser sources such as single- and multi-mode fiber splices, fluoride to silica splices, endcaps and FBGs were also fabricated in the scope of this project. The previous works and the experimental studies during the PhD project showed the various major challenges which need to be addressed from both theoretical and practical perspectives for further improvement of output laser parameters. Despite the world record output of slope efficiency, average output power and pulse energy near 3 μm have been achieved, a high level of long-term output power stability and long-term operating time of high-power 3 μm fluoride fiber lasers were big question marks due to the fiber tip degradation phenomenon from early part to last months of this project. Therefore, the dissertation ended up with a solution that proposes a method to eliminate the fiber tip degradation problem. In this way, the research output of this study is not only the experimental demonstrations of 3 μm fluoride fiber laser systems and their components but also serves as a reference work for further fluoride fiber laser studies to minimize potential problems. The summary of the thesis and future work are given in the following subsections.

Summary

This dissertation started by discussing the motivation behind this project along with the main applications for 3 μm fiber lasers. The historical development of 3 μm fluoride fiber lasers and their major components were reviewed in the same chapter. The first chapter also showed the theory of 3 μm laser transition through different gain media and described the approaches and methods to achieve an efficient high-power 3 μm emission. In addition, challenges associated with high-power laser operation in fluoride fiber-based systems were highlighted and solutions were proposed for each problem.

Chapter 1 presented a passively-cooled Er^{3+}:ZrF_4 cascade fiber laser operating at 2.8 μm and 1.6 μm, simultaneously. The influence of the 1.6 μm transition on 2.8 μm emission was studied

and an ESA process which recycles the excitation back to the upper laser level was identified in Er^{3+}:ZrF_4 fiber. Thanks to this ESA, an optical-to-optical conversion efficiency of 50% was achieved at 2.8 μm. The main drawback of this configuration was the temporal instabilities which limited maximum output power to 12.95 W and led to catastrophic failures. The results of this research were published in the prestigious journal "Optica" in February 2017.

A sub-ns pulsed fluoride fiber amplifier was reported in Chapter 2. In this work, the capability of high pulse-energy amplification near 3 μm from a fluoride fiber was demonstrated by a cascaded amplification of mW-level laser signal at 2.8 μm through Er^{3+}:ZrF_4 and Ho^{3+}:ZrF_4 fibers. The fluoride fiber amplifier in this research delivers 500 ps, 122 μJ pulses at 20 kHz with an average power of 2.45 W, corresponding to a peak power of 245 kW. The pulse energy and output power obtained in this configuration are the record for a 3 μm-class sub-ns fluoride fiber amplifier. The results of this research were published in the prestigious journal "Optics Letters" in June 2018.

A monolithic passively-cooled Er^{3+}:ZrF_4 fluoride fiber laser cavity delivering 41.6 W of continuous output power at 2.824 μm was demonstrated in Chapter 3. The average output power achieved in this research is a record for 3 μm-class fiber lasers. FBGs were written directly in the core of the active fiber which leads to building a splice-less cavity and innovative techniques were used to reduce the thermal load along the active fiber. Moreover, the fiber tip degradation of fluoride fiber under high-power 3 μm laser emission was studied in the last part of this study. According to fiber tip degradation experiments, it was concluded that other materials different from AlF_3- and ZrF_4-based endcaps need to be considered for long-term stability at high output power levels. The results of this research were published in the prestigious journal "Optics Letters" in September 2018.

The problem related to OH radical diffusion occurring at the fiber tips is a limiting factor for long term stability of 3 μm high-power fiber lasers and was investigated in Chapter 3. A couple of solutions for this problem were proposed in Chapter 4. To address fiber tip degradation, several different types of endcaps, either oxide- or non-oxide-based, were fabricated and their long-term performances under the intense 3 μm laser radiation were monitored. Then, endcaps were categorized according to the maximum power handling capacity for long-term operation. Most importantly, a novel method to completely suppress OH diffusion on the fiber tip was proposed in this chapter. This method consists in coating of a Si_3N_4 thin film on the endcap face which enables stable long-term operation of high-power fluoride fiber lasers at 3 μm. The results of this research were published in the prestigious journal "Optics Express" in July 2019.

Future work

The studies and experimental demonstrations in this thesis suggest new directions to pursue for the future. I anticipate that with future optimization of laser systems and components, it may be possible to achieve more powerful systems. In this part of the thesis, additional studies for future work with the scope of improving the performances of high-power fluoride fiber laser sources will be discussed. In the near future, thanks to the further suggestions, mJ-regime pulse energies and hundred-watt regime CW average power near 3 μm with stable long-term operation can be achieved by using simpler laser architectures.

To achieve higher power levels at 3 μm, cascade laser operation at 1.6 and 2.8 μm is a promising solution thanks to high-efficiency and low thermal load along the fiber. Despite exceeding the Stokes limit, the output power was limited to 12.95 W in our work due to temporal instabilities. We believe this might be the result of a saturable absorption process from ground state Er^{3+} ions located in the unpumped end of the fiber which results in giant pulse formation at high pump power. However, it is not certain and needs further investigations. In future investigations, numerical simulations can be performed for better understanding of the problem. In addition, the wavelength of the FBGs in this study was not optimized and investigated clearly, thus optimized FBGs might be a solution for the instability problems. Moreover, an external 1.6 μm laser can be used with 980 nm pump diodes to pump a 2.8 μm fluoride fiber laser cavity and behaviour of the cavity under different pumping conditions can be studied. In this work, the laser cavity was not monolithic and pump power was injected to the laser cavity through butt-coupling. In future work, by writing FBGs at 1.6 μm into the gain fiber core and using the splicing techniques presented in Chapter 4 to achieve silica to fluoride splice can provide a monolithic laser cavity.

The fluoride fiber amplifier presented in Chapter 2 showed the potential of such laser sources for implementing short pulsed laser sources suitable for biomedical applications. There are several drawbacks in the current amplifier such as unmatched cladding size between the first and second amplification stage, high-doping concentration of Ho^{3+}, Pr^{3+}:ZrF_4 fiber, low seed pulse energy. This amplifier system can be simplified by improving the components and replacing the seed laser. First, instead of three-stage amplification, efficient amplification in one stage can be achieved by adopting a proper design. The seed source can be replaced with another one which has a maximum overlapping central wavelength with the active gain spectrum and delivers higher pulse energies. Second, a new active fiber with lower doping concentration and new geometry (i.e. larger clad size) can be used to reduce undesired thermal effects and to improve the laser slope efficiency. In order to investigate optimum fiber properties for achieving more efficient and higher energy pulses, numerical simulations are required to be performed. On the other hand, today, fiber combiners are not commercially available but with the advances in this component in the future, they can be used for pumping active medium instead of free-space injection. Combiners could also allow to build several amplification stages which minimize the

undesired ASE processes. In addition, a fluoride fiber-based oscillator can also be used as a seed source which might enable to build a monolithic amplifier thanks to combiners. Lastly, Al_2O_3 fibers are used for the delivery of 3 μm laser energy in clinical applications so Al_2O_3 fiber endcaps can be spliced at the end of the fiber amplifier by using techniques presented in Chapter 4. Therefore, much simpler and reliable fiber amplifiers can be achieved in this way.

Average output power scalability of fluoride fiber lasers is possible by applying the endcap solutions to laser cavity presented in Chapter 3. In this laser system, the main problem which limits the long-term operation was OH degradation of the fiber tip. This problem can be eliminated by using oxide-based endcaps or endcaps with Si_3N_4 coated thin films as demonstrated in Chapter 4. In addition to this, for an efficient laser transition and lower thermal load on gain fiber, wavelength stabilized diodes near 982 nm can be used as a pump source which leads to much lower undesired ESA. Fiber doping concentration and geometry can also be optimized in order to lower thermal load on fiber and enhance laser slope efficiency. Optimization of fibers might also enable one side pumping instead of pumping from both ends to share pump heat load. For determining properties of the new fiber, numerical simulations are required to be performed. With the advances in fluoride fiber pump combiners in the near future, MOPA configuration can also be considered for further power scaling. Despite its complexity, the MOPA-based architecture can lead to more homogeneous thermal load on active fiber by dividing it into amplification stages. Lastly, an optimized Er^{3+},Pr^{3+}:ZrF_4 fiber can also numerically studied and fabricated instead singly-doped Er^{3+}:ZrF_4 fiber since such medium enable to use medium doping concentration which will help to reduce heat load on fiber.

In Chapter 4, a common problem, fiber tip degradation, was discussed and different endcapping materials were tested under high power 3 μm laser emission. In addition to these, a novel solution was proposed to eliminate this problem. First, undoped YAG crystals and CaF_2 crystals are interesting materials as an endcap but they were not tested due to unavailability. These materials can be fabricated as an endcapping component on a high-power 3 μm fluoride fiber laser output fiber and their performances can be tested. Si_3N_4 coating thin film is a suitable solution for degradation problem; however, it was observed that such coatings show signs of cracking a few months after their deposition upon the fibers. Therefore, optimization of deposition is required for fabricating rugged coatings in the future by investigating optimum thickness range where coatings do not crack over time and preserve their function as an OH diffusion barrier.

Bibliography

[1] T. H. Maiman, "Stimulated optical radiation in ruby," *Nature*, vol. 187, no. 4736, pp. 493–494, 1960.

[2] C. J. Koester and E. Snitzer, "Amplification in a fiber laser," *Applied Optics*, vol. 3, no. 10, pp. 1182–1186, 1964.

[3] S. Poole, D. Payne, and M. Fermann, "Fabrication of low-loss optical fibres containing rare-earth ions," *Electronics Letters*, vol. 21, no. 17, pp. 737–738, 1985.

[4] E. A. Shcherbakov, V. V. Fomin, A. A. Abramov, A. A. Ferin, D. V. Mochalov, and V. P. Gapontsev, "Industrial grade 100 kw power cw fiber laser," in *Advanced Solid-State Lasers Congress*, 2013, p. ATh4A.2.

[5] X. Shen, H. Zhang, and M. Gong, "High energy (100 mJ) and high peak power (8 MW) nanosecond pulses delivered by fiber lasers and self-focusing analysis based on a novel mode decomposition method," *IEEE Journal of Selected Topics in Quantum Electronics*, vol. 24, no. 3, pp. 1–6, 2018.

[6] V. Dominic, S. MacCormack, R. Waarts, S. Sanders, S. Bicknese, R. Dohle, E. Wolak, P. Yeh, and E. Zucker, "110 W fibre laser," *Electronics Letters*, vol. 35, no. 14, pp. 1158–1160, 1999.

[7] M. Brierley and P. France, "Neodymium-doped fluoro-zirconate fibre laser," *Electronics Letters*, vol. 23, no. 16, pp. 815–817, 1987.

[8] M. C. Brierley and P. W. France, "Continuous wave lasing at 2.7 μm in an erbium-doped fluorozirconate fibre," *Electronics Letters*, vol. 24, no. 15, pp. 935–937, 1988.

[9] J. Allain, M. Monerie, and H. Poignant, "Erbium-doped fluorozirconate single-mode fibre lasing at 2.71 μm," *Electronics Letters*, vol. 25, no. 1, pp. 28–29, 1989.

[10] R. Allen, L. Esterowitz, and R. J. Ginther, "Diode-pumped single-mode fluorozirconate fiber laser from the $^4I_{11/2} \rightarrow {}^4I_{13/2}$ transition in erbium," *Applied Physics Letters*, vol. 56, no. 17, pp. 1635–1637, 1990.

[11] L. Wetenkamp, "Efficient CW operation of a 2.9 μm Ho^{3+}-doped fluorozirconate fibre laser pumped at 640 nm," *Electronics Letters*, vol. 26, no. 13, pp. 883–884, 1990.

[12] H. Yanagita, H. Toratani, T. T. Yamashita, and I. Masuda, "2.7-*um* diode-pumped fiber laser," in *SPIE Proc.*, vol. 1581, 1992, pp. 171–180.

[13] J. Schneider, D. Hauschild, C. Frerichs, and L. Wetenkamp, "Highly efficient Er^{3+}:Pr^{3+}-codoped CW fluorozirconate fiber laser operating at 2.7 μm," *International Journal of Infrared and Millimeter Waves*, vol. 15, no. 11, pp. 1907–1922, 1994.

[14] J. Schneider, "Mid-infrared fluoride fiber lasers in multiple cascade operation," *IEEE Photonics Technology Letters*, vol. 7, no. 4, pp. 354–356, 1995.

[15] M. Bunea, W. Lüthy, M. Pollnau, G. Bunea, C. Ghisler, and H. Weber, "Up-conversion cascade laser at 1.7 μm with simultaneous 2.7 μm lasing in erbium ZBLAN fibre," *Electronics Letters*, vol. 31, no. 5, pp. 373–374, 1995.

[16] M. Pollnau, C. Ghisler, G. Bunea, M. Bunea, W. Luthy, and H. P. Weber, "150 mW unsaturated output power at 3 μm from a single-mode-fiber erbium cascade laser," *Applied Physics Letters*, vol. 66, no. 26, pp. 3564–3566, 1995.

[17] M. Pollnau, C. Ghisler, W. Lüthy, H. P. Weber, J. Schneider, and U. B. Unrau, "Three-transition cascade erbium laser at 1.7, 2.7, and 1.6 μm," *Optics Letters*, vol. 22, no. 9, pp. 612–614, 1997.

[18] E. Poppe, B. Srinivasan, and R. Jain, "980 nm diode-pumped continuous wave mid-IR (2.7 μm) fibre laser," *Electronics Letters*, vol. 34, no. 24, pp. 2331–2333, 1998.

[19] T. Sumiyoshi and H. Sekita, "Dual-wavelength continuous-wave cascade oscillation at 3 and 2 μm with a holmium-doped fluoride-glass fiber laser," *Optics Letters*, vol. 23, no. 23, pp. 1837–1839, 1998.

[20] B. Srinivasan, E. Poppe, J. Tafoya, and R. Jain, "High-power (400 mW) diode-pumped 2.7 μm Er:ZBLAN fibre lasers using enhanced Er-Er cross-relaxation processes," *Electronics Letters*, vol. 35, no. 16, pp. 1338–1340, 1999.

[21] T. Sandrock, D. Fischer, P. Glas, M. Leitner, M. Wrage, and A. Diening, "Diode-pumped 1-W Er-doped fluoride glass M-profile fiber laser emitting at 2.8 μm," *Optics Letters*, vol. 24, no. 18, pp. 1284–1286, 1999.

[22] S. D. Jackson, T. A. King, and M. Pollnau, "Diode-pumped 1.7-W erbium 3-μm fiber laser," *Optics Letters*, vol. 24, no. 16, pp. 1133–1135, 1999.

[23] T. Sumiyoshi, H. Sekita, T. Arai, S. Sato, M. Ishihara, and M. Kikuchi, "High-power continuous-wave 3- and 2-μm cascade Ho^{3+}:ZBLAN fiber laser and its medical applications," *IEEE Journal of Selected Topics in Quantum Electronics*, vol. 5, no. 4, pp. 936–943, 1999.

[24] B. Srinivasan, J. Tafoya, and R. Jain, "High-power "watt-level" CW operation of diode-pumped 2.7 μm fiber lasers using efficient cross-relaxation and energy transfer mechanisms," *Optics Express*, vol. 4, no. 12, pp. 490–495, 1999.

[25] S. D. Jackson, "210 mW 2.84 μm Ho^{3+}, Pr^{3+}-doped fluoride fibre laser," *Electronics Letters*, vol. 39, no. 10, pp. 772–773, 2003.

[26] S. D. Jackson, "Continuous wave 2.9 μm dysprosium-doped fluoride fiber laser," *Applied Physics Letters*, vol. 83, no. 7, pp. 1316–1318, 2003.

[27] S. D. Jackson, "Singly Ho^{3+}-doped fluoride fibre laser operating at 2.92 μm," *Electronics Letters*, vol. 40, no. 22, pp. 1400–1401, 2004.

[28] S. D. Jackson, "Single-transverse-mode 2.5-W holmium-doped fluoride fiber laser operating at 2.86 μm," *Optics Letters*, vol. 29, no. 4, pp. 334–336, 2004.

[29] X. Zhu and R. Jain, "5W diode pumped compact mid-IR fiber laser at 2.7 μm," in *IEEE/LEOS*, 2004, p. ThP5.

[30] X. Zhu and R. Jain, "Compact 2 W wavelength-tunable Er:ZBLAN mid-infrared fiber laser," *Optics Letters*, vol. 32, no. 16, pp. 2381–2383, 2007.

[31] X. Zhu and R. Jain, "10-W-level diode-pumped compact 2.78 microm ZBLAN fiber laser." *Optics Letters*, vol. 32, no. 1, pp. 26–28, 2007.

[32] X. Zhu and R. Jain, "Watt-level 100-nm tunable 3-μm fiber laser," *IEEE Photonics Technology Letters*, vol. 20, no. 2, pp. 156–158, 2008.

[33] S. D. Jackson, "High-power and highly efficient diode-cladding-pumped holmium-doped fluoride fiber laser operating at 2.94 μm," *Optics Letters*, vol. 34, no. 15, pp. 2327–2329, 2009.

[34] S. D. Jackson, "High-power erbium cascade fibre laser," *Electronics Letters*, vol. 45, no. 16, pp. 830–832, 2009.

[35] M. Bernier, D. Faucher, N. Caron, and R. Vallée, "Highly stable and efficient erbium-doped 2.8 μm all fiber laser," *Optics Express*, vol. 17, no. 19, pp. 16 941–16 946, 2009.

[36] D. Faucher, M. Bernier, N. Caron, and R. Vallée, "Erbium-doped all-fiber laser at 2.94 μm," *Optics Letters*, vol. 34, no. 21, pp. 3313–3315, 2009.

[37] S. Tokita, M. Murakami, S. Shimizu, M. Hashida, and S. Sakabe, "Liquid-cooled 24 W mid-infrared Er:ZBLAN fiber laser." *Optics Letters*, vol. 34, no. 20, pp. 3062–3064, 2009.

[38] D. Faucher, M. Bernier, G. Androz, N. Caron, and R. Vallée, "20 W passively cooled single-mode all-fiber laser at 2.8 μm." *Optics Letters*, vol. 36, no. 7, pp. 1104–1106, 2011.

[39] J. Li, D. D. Hudson, and S. D. Jackson, "High-power diode-pumped fiber laser operating at 3 μm," *Optics Letters*, vol. 36, no. 18, pp. 3642–3644, 2011.

[40] D. Hudson, E. Magi, L. Gomes, and S. Jackson, "1 W diode-pumped tunable Ho^{3+}, Pr^{3+}-doped fluoride glass fibre laser," *Electronics Letters*, vol. 47, no. 17, pp. 985–986, 2011.

[41] S. D. Jackson, M. Pollnau, and Jianfeng Li, "Diode pumped erbium cascade fiber lasers," *IEEE Journal of Quantum Electronics*, vol. 47, no. 4, pp. 471–478, 2011.

[42] V. Fortin, M. Bernier, N. Caron, D. Faucher, M. El Amraoui, Y. Messaddeq, and R. Vallée, "Towards the development of fiber lasers for the 2 to 4 μm spectral region," *Optical Engineering*, vol. 52, no. 5, p. 054202, 2013.

[43] S. Crawford, D. D. Hudson, and S. Jackson, "3.4 W Ho^{3+}, Pr^{3+} Co-doped fluoride fibre laser," in *Conference on Lasers and Electro-Optics*, 2014, p. STu1L.3.

[44] V. Fortin, M. Bernier, S. T. Bah, and R. Vallée, "30 W fluoride glass all-fiber laser at 2.94 μm," *Optics Letters*, vol. 40, no. 12, pp. 2882–2885, 2015.

[45] J. Li, L. Wang, H. Luo, J. Xie, and Y. Liu, "High power cascaded erbium doped fluoride fiber laser at room temperature," *IEEE Photonics Technology Letters*, vol. 28, no. 6, pp. 673–676, 2016.

[46] M. Majewski and S. D. Jackson, "Highly efficient mid-infrared dysprosium fiber laser," *Optics Letters*, vol. 41, no. 10, pp. 2173–2176, 2016.

[47] Y. O. Aydin, V. Fortin, F. Maes, F. Jobin, S. D. Jackson, R. Vallée, and M. Bernier, "Diode-pumped mid-infrared fiber laser with 50 % slope efficiency," *Optica*, vol. 4, no. 2, pp. 6–9, 2017.

[48] L. Sojka, L. Pajewski, M. Popenda, E. Beres-Pawlik, S. Lamrini, K. Markowski, T. Osuch, T. M. Benson, A. B. Seddon, and S. Sujecki, "Experimental investigation of mid-infrared laser actionfrom Dy^{3+} doped fluorozirconate fiber," *IEEE Photonics Technology Letters*, vol. 30, no. 12, pp. 1083–1086, 2018.

[49] R. I. Woodward, M. R. Majewski, G. Bharathan, D. D. Hudson, A. Fuerbach, and S. D. Jackson, "Watt-level dysprosium fiber laser at 3.15 μm with 73% slope efficiency," *Optics Letters*, vol. 43, no. 7, pp. 1471–1474, 2018.

[50] Y. O. Aydin, V. Fortin, R. Vallée, and M. Bernier, "Towards power scaling of 2.8 μm fiber lasers," *Optics Letters*, vol. 43, no. 18, pp. 4542–4545, 2018.

[51] V. Fortin, F. Jobin, M. Larose, M. Bernier, and R. Vallée, "10-W-level monolithic dysprosium-doped fiber laser at 3.24 μm," *Optics Letters*, vol. 44, no. 3, p. 491, 2019.

[52] S. Jackson, T. King, and M. Pollnau, "Efficient high power operation of erbium 3 μm fibre laser diode-pumped at 975 nm," *Electronics Letters*, vol. 36, no. 3, pp. 223–224, 2000.

[53] C. Frerichs and T. Tauermann, "Q-switched operation of laser diode pumped erbium-doped fluorozirconate fibre laser operating at 2.7 μm," *Electronics Letters*, vol. 30, no. 9, pp. 706–707, 1994.

[54] J. M. Teichman, K. F. Chan, P. P. Cecconi, N. S. Corbin, A. D. Kamerer, R. D. Glickman, and A. J. Welch, "Erbium:YAG versus holmium:YAG lithotripsy," *Journal of Urology*, vol. 165, no. 3, pp. 876–879, 2001.

[55] C. Bader and I. Krejci, "Indications and limitations of Er:YAG laser applications in dentistry," *American Journal of Dentistry*, vol. 19, no. 3, pp. 178–186, 2006.

[56] C. C. Neubaur and G. Stevens, "Erbium:YAG laser cataract removal: Role of fiber-optic delivery system," *Journal of Cataract & Refractive Surgery*, vol. 25, no. 4, pp. 514–520, 1999.

[57] C. K. Chen, N. J. Chang, J. H. Ke, E. Fu, and W. H. Lan, "Er:YAG laser application for removal of keratosis using topical anesthesia," *Journal of Dental Sciences*, vol. 8, no. 2, pp. 196–199, 2013.

[58] D. G. Pandurić, I. Bago, D. Katanec, J. Žabkar, I. Miletić, and I. Anić, "Comparison of Er:YAG laser and surgical drill for osteotomy in oral surgery: an experimental study," *Journal of Oral and Maxillofacial Surgery*, vol. 70, no. 11, pp. 2515–2521, 2012.

[59] Z. Li, L. Reinisch, and W. P. Van de Merwe, "Bone ablation with Er:YAG and CO_2 laser: Study of thermal and acoustic effects," *Lasers in Surgery and Medicine*, vol. 12, no. 1, pp. 79–85, 1992.

[60] G. Teikemier and D. J. Goldberg, "Skin resurfacing with the erbium:YAG laser," *Dermatologic Surgery*, vol. 23, no. 8, pp. 685–687, 1997.

[61] R. F. Bonner, L. G. Prevosti, M. B. Leon, K. Levin, and D. Tran, "New source for laser angioplasty: Er:YAG laser pulses transmitted through zirconium fluoride optical fiber catheters," in *SPIE Proc.*, vol. 0906, 1988, pp. 288–293.

[62] M. H. Niemz, "Interaction Mechanism," in *Laser-Tissue Interactions*, E. Greenbaum and O. Ridge, Eds. Springer Berlin Heidelberg, 2007, pp. 45–150.

[63] H. Jelínková, "Introduction: the history of lasers in medicine," in *Lasers for Medical Applications*, H. Jelínková, Ed. Woodhead Publishing, 2013, pp. 1 – 13.

[64] S. J. Linke, A. Frings, L. Ren, A. Gomolka, U. Schumacher, R. Reimer, N. O. Hansen, N. Jowett, G. Richard, and R. J. Miller, "A new technology for applanation free corneal trephination: The picosecond infrared laser (PIRL)," *PLoS ONE*, vol. 10, no. 3, pp. 1–12, 2015.

[65] H. Petersen, A. Gliese, Y. Stober, S. Maier, N.-O. Hansen, S. Kruber, D. Eggert, M. Tóth, T. Gosau, H. Schlüter, K. Püschel, U. Schumacher, R. J. D. Miller, A. Münscher, and C. Dalchow, "Picosecond Infrared Laser (PIRL) Application in stapes surgery—first experience in human temporal bones," *Otology & Neurotology*, vol. 39, no. 4, pp. e224–e230, 2018.

[66] M. Kwiatkowski, M. Wurlitzer, A. Krutilin, P. Kiani, R. Nimer, M. Omidi, A. Mannaa, T. Bussmann, K. Bartkowiak, S. Kruber, S. Uschold, P. Steffen, J. Lübberstedt, N. Küpker, H. Petersen, R. Knecht, N. Hansen, A. Zarrine-Afsar, W. Robertson, R. Miller, and H. Schlüter, "Homogenization of tissues via picosecond-infrared laser (PIRL) ablation: Giving a closer view on the in-vivo composition of protein species as compared to mechanical homogenization," *Journal of Proteomics*, vol. 134, pp. 193–202, 2016.

[67] HITRAN online. hitran.org/, accessed 2019-02-27.

[68] M. C. Pierce, S. D. Jackson, M. R. Dickinson, T. A. King, and P. Sloan, "Laser-tissue interaction with a continuous wave 3-μm fibre laser: Preliminary studies with soft tissue," *Lasers in Surgery and Medicine*, vol. 26, no. 5, pp. 491–495, 2000.

[69] T. Arai, T. Sumiyoshi, K. Naruse, M. Ishihara, S. Sato, M. Kikuchi, T. Kasamatsu, H. Sekita, and M. Obara, "Laser-tissue interaction of a continuous-wave 2-μm, 3-μm cascade oscillation fiber laser: sharp incision with controlled coagulation layer thickness," in *SPIE Proc.*, vol. 3914, 2000, pp. 252–259.

[70] M. R. Majewski, R. I. Woodward, and S. D. Jackson, "Dysprosium-doped ZBLAN fiber laser tunable from 2.8 μm to 3.4 μm, pumped at 1.7 μm," *Optics Letters*, vol. 43, no. 5, pp. 971–974, 2018.

[71] R. I. Woodward, M. R. Majewski, D. D. Hudson, and S. D. Jackson, "Swept-wavelength mid-infrared fiber laser for real-time ammonia gas sensing," *APL Photonics*, vol. 4, no. 2, p. 020801, 2019.

[72] W. Yang, B. Zhang, K. Yin, X. Zhou, and J. Hou, "High power all fiber mid-IR supercontinuum generation in a ZBLAN fiber pumped by a 2 μm MOPA system," *Optics Express*, vol. 21, no. 17, pp. 19 732–19 742, 2013.

[73] J. Swiderski and M. Michalska, "High-power supercontinuum generation in a ZBLAN fiber with very efficient power distribution toward the mid-infrared," *Optics Letters*, vol. 39, no. 4, pp. 910–913, 2014.

[74] J.-C. Gauthier, V. Fortin, S. Duval, R. Vallée, and M. Bernier, "In-amplifier mid-infrared supercontinuum generation," *Optics Letters*, vol. 40, no. 22, pp. 5247–5250, 2015.

[75] J.-C. Gauthier, V. Fortin, J.-Y. Carrée, S. Poulain, M. Poulain, R. Vallée, and M. Bernier, "Mid-ir supercontinuum from 2.4 to 5.4 μm in a low-loss fluoroindate fiber," *Optics Letters*, vol. 41, no. 8, pp. 1756–1759, 2016.

[76] S. Duval, M. Bernier, V. Fortin, J. Genest, M. Piché, and R. Vallée, "Femtosecond fiber lasers reach the mid-infrared," *Optica*, vol. 2, no. 7, pp. 623–626, 2015.

[77] R. I. Woodward, M. R. Majewski, and S. D. Jackson, "Mode-locked dysprosium fiber laser: picosecond pulse generation from 2.97 to 3.30 μm," *APL Photonics*, vol. 3, no. 11, p. 116106, 2018.

[78] S. P. Mahulikar, H. R. Sonawane, and G. Arvind Rao, "Infrared signature studies of aerospace vehicles," *Progress in Aerospace Sciences*, vol. 43, no. 7-8, pp. 218–245, 2007.

[79] I. Elder, "Performance requirements for countermeasures lasers," in *SPIE Proc.*, vol. 7836, 2010, p. 783605.

[80] H. H. P. T. Bekman, J. C. van den Heuvel, F. J. M. van Putten, and R. Schleijpen, "Development of a mid-infrared laser for study of infrared countermeasures techniques," in *SPIE Proc.*, vol. 5615, 2004, pp. 27–38.

[81] M. Bernier, D. Faucher, R. Vallée, A. Saliminia, G. Androz, Y. Sheng, and S. L. Chin, "Bragg gratings photoinduced in ZBLAN fibers by femtosecond pulses at 800 nm," *Optics Letters*, vol. 32, no. 5, pp. 454–456, 2007.

[82] M. Poulain, M. Poulain, J. Lucas, and P. Brun, "Verres fluorés au tétrafluorure de zirconium: propriétés optiques d'un verre dopé au Nd^{3+}," *Materials Research Bulletin*, vol. 10, no. 4, pp. 243–246, 1975.

[83] K. Ohsawa, T. Shibata, K. Nakamura, and S. Yoshida, "Fluorozirconate glasses for infrared transmitting optical fiber," in *Proc. of ECOC*, vol. 7, 1981.

[84] S. Cozic, S. Poulain, and M. Poulain, "Low loss fluoride optical fibers: fabrication and applications," in *Advanced Photonics Congress (BGPP, IPR)*, 2018, p. SoM2H.3.

[85] S. Shibata, M. Horiguchi, K. Jinguji, S. Mitachi, T. Kanamori, and T. Manabe, "Prediction of loss minima in infra-red optical fibres," *Electronics Letters*, vol. 17, no. 21, pp. 775–777, 1981.

[86] M. Poulain, N. Gougeon, and G. Mazé, "Mechanical properties of fluoride glass fibers," in *SPIE Proc.*, vol. 4940, 2003, pp. 30–46.

[87] C. R. Kurkjian, D. R. Biswas, and H. H. Yuce, "Intrinsic strength of light guide fibers," in *SPIE Proc.*, vol. 2611, 1996, pp. 56–63.

[88] M. Saad, "Indium fluoride glass fibers," in *SPIE Proc.*, vol. 8275, 2012, p. 82750D.

[89] J. A. Harrington, "Mid-IR and Infrared Fibers," in *Specialty Optical Fibers Handbook*, A. Mendez and T. Morse, Eds. Elsevier BV, 2007, pp. 429–452.

[90] B. Srinivasan, M. Erlandsson, G. Feller, E. Mies, and R. Jain, "Reproducible fusion splicing of low melting point (fluoride) optical fibers with the use of a stable heat source," in *Proc. Opt. Fiber Commun. Conf*, 1997, pp. 1–2.

[91] M. Saad, "High purity fluoride glass synthesis: a review," in *SPIE Proc*, vol. 7228, 2009, p. 72280G.

[92] FiberLabs Inc. www.fiberlabs.com, last visited on 24/03/2019.

[93] Le Verre Fluore Infrared Solutions. www.leverrefluore.com, last visited on 24/03/2019.

[94] J. Colaizzi, M. J. Matthewson, T. Iqbal, and M. R. Shahriari, "Mechanical Properties of Aluminum Fluoride Glass Fibers," in *SPIE Proc.*, vol. 1591, 1991, pp. 26–33.

[95] J. Colaizzi and M. Matthewson, "Mechanical durability of ZBLAN and aluminum fluoride-based optical fiber," *Journal of Lightwave Technology*, vol. 12, no. 8, pp. 1317–1324, 1994.

[96] M. R. Majewski, R. I. Woodward, J.-Y. Carrée, S. Poulain, M. Poulain, and S. D. Jackson, "Emission beyond 4 μm and mid-infrared lasing in a dysprosium-doped indium fluoride (InF_3) fiber," *Optics Letters*, vol. 43, no. 8, pp. 1926–1929, 2018.

[97] R. Doremus, N. Bansal, T. Bradner, and D. Murphy, "Zirconium fluoride glass : surface crystals formed by reaction with water," *Journal of Materials Science Letters*, vol. 3, pp. 484–488, 1984.

[98] R. H. Doremus, D. Murphy, and N. P. Bansal, "Reaction of zirconium fluoride glass with water : kinetics of dissolution," *Journal of Materials Science*, vol. 20, pp. 4445–4453, 1985.

[99] H. Poignant, S. Boj, E. Delevaque, M. Monerie, T. Taunay, P. Niay, P.Bernage, and W. Xie, "Efficiency and thermal behaviour of cerium- doped fluorozirconate glass fibre Bragg gratings," *Electronics Letters*, vol. 30, no. 16, pp. 1339–1341, 1994.

[100] T. Taunay, P. Niay, P. Bernage, and E. X. Xie, "Ultraviolet-induced permanent Bragg gratings in cerium-doped ZBLAN glasses or optical fibers," *Optics Letters*, vol. 19, no. 17, pp. 1269–1271, 1994.

[101] K. M. Davis, K. Miura, N. Sugimoto, and K. Hirao, "Writing waveguides in glass with a femtosecond laser," *Optics Letters*, vol. 21, no. 21, pp. 1729–1731, 1996.

[102] K. Miura, J. Qiu, T. Mitsuyu, and K. Hirao, "Preparation and optical properties of fluoride glass waveguides induced by laser pulses," *Journal of Non-Crystalline Solids*, vol. 256, pp. 212–219, 1999.

[103] D. Grobnic, S. J. Mihailov, and C. W. Smelser, "Femtosecond IR Laser Inscription of Bragg Gratings in Single- and Multimode Fluoride Fibers," *IEEE Photonics Technology Letters*, vol. 18, no. 24, pp. 2686–2688, 2006.

[104] G. Androz, M. Bernier, D. Faucher, and R. Vallée, "2.3 W single transverse mode thulium-doped ZBLAN fiber laser at 1480 nm," *Optics Express*, vol. 16, no. 20, pp. 16 019–16 031, 2009.

[105] D. D. Hudson, R. J. Williams, M. J. Withford, and S. D. Jackson, "Single-frequency fiber laser operating at 2.9 μm," *Optics Letters*, vol. 38, no. 14, pp. 2388–2390, 2013.

[106] M. Bernier, F. Trépanier, J. Carrier, and R. Vallée, "High mechanical strength fiber Bragg gratings made with infrared femtosecond pulses and a phase mask," *Optics Letters*, vol. 39, no. 12, pp. 3646–3649, 2014.

[107] L.-P. Pleau, P. Paradis, J.-S. Frenière, M. Huneault, S. Gouin, S. M. Aljamimi, Y. O. Aydin, S. Duval, J.-C. Gauthier, J. Habel, F. Jobin, F. Maes, L.-R. Robichaud, N. Grégoire, S. Morency, and M. Bernier, "20 W splice-free erbium-doped all-fiber laser operating at 1610 nm," *Optics Express*, vol. 26, no. 17, pp. 22 378–22 388, 2018.

[108] Y. O. Aydin, V. Fortin, R. Vallée, and M. Bernier, "High power splice-less fiber laser at 2825 nm," in *Conference on Lasers and Electro-Optics*, 2018, p. STh4K.2.

[109] P. Paradis, V. Fortin, Y. O. Aydin, R. Vallée, and M. Bernier, "10 W-level gain-switched all-fiber laser at 2.8 μm," *Optics Letters*, vol. 43, no. 13, pp. 3196–3199, 2018.

[110] G. Bharathan, R. I. Woodward, M. Ams, D. D. Hudson, S. D. Jackson, and A. Fuerbach, "Direct inscription of Bragg gratings into coated fluoride fibers for widely tunable and robust mid-infrared lasers," *Optics Express*, vol. 25, no. 24, pp. 2388–2390, 2017.

[111] K. Goya, H. Matsukuma, H. Uehara, S. Hattori, C. Schäfer, D. Konishi, M. Murakami, and S. Tokita, "Plane-by-plane femtosecond laser inscription of first-order fiber Bragg gratings in fluoride glass fiber for in situ monitoring of lasing evolution," *Optics Express*, vol. 26, no. 25, pp. 33 305–33 313, 2018.

[112] G. Bharathan, R. I. Woodward, D. D. Hudson, S. D. Jackson, and A. Fuerbach, "In-fiber polarizer based on a 45-degree tilted fluoride fiber Bragg grating for mid-infrared fiber laser technology," *OSA Continuum*, vol. 1, no. 1, pp. 56–63, 2018.

[113] M. Kondow, T. Kitatani, K. Nakahara, and T. Tanaka, "Temperature dependence of lasing wavelength in a GaInNAs laser diode," *IEEE Photonics Technology Letters*, vol. 12, no. 7, pp. 777–779, 2000.

[114] J. Li and S. D. Jackson, "Numerical modeling and optimization of diode Pumped heavily-erbium-doped fluoride fiber lasers," *IEEE Journal of Quantum Electronics*, vol. 48, no. 4, pp. 454–464, 2012.

[115] D. V. Talavera and E. B. Mejia, "Holmium-doped fluoride fiber laser at 2950 nm pumped at 1175 nm," *Laser Physics*, vol. 16, no. 3, pp. 436–440, 2006.

[116] R. Al-Mahrous, R. Caspary, and W. Kowalsky, "A thermal splicing method to join silica and fluoride fibers," *Journal of Lightwave Technology*, vol. 32, no. 2, pp. 303–308, 2014.

[117] D. L. Bisbee, "Splicing silica fibers with an electric arc," *Applied Optics*, vol. 15, no. 3, pp. 796–798, 1976.

[118] L. Rivoallan and J. Guilloux, "Fusion splicing of fluoride glass optical fibre with CO_2 laser," *Electronics Letters*, vol. 24, no. 12, pp. 756–757, 1988.

[119] R. Carbonnier and W. Zheng, "New approach for high reliability, low loss splicing between silica and ZBLAN fibers," in *SPIE Proc.*, vol. 10513, 2018, p. 105131G.

[120] G. E. Miller, "Method and apparatus for cutting optical fibers," U.S. Patent 4 203 539, 1980.

[121] J. Shibin and J. Wang, "Method of fusion splicing silica fiber with low-temperature multi-component glass fiber," U.S. Patent 6 705 771, 2004.

[122] L. Pei, X. Dong, Q. C. Zhao, Ruifeng, R. Caspary, M. S. K. Kien, and S. Jian, "Low loss splicing method to join silica and fluoride fibers," in *SPIE Proc.*, vol. 6781, 2007, p. 67814O.

[123] H. Okamoto, K. Kasuga, and Y. Kubota, "Efficient 521 nm all-fiber laser: splicing Pr^{3+}-doped ZBLAN fiber to end-coated silica fiber," *Optics Letters*, vol. 36, no. 8, pp. 1470–1472, 2011.

[124] J. Yu, C.-Y. Guo, Z.-J. Zheng, D.-Q. Ouyang, J.-Q. Zhao, J.-Z. Wang, and S.-C. Ruan, "An effective thermal splicing method to join fluoride and silica fibers for a high power regime," *Chinese Physics Letters*, vol. 32, no. 11, p. 114206, 2015.

[125] T. Huang, Q. He, X. She, X. Shu, and C. Liu, "Study on thermal splicing of ZBLAN fiber to silica fiber," *Optical Engineering*, vol. 55, no. 10, p. 106119, 2016.

[126] Y. O. Aydin, F. Maes, V. Fortin, S. T. Bah, R. Vallée, and M. Bernier, "Endcapping of high-power 3 μm fiber lasers," *Opt. Express*, vol. 27, no. 15, pp. 20 659–20 669, 2019.

[127] N. Caron, M. Bernier, D. Faucher, and R. Vallée, "Understanding the fiber tip thermal runaway present in 3 μm fluoride glass fiber lasers," *Optics Express*, vol. 20, no. 20, pp. 22 188–22 194, 2012.

[128] G. Frischat, B. Hueber, and B. Ramdohr, "Chemical stability of ZrF_4- and AlF_3-based heavy metal fluoride glasses in water," *Journal of Non-Crystalline Solids*, vol. 284, no. 1-3, pp. 105–109, 2001.

[129] M. Messner, A. Heinrich, C. Hagen, and K. Unterrainer, "High brightness diode pumped Er:YAG laser system at 2.94 μm with nearly 1kW peak power," in *SPIE Proc.*, vol. 9726, 2016, pp. 972 602–1.

[130] Faraday Photonics. www.faradayphotonics.com, last visited on 2019-03-24.

[131] C. A. Schäfer, H. Uehara, D. Konishi, S. Hattori, H. Matsukuma, M. Murakami, S. Shimizu, and S. Tokita, "Fluoride-fiber-based side-pump coupler for high-power fiber lasers at 2.8 μm," *Optics Letters*, vol. 43, no. 10, pp. 2340–2343, 2018.

[132] G. Stevens and T. Woodbridge, "Mid-IR fused fiber couplers," in *SPIE Proc.*, vol. 9730, 2016, p. 973007.

[133] N. Bawden, H. Matsukuma, O. Henderson-Sapir, E. Klantsataya, S. Tokita, and D. J. Ottaway, "Actively Q-switched dual-wavelength pumped Er^{3+}:ZBLAN fiber laser at 3.47 μm," *Optics Letters*, vol. 43, no. 11, pp. 2724–2727, 2018.

[134] Y. O. Aydin, V. Fortin, F. Maes, F. Jobin, S. D. Jackson, R. Vallée, and M. Bernier, "Diode-pumped mid-infrared fiber laser with 50 % slope efficiency," *Optica*, vol. 4, no. 2, pp. 6–9, 2017.

[135] P. Golding, S. Jackson, T. King, and M. Pollnau, "Energy transfer processes in Er^{3+}-doped and Er^{3+},Pr^{3+}-codoped ZBLAN glasses," *Physical Review B*, vol. 62, no. 2, pp. 856–864, 2000.

[136] M. Gorjan, R. Petkovšek, M. Marinček, and M. Čopič, "High-power pulsed diode-pumped Er:ZBLAN fiber laser," *Optics Letters*, vol. 36, no. 10, pp. 1923–1925, 2011.

[137] S. Tokita, M. Murakami, S. Shimizu, M. Hashida, and S. Sakabe, "12 W Q-switched Er:ZBLAN fiber laser at 2.8 μm," *Optics Letters*, vol. 36, no. 15, pp. 2812–2814, 2011.

[138] P. Paradis, V. Fortin, Y. O. Aydin, F. Jobin, S. Duval, R. Vallée, and M. Bernier, "All-fiber gain-switched laser at 2.8 microns," in *Laser Congress 2017 (ASSL, LAC)*, vol. 2017. OSA, 2017, p. ATh4A.5.

[139] P. Wan, L.-M. Yang, S. Bai, and J. Liu, "High energy 3 μm ultrafast pulsed fiber laser," *Optics Express*, vol. 23, no. 7, pp. 9527–9532, 2015.

[140] H. Luo, J. Li, J. Xie, B. Zhai, C. Wei, and Y. Liu, "High average power and energy microsecond pulse generation from an erbium-doped fluoride fiber MOPA system," *Optics Express*, vol. 24, no. 25, pp. 29 022–29 032, 2016.

[141] M. Pollnau and S. D. Jackson, "Energy recycling versus lifetime quenching in erbium-doped 3 μm fiber lasers," *IEEE Journal of Quantum Electronics*, vol. 38, no. 2, pp. 162–169, 2002.

[142] R. S. Quimby, W. J. Miniscalco, and B. A. Thompson, "Excited-state absorption at 980 nm in erbium-doped glass," in *SPIE Proc.*, vol. 1581, 1992, pp. 72–79.

[143] J. Li, H. Luo, Y. Liu, L. Zhang, and S. D. Jackson, "Modeling and optimization of cascaded erbium and holmium doped fluoride fiber lasers," *IEEE Journal of Selected Topics in Quantum Electronics*, vol. 20, no. 5, pp. 15–28, 2014.

[144] D. J. Coleman, T. A. King, D.-K. Ko, and J. Lee, "Q-switched operation of a 2.7 μm cladding-pumped Er^{3+}/Pr^{3+} codoped ZBLAN fibre laser," *Optics Communications*, vol. 236, no. 4-6, pp. 379–385, 2004.

[145] M. Gorjan, M. Marinček, and M. Čopič, "Role of interionic processes in the efficiency and operation of erbium-doped fluoride fiber lasers," *IEEE Journal of Quantum Electronics*, vol. 47, no. 2, pp. 262–273, 2011.

[146] J. Li, L. Gomes, and S. D. Jackson, "Numerical modeling of holmium-doped fluoride fiber lasers," *IEEE Journal of Quantum Electronics*, vol. 48, no. 5, pp. 596–607, 2012.

[147] T. Hu, D. D. Hudson, and S. D. Jackson, "Actively Q-switched 2.9 μm Ho^{3+},Pr^{3+}-doped fluoride fiber laser," *Optics Letters*, vol. 37, no. 11, p. 2145, 2012.

[148] J. Li, Y. Yang, D. D. Hudson, Y. Liu, and S. D. Jackson, "A tunable Q -switched Ho^{3+}-doped fluoride fiber laser," *Laser Physics Letters*, vol. 10, no. 4, p. 045107, 2013.

[149] S. Jackson, D. Hudson, and T. Hu, "High peak power actively Q-switched Ho^{3+}, Pr^{3+}-co-doped fluoride fibre laser," *Electronics Letters*, vol. 49, no. 12, pp. 766–767, 2013.

[150] Y. O. Aydın, V. Fortin, D. Kraemer, A. Fraser, R. Vallée, and M. Bernier, "High-energy picosecond pulses from a 2850 nm fiber amplifier," *Optics Letters*, vol. 43, no. 12, pp. 2748–2751, 2018.

[151] B. M. Antipenko, A. L. Ashkalunin, A. A. Mak, B. V. Sinitsyn, Y. V. Tomashevich, and G. S. Shakhkalamyan, "Three-micron laser action in Dy^{3+}," *Soviet Journal of Quantum Electronics*, vol. 10, no. 5, pp. 560–563, 1980.

[152] Y. H. Tsang, A. E. El-Taher, T. A. King, and S. D. Jackson, "Efficient 2.96 μm dysprosium-doped fluoride fibre laser pumped with a Nd:YAG laser operating at 1.3 μm," *Optics Express*, vol. 14, no. 2, pp. 678–685, 2006.

[153] M. R. Majewski and S. D. Jackson, "Tunable dysprosium laser," *Optics Letters*, vol. 41, no. 19, pp. 4496–4498, 2016.

[154] P. Tang, Z. Qin, J. Liu, C. Zhao, G. Xie, S. Wen, and L. Qian, "Watt-level passively mode-locked Er^{3+}-doped ZBLAN fiber laser at 2.8 μm," *Optics Letters*, vol. 40, no. 21, p. 4855, 2015.

[155] D. Ristau, *Laser-Induced Damage in Optical Materials*, 1st ed. CRC Press, 2015.

[156] S. Duval, J.-C. Gauthier, L.-R. Robichaud, P. Paradis, M. Olivier, V. Fortin, M. Bernier, M. Piché, and R. Vallée, "Watt-level fiber-based femtosecond laser source tunable from 2.8 to 3.6 μm," *Optics Letters*, vol. 41, no. 22, pp. 5294–5297, 2016.

[157] M. Michalska, P. Hlubina, and J. Swiderski, "Mid-infrared supercontinuum generation to $\sim$4.7 μm in a ZBLAN fiber pumped by an optical parametric generator," *IEEE Photonics Journal*, vol. 9, no. 2, pp. 1–7, 2017.

[158] K. Liu, J. Liu, H. Shi, F. Tan, and P. Wang, "High power mid-infrared supercontinuum generation in a single-mode ZBLAN fiber with up to 21.8 W average output power," *Opt. Express*, vol. 22, no. 20, pp. 24 384–24 391, 2014.

[159] F. K. Tittel, D. Richter, and A. Fried, "Mid-Infrared Laser Applications in Spectroscopy," in *Solid-State Mid-Infrared Laser Sources*, I. T. Sorokina and K. Vodopyanov, Eds. Springer Berlin Heidelberg, 2003, pp. 458–529.

[160] M. C. Pierce, S. D. Jackson, M. R. Dickinson, T. A. King, and P. Sloan, "Laser-tissue interaction with a continuous wave 3 μm fibre laser: preliminary studies with soft tissue," *Lasers in Surgery and Medicine*, vol. 26, no. 5, pp. 491–495, 2000.

[161] D. J. Richardson, J. Nilsson, and W. A. Clarkson, "High power fiber lasers: current status and future perspectives [Invited]," *Journal of the Optical Society of America B*, vol. 27, no. 11, p. B63, 2010.

[162] V. Fortin, F. Maes, M. Bernier, S. T. Bah, M. D'Auteuil, and R. Vallée, "Watt-level erbium-doped all-fiber laser at 3.44 μm," *Optics Letters*, vol. 41, no. 3, pp. 559–562, 2016.

[163] S. Colin, E. Contesse, P. L. Boudec, G. Stephan, and F. Sanchez, "Evidence of a saturable-absorption effect in heavily erbium-doped fibers." *Optics Letters*, vol. 21, no. 24, pp. 1987–1989, 1996.

[164] Y. D. Huang, M. Mortier, and F. Auzel, "Stark level analysis for Er^{3+}-doped ZBLAN glass," *Optical Materials*, vol. 17, pp. 501–511, 2001.

[165] J. Koetke and G. Huber, "Infrared excited-state absorption and stimulated-emission cross sections of Er^{3+}-doped crystals," *Applied Physics B*, vol. 61, no. 2, pp. 151–158, 1995.

[166] S. D. Jackson, "Towards high-power mid-infrared emission from a fibre laser," *Nature Photonics*, vol. 6, no. 7, pp. 423–431, 2012.

[167] O. Henderson-Sapir, S. D. Jackson, and D. J. Ottaway, "Versatile and widely tunable mid-infrared erbium doped ZBLAN fiber laser," *Optics Letters*, vol. 41, no. 7, pp. 1676–1679, 2016.

[168] Optiwave Inc. http://www.optiwave.com, accessed 2019-02-27.

[169] K. Franjic, M. L. Cowan, D. Kraemer, and R. J. D. Miller, "Laser selective cutting of biological tissues by impulsive heat deposition through ultrafast vibrational excitations," *Optics Express*, vol. 17, no. 25, pp. 22 937–22 959, 2009.

[170] S. Amini-Nik, D. Kraemer, M. L. Cowan, K. Gunaratne, P. Nadesan, B. A. Alman, and R. J. Dwayne Miller, "Ultrafast mid-IR laser scalpel: Protein signals of the fundamental limits to minimally invasive surgery," *PLoS ONE*, vol. 5, no. 9, p. e13053, 2010.

[171] M. Hess, M. D. Hildebrandt, F. Müller, S. Kruber, P. Kroetz, U. Schumacher, R. Reimer, M. Kammal, K. Püschel, W. Wöllmer, and D. Miller, "Picosecond infrared laser (PIRL): an ideal phonomicrosurgical laser?" *European Archives of Oto-Rhino-Laryngology*, vol. 270, no. 11, pp. 2927–2937, 2013.

[172] M. Skorczakowski, J. Swiderski, W. Pichola, P. Nyga, A. Zajac, M. Maciejewska, L. Galecki, J. Kasprzak, S. Gross, A. Heinrich, and T. Bragagna, "Mid-infrared Q-switched Er:YAG laser for medical applications," *Laser Physics Letters*, vol. 7, no. 7, pp. 498–504, 2010.

[173] J. T. Walsh, T. J. Flotte, and T. F. Deutsch, "Er:YAG laser ablation of tissue: Effect of pulse duration and tissue type on thermal damage," *Lasers in Surgery and Medicine*, vol. 9, no. 4, pp. 314–326, 1989.

[174] I. Moskalev, S. Mirov, M. Mirov, S. Vasilyev, V. Smolski, A. Zakrevskiy, and V. Gapontsev, "140 W Cr:ZnSe laser system," *Optics Express*, vol. 24, no. 18, pp. 21 090–21 104, 2016.

[175] V. Fortin, M. Bernier, S. T. Bah, and R. Vallée, "30 W fluoride glass all-fiber laser at 2.94 μm," *Opt. Lett.*, vol. 40, no. 12, pp. 2882–2885, 2015.

[176] K. Tanimura, M. D. Shinn, W. A. Sibley, M. G. Drexhage, and R. N. Brown, "Optical transitions of Ho^{3+} ions in fluorozirconate glass," *Physical Review B*, vol. 30, no. 5, pp. 2429–2437, 1984.

[177] S. D. Jackson, F. Bugge, and G. Erbert, "Directly diode-pumped holmium fiber lasers," *Optics Letters*, vol. 32, no. 17, pp. 2496–2498, 2007.

[178] J. Li, D. D. Hudson, Y. Liu, and S. D. Jackson, "Efficient 2.87 μm fiber laser passively switched using a semiconductor saturable absorber mirror," *Optics Letters*, vol. 37, no. 18, pp. 3747–3749, 2012.

[179] M. Murakami, S. Hattori, C. Schaefer, and K. Yahata, "Laser processing technology with mid-infrared Er fiber laser," *Proceedings of the 83rd Laser Materials Processing Conference*, p. 117, 2015.

[180] M. R. Dickinson, A. Charlton, T. A. King, A. J. Freemont, and R. Bramley, "Studies of Er-YAG laser interactions with soft tissue," *Lasers in Medical Science*, vol. 6, no. 2, pp. 125–131, 1991.

[181] S. Tokita, M. Hirokane, M. Murakami, S. Shimizu, M. Hashida, and S. Sakabe, "Stable 10 W Er:ZBLAN fiber laser operating at 2.71-2.88 μm," *Optics Letters*, vol. 35, no. 23, pp. 3943–3945, 2010.

[182] D. Faucher, M. Bernier, N. Caron, and R. Vallée, "Erbium-doped all-fiber laser at 2.94 μm," *Optics Letters*, vol. 34, no. 21, pp. 3313–3315, 2009.

[183] M. Bernier, F. Trépanier, J. Carrier, and R. Vallée, "High mechanical strength fiber Bragg gratings made with infrared femtosecond pulses and a phase mask," *Optics Letters*, vol. 39, no. 12, pp. 3646–9, 2014.

[184] J. M. Jewell and I. D. Aggarwal, "Thermal lensing in heavy metal fluoride glasses," *Journal of Non-Crystalline Solids*, vol. 142, pp. 260–268, 1992.

[185] W. Shi, Q. Fang, X. Zhu, R. A. Norwood, and N. Peyghambarian, "Fiber lasers and their applications," *Appl. Opt.*, vol. 53, no. 28, pp. 6554–6568, Oct 2014.

[186] A. Carter, B. N. Samson, K. Tankala, D. P. Machewirth, V. Khitrov, U. H. Manyam, F. Gonthier, and F. Seguin, "Damage mechanisms in components for fiber lasers and amplifiers," in *SPIE Proc.*, no. 5647, 2005, p. 561.

[187] F. Maes, V. Fortin, M. Bernier, and R. Vallée, "5.6 W monolithic fiber laser at 3.55 µm," *Optics Letters*, vol. 42, no. 11, pp. 2054–2057, 2017.

[188] F. Maes, V. Fortin, S. Poulain, M. Poulain, J.-Y. Carrée, M. Bernier, and R. Vallée, "Room-temperature fiber laser at 3.92 μm," *Optica*, vol. 5, no. 7, pp. 761–764, 2018.

[189] J. Habel, T. Boilard, J. S. Frenière, F. Trépanier, and M. Bernier, "Femtosecond FBG written through the coating for sensing applications," *Sensors*, vol. 17, no. 11, p. 2519, 2017.

[190] Heraus, "Datasheet, Specialty fiber preforms for the most demanding applications," https://www.heraeus.com, 2018.

[191] X. Zhu and N. Peyghambarian, "High-power ZBLAN glass fiber lasers: Review and prospect," *Advances in OptoElectronics*, vol. 2010, 2010.

[192] H. Li, J. Lousteau, W. N. Macpherson, X. Jiang, H. T. Bookey, J. S. Barton, A. Jha, and A. K. Kar, "Thermal sensitivity of tellurite and germanate optical fibers," *Optics Express*, vol. 15, no. 14, pp. 8857–8863, 2007.

[193] Shasta Crystals, "Product Catalog," 2018.

[194] S. Jiang and J. Wang, "Method of fusion splicing silica fiber with low-temperature multi-component glass fiber," 2004, U.S. patent 6,705,771.

[195] K. Yin, B. Zhang, J. Yao, L. Yang, S. Chen, and J. Hou, "Highly stable, monolithic, single-mode mid-infrared supercontinuum source based on low-loss fusion spliced silica and fluoride fibers," *Optics Letters*, vol. 41, no. 5, pp. 946–949, 2016.

[196] R. Thapa, R. R. Gattass, V. Nguyen, G. Chin, D. Gibson, W. Kim, L. B. Shaw, and J. S. Sanghera, "Low-loss, robust fusion splicing of silica to chalcogenide fiber for integrated mid-infrared laser technology development," *Optics Letters*, vol. 40, no. 21, pp. 5074–5077, 2015.

[197] Z. Zheng, D. Ouyang, J. Zhao, M. , S. Ruan, P. Yan, and J. Wang, "Scaling all-fiber mid-infrared supercontinuum up to 10 W-level based on thermal-spliced silica fiber and ZBLAN fiber," *Photon. Res.*, vol. 4, no. 4, pp. 135–139, 2016.

[198] R. Thapa, D. Gibson, R. R. Gattass, C. Askins, W. Kim, S. Bayya, L. B. Shaw, and J. S. Sanghera, "Fusion splicing of highly dissimilar YAG crystal fiber and silica fiber with reaction bonding," *Optical Materials Express*, vol. 6, no. 8, pp. 2560–2566, 2016.

[199] J.-P. Bérubé, J. Lapointe, A. Dupont, M. Bernier, and R. Vallée, "Femtosecond laser inscription of depressed cladding single-mode mid-infrared waveguides in sapphire," *Optics Letters*, vol. 44, no. 1, pp. 37–40, 2019.

[200] A. J. Moulson and J. P. Roberts, "Water in silica glass," *Transaction of the Faraday Society*, vol. 57, pp. 1208–1216, 1960.

[201] M. Tomozawa, H. Li, and K. Davis, "Water diffusion , oxygen vacancy annihilation and structural relaxation in silica glasses," *Journal of Non-Crystalline Solids*, vol. 179, pp. 162–169, 1994.

[202] K. Davis, A. Agarwal, M. Tomozawa, and K. Hirao, "Quantitative infrared spectroscopic measurement of hydroxyl concentrations in silica glass," *Journal of Non-Crystalline Solids*, vol. 203, pp. 27–36, 1996.

[203] X. Jiang, J. Lousteau, S. Shen, and A. Jha, "Fluorogermanate glass with reduced content of OH-groups for infrared fiber optics," *Journal of Non-Crystalline Solids*, vol. 355, pp. 2015–2019, 2009.

[204] H. Knözinger and P. Ratnasamy, "Catalytic aluminas : surface models and characterization of surface sites," *Catalysis Reviews Science and Engineering*, vol. 17, no. 1, pp. 31–70, 1978.

[205] A. E. Kaloyeros, F. A. Jové, J. Goff, and B. Arkles, "Review—silicon nitride and silicon nitride-rich thin film technologies: trends in deposition techniques and related applications," *ECS Journal of Solid State Science and Technology*, vol. 6, no. 10, pp. 691–714, 2017.

[206] S. T. Bah, C. O. Ba, M. D'Auteuil, P. Ashrit, L. Sorelli, and R. Vallée, "Fabrication of TaO_xN_y thin films by reactive ion beam-assisted ac double magnetron sputtering for optical applications," *Thin Solid Films*, vol. 615, pp. 351–357, 2016.

[207] M. Józwik, P. Delobelle, C. Gorecki, A. Sabac, L. Nieradko, C. Meunier, F. Munnik, and M. Jo, "Optomechanical characterisation of compressively prestressed silicon oxynitride films deposited by plasma-enhanced chemical vapour deposition on silicon membranes," *Thin Solid Films*, vol. 468, pp. 84–92, 2004.

[208] C. A. Taylor and W. K. Chiu, "Characterization of CVD carbon films for hermetic optical fiber coatings," *Surface and Coatings Technology*, vol. 168, no. 1, pp. 1–11, 2003.

[209] K.-H. Haas and H. Wolter, "Synthesis , properties and applications of inorganic – organic copolymers," *Current Opinion in Solide State & Materials Science*, vol. 4, no. 1999, pp. 571–580, 1999.

[210] D. A. Pinnow, G. D. Robertson, and J. A. Wysocki, "Reductions in static fatigue of silica fibers by hermetic jacketing," *Applied Physics Letters*, vol. 34, no. 1, pp. 17–19, 1979.